A NON-LINEAR DYNAMIC MACROELEMENT FOR SOIL STRUCTURE INTERACTION ANALYSES OF PILES IN LIQUEFIABLE SITES

A Dissertation
Presented to
The Academic Faculty

by

Varun

In Partial Fulfillment
of the Requirements for the Degree
Doctor of Philosophy in the
School of Civil and Environmental Engineering

Georgia Institute of Technology
August, 2010

A NON-LINEAR DYNAMIC MACROELEMENT FOR SOIL STRUCTURE INTERACTION ANALYSES OF PILES IN LIQUEFIABLE SITES

Approved by:

Dr. Dominic Assimaki, Advisor
School of Civil and Environmental Engineering (Geosystems)
Georgia Institute of Technology

Dr. Reginald DesRoches
School of Civil and Environmental Engineering (SEMM)
Georgia Institute of Technology

Dr. Glenn Rix
School of Civil and Environmental Engineering (Geosystems)
Georgia Institute of Technology

Dr. Rami Haj-Ali
School of Civil and Environmental Engineering (SEMM)
Georgia Institute of Technology

Dr. Paul Mayne
School of Civil and Environmental Engineering (Geosystems)
Georgia Institute of Technology

Dr. Eduardo Kausel
Department of Civil and Environmental Engineering
Massachusetts Institute of Technology

Date Approved: June 22, 2010

To my Parents and Sister

ACKNOWLEDGEMENTS

I would like to thank my advisor Dr. Dominic Assimaki for her thoughtful guidance and advice during research. She has been a consistent motivating force for us to excel both as a role model and as a mentor. Be it the group meetings that taught us how to quickly read and extract the most out of research papers, or her assurance during problematic times with research that taught us importance of patience and persistence; being a part of her research group has been a continuous learning experience. I am also thankful to my committee members Dr. Rix, Dr. Mayne, Dr. DesRoches, Dr. Haj-Ali and Dr. Kausel for their valuable comments and suggestions regarding the research.

Several teachers including Dr. Rix, Dr. Mayne, Dr. Santamarina and Dr. Burns helped with the foundation of this research by means of courses that provided insight as well as useful tools for this research. While Dr. Rix's courses on earthquake engineering and soil dynamics really put a strong foundation for my research; the case histories from Dr. Mayne's foundation class notes came in most handy when it came to verifying that my FEM models were correct. I am also very thankful to Dr. Santamarina whose courses helped me see the role of geotechs in big picture including energy and sustainability while providing food for thought and an escape from soil dynamics.

I want to thank research group fellows Wei Li, Alexandros Kalos and Seokho Jeong for the interesting 'white board' discussions and suggestions regarding the research. Special thanks go to Abdollah for all his help with integrating the macroelement in Opensees. I also want to thank Aditya and Alex for the 'movie-time' and 'lunch-time' discussions.

Most importantly, I would like to thank my parents and sister for their unconditional love and continuous support, which allowed me to devote so much of my time and energy to this work.

Finally, I would like to acknowledge the project sponsors. The material presented in this research is based upon work supported by the NEESR program of the National Science Foundation under Grants No. CMS-0530478 and CMS-0402490, Project Title "NEESR-GC: Seismic Risk Mitigation for Port Systems". Any opinions, findings, and conclusions or recommendations expressed in this material are those of the author(s) and do not necessarily reflect the views of NSF.

TABLE OF CONTENTS

LIST OF TABLES

Page

LIST OF FIGURES

Page

LIST OF SYMBOLS

p , $\vec{p}$, p_i	Force per unit length (magnitude, vector, ith component)
u , $\vec{u}$, u_i	Displacement (magnitude, vector, ith component)
du , $\overrightarrow{du}$, du_i	Incremental displacement (magnitude, vector, ith component)
p_y	Ultimate resistance (per unit length)
f_ζ	Function controlling backbone curve
ζ , $\vec{\zeta}$, ζ_i	Hysteretic parameter (magnitude, vector, ith component)
$d\zeta$, $\overrightarrow{d\zeta}$, $d\zeta_i$	Incremental hysteretic parameter (magnitude, vector, ith component)
K_0	Initial stiffness (per unit length)
K	Stiffness (per unit length)
$\overline{\overline{K}}$	Stiffness matrix along principal directions (2D model)
$\overline{\overline{K}}_\theta$	Stiffness matrix along direction θ (2D model)
k_{ii}	Diagonal stiffness term (2D model)
k_{ij}	Cross-stiffness term (2D model)
θ	Angle made by any vector with x-axis
$\overline{\overline{\theta}}$	Transformation matrix for rotation of axes by angle θ
ψ	Angle between $\vec{\zeta}$ and $\overrightarrow{du}$
u_y	Yield displacement
α	Backbone curve stiffness parameter
b, g	Unloading/Reloading stiffness parameters
c	Cross-stiffness parameter for bidirectional (2D) loading model

p_s	Force per unit length exerted by spring
p_d	Force per unit length exerted by dashpot
c_r	Non-linear radiation damping coefficient
c_{re}	Linear radiation damping coefficient
a_0	Normalized loading frequency
r	Normalized soil resistance (per unit length)
r_d	Normalized soil resistance for drained case (per unit length)
S	Average effective stress ratio in near-field
S_{ff}	Effective stress ratio in free-field
S_0	Liquefaction front parameter
m_1	Slope of failure line
m_2	Slope of phase transformation line
w	Normalized shear work in macroelement
dw	Incremental shear work in macroelement
w_1	Liquefaction resistance parameter in macroelement
κ	Parameter controlling shape of strength degradation curve
η	Parameter to account for Poisson's ratio in liquefaction resistance
m_3, S_2	Parameters in pwp generation model
β	Drainage parameter in macroelement
B	Pile diameter
D	Depth below ground surface
f	Loading frequency
ω	Angular frequency

dt	Time increment
σ_v'	Effective vertical stress
σ_{v0}'	Initial effective vertical stress
ρ_s	Mass density of soil
V_s	Shear Wave velocity in soil
E_s	Young's Modulus of soil
G_s	Shear Modulus of soil
K_s	Bulk Modulus of soil
ν	Poisson's ratio of soil
φ	Internal friction angle of soil
φ_{ss}	Critical state friction angle of soil
δ	Dilation angle of soil
K_p	Coefficient of passive resistance in soil
n_p	Soil porosity
n	Power coefficient for soil stiffness
k	Hydraulic conductivity (permeability) of soil
$\gamma_{\max}$	Maximum shear strain in soil
χ	Liquefaction resistance parameter for soil
r_u	Excess pore water pressure ratio
V	Drainage velocity
L	Free surface drainage length
ε_v	Volumetric strain in soil

LIST OF ABBREVIATIONS

pwp	Pore water pressure
FEM	Finite Element Method
SSI	Soil Structure Interaction
ff	Far Field
2D	Two dimensional
3D	Three dimensional

SUMMARY

Implementation of performance-based design procedures for pile-supported waterfront structures involves estimation of the dynamic wharf response for hazard scenarios that include liquefaction of the backfill. In these cases, empirical techniques based on quasi-static observations and widely implemented in practice for the analysis of dynamic soil-pile interaction problems, may not be used to address the role of critical parameters such as soil permeability, rate of loading and residual soil strength in the wharf performance, nor simulate radiation damping phenomena for liquefiable soils in transient loading. On the other hand, very few experimental results exist on dynamic soil-pile interaction effects in liquefiable sites to justify the development of generic mechanical elements for this class of problems.

As part of this research, a macroelement is developed for soil-structure interaction analyses of piles in liquefiable soils, which captures efficiently the fundamental mechanisms of saturated granular soil behavior. The mechanical model comprises a nonlinear Winkler-type model that accounts for soil resistance acting along the circumference of the pile, and a coupled viscous damper that simulates changes in radiation damping with increasing material non-linearity. Three-dimensional (3D) finite element (FE) simulations are conducted for a pile in radially homogeneous soil to identify the critical parameters governing the response. The identified parameters, i.e., hydraulic conductivity, loading rate of dynamic loading, dilation angle and liquefaction potential are then expressed in dimensionless form. Next, the macroelement parameters

are calibrated as a function of the soil properties and the effective stress. A semi-empirical approach that accounts for the effects of soil-structure interaction on pore pressure generation in the vicinity of pile is used to detect the onset of liquefaction. The predictions are compared with field data obtained using blast induced liquefaction and centrifuge tests and found to be in good agreement.

Finally, the macroelement formulation is extended to account for coupling in both lateral directions. FEM simulations indicate that response assuming no coupling between the two horizontal directions for biaxial loading tends to overestimate the soil resistance and fails to capture features like ‘apparent negative stiffness’, ‘strain hardening’ and ‘rounded corners’.

CHAPTER 1

INTRODUCTION

Smooth and efficient transportation of goods is vital both for the development and competitive strength of trade and industry and for society in general. Among the alternative modes of transportation, naval route is perhaps the most economical one for international trade, a fact that renders ports as a critical link in the transportation chain. Indeed, forty percent of the value of U.S. international trade passes through ports, more than any other mode (Bureau of Transportation Statistics [1]). Furthermore, maritime trade value has nearly doubled in the last decade, from $434 billion in 1990 to $811 billion in 2003, and is likely to increase further given the expected growth in trade with Asia and Pacific-Rim nations and growing traffic congestion within land-based transport services. Clearly, these 'gateways for international trade' are 'critical civil infrastructural systems' indeed. Port components, however, are susceptible to significant damage from a variety of natural hazards, including earthquakes, tsunamis and hurricanes. In the life cycle of port structures, devastation by large earthquakes may be considered as a rare event, but with devastating magnitude of consequences nonetheless. As an example, the extensive damage caused by the Mw 6.9, 1995 Kobe earthquake to the port of Kobe required $8.6 billion and two years to repair, which caused the port to slip from the 6th to the 32nd largest in size in the world by 2003 along with long term loss in business. Extensive damage was caused at Derince and Akita ports during 7.4 M_w Kocaeli, Turkey earthquake of August 17, 1999. Recent examples of earthquake induced damage to ports include Port de Port-au-Prince during 7.0 M_w Haiti earthquake of January 10, 2010 and Port of Coronel, Port at Valparaiso and Port of San Antonio during 8.8 M_w Chile earthquake on February 27, 2010. As can be readily seen, earthquakes pose low probability-high loss risk to port structures, and in particular for the US, seismic hazard

maps by USGS (Figure 1.1) show that not only Western U.S. ports in Oakland, Los Angeles, Long Beach and Seattle but also Eastern U.S. ports in Charleston, SC and Savannah, GA are at high risk from earthquake damage.

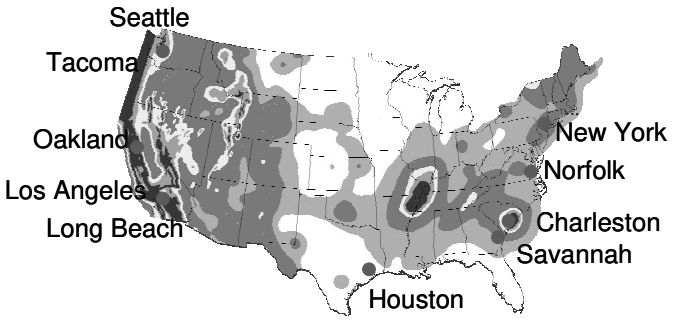

Figure 1.1 Location of large US ports and seismic hazard by USGS (PGA with 2% PE in 50 years)

Seismic Vulnerability of Wharf Structures

Wharfs are an important part of the port system as they provide a work surface for port operations and support material handling equipment, such as container cranes, and storage facilities which are critical in determining the material handling capacity and overall performance of the port. The most common type of wharf structure at large U.S. ports is a pile-supported marginal wharf (Figure 1.2).

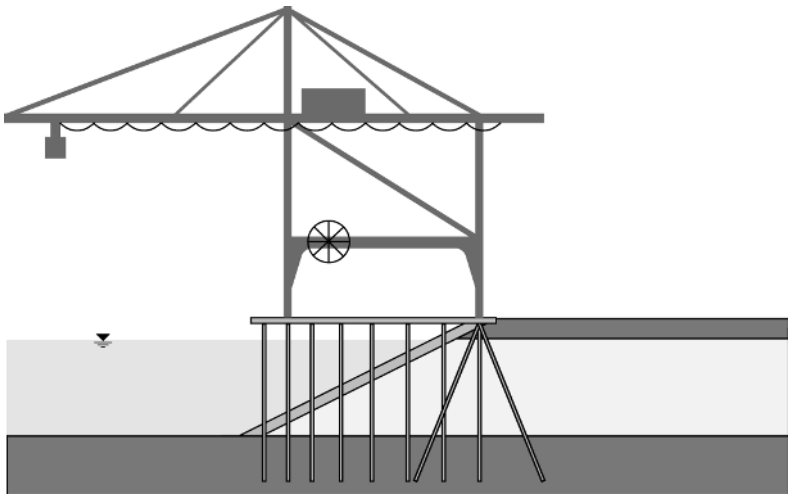

Figure 1.2 Soil-foundation-structure system for pile supported wharf (not to scale)

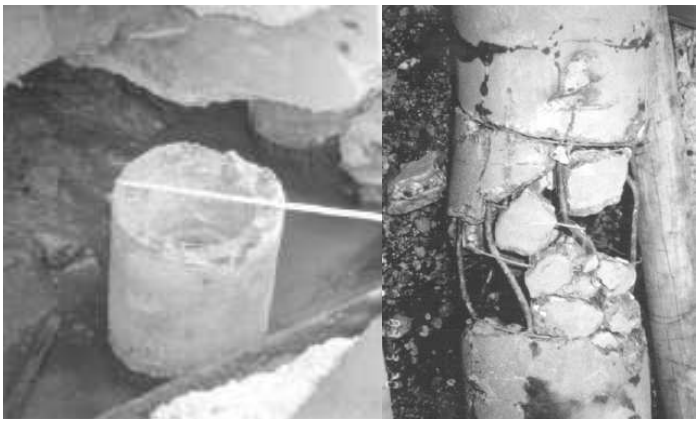

Figure 1.3 Shearing (left) and damage (right) to pile by ground displacement in Kobe 1995 and Niigata 1964 earthquakes, respectively (Finn & Fujita [2])

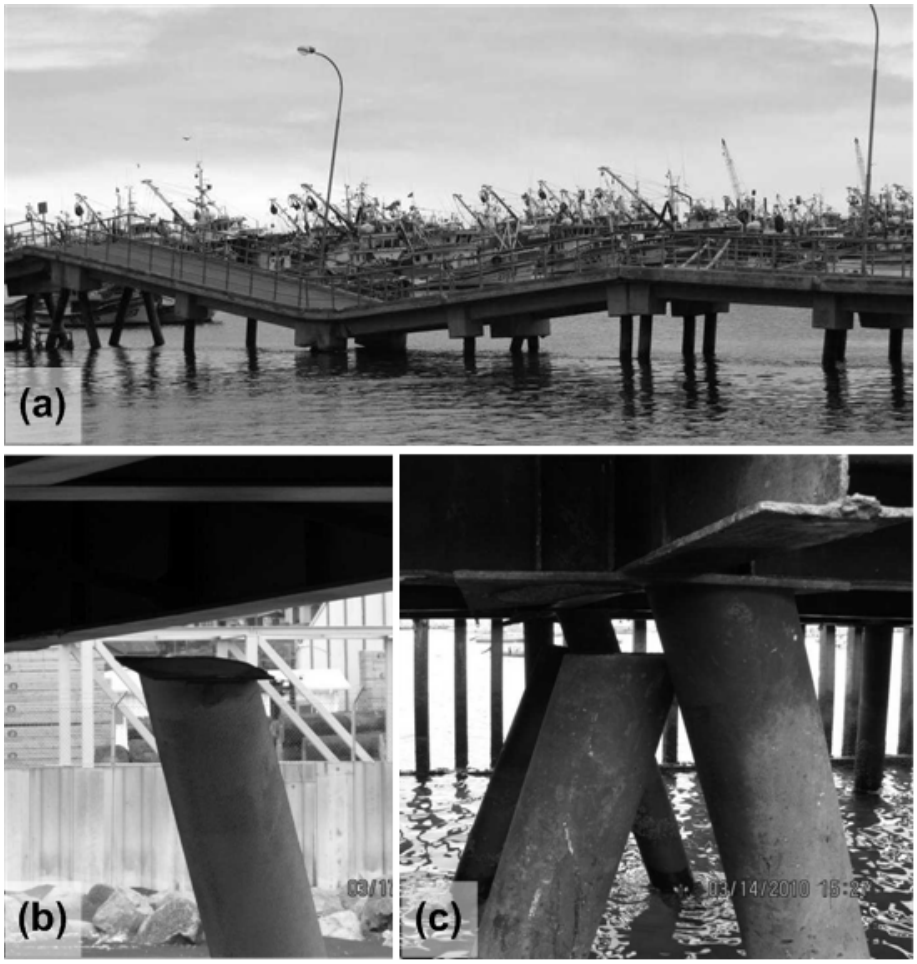

Figure 1.4 (a)-(b) Damage to fishermen's wharf and broken pile-wharf connections at Port of Coronel and (c) broken connections at Port of San Antonio from Feb, 2010 Chile earthquake. (Courtesy: GEER, www. geerassociation.org)

These structures consist of long, narrow pile-supported deck segments on sloping subsurface materials ranging from rock dikes to hydraulic fills. The wharfs are particularly vulnerable to damage during earthquakes caused by liquefaction of loose backfill soils. Liquefaction results in reduction in stiffness and strength of supporting soils and hence the loss of load carrying capacity of piles. Furthermore, the lateral spreading of liquefied soils exerts excessive forces often leading to shearing of piles and thus failure of the whole structure.

Figure 1.5 Satellite image of Port de Port-au-Prince before and after the 2010 Haiti earthquake showing the collapsed wharf, submerged cranes and sand boils (Google [3])

Examples include failures prevalent during 1964 Niigata and 1995 Kobe earthquake (Figure 1.3) and more recently during 2010 Haiti and 2010 Chile earthquake (Figure 1.4). Figure 1.5 shows the satellite image at Port de Port-au-Prince before and after the January 10, 2010 Haiti earthquake. The image after the earthquake is missing a large section of jetty and the main wharf next to the warehouse that collapsed due to liquefaction and subsided later due to lateral spreading. Two of the cranes sitting on the wharf earlier can also be seen submerged in water. Extensive signs of liquefaction in form of sand boils are also visible.

Reduction of Liquefaction Susceptibility

The liquefaction susceptibility of loose fills and liquefaction-related ground deformations may be reduced by a variety of soil improvement methods (e.g. PHRI [4]). Generally, these soil improvement methods rely on one or more of the following mechanisms to mitigate liquefaction hazards: (a) densification of loose soils, e.g., dynamic compaction (b) rapid dissipation of excess pore pressures via drainage so that the excess pore pressure ratio ($\Delta u/\sigma'v$) remains below about 0.6, (c) stiffening of the soil mass to limit the development of strains and thus excess pore pressures within the soil mass, e.g., deep soil mixing or (d) reinforcement of the soil mass via stiff inclusions that limit ground deformations even if liquefaction occurs. NRC [5] has pointed out the need to develop quantitative, performance-based guidelines that reflect these mechanisms to advance beyond current heuristic approaches. At existing waterfront structures of ports, traditional soil improvement methods can be used to treat soils in the backland, but these methods are difficult, impractical, and expensive to be employed for the treatment of soils beneath existing wharf components due to lack of access or sufficient clearance. In addition, traditional soil improvement methods are often poorly suited for developed sites such as port facilities because of adverse effects on adjacent structures due to vibration, densification, or increased lateral stresses as well as the disruption of ongoing port

operations. However, two innovative soil improvement techniques that overcome these problems and are thus well suited for remediating hydraulic fills prone to liquefaction at port facilities have been suggested. The alternative remediation techniques comprise: (a) installation of prefabricated vertical drains (Rathje et al [6]; Chang et al [7]) and (b) colloidal silica grout (Gallagher & Mitchell [8]; Gallagher et al. [9]; Pamuk et al. [10]). In the first method, perforated, corrugated plastic pipes (75 to 200 mm diameter) encased in a geotextile are installed at regular spacing (1-2m). Depending on their spacing, these pipes reduce the free drainage length significantly and hence are able to drain and rapidly dissipate excess pore water pressures thereby reducing the lateral spread by a considerable amount (Figure 1.6).

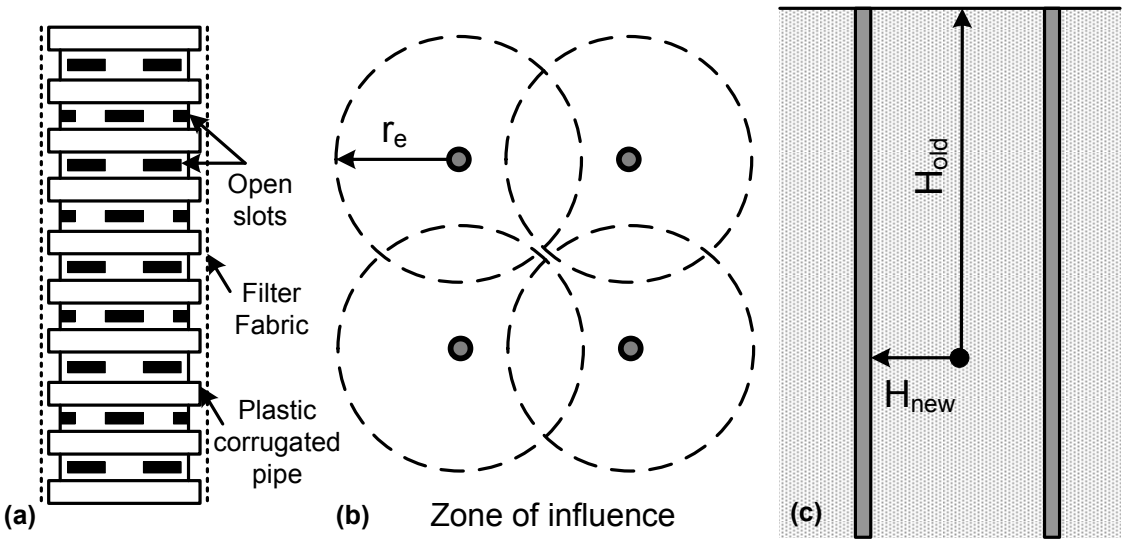

Figure 1.6 (a) Structure of prefabricated drain (b) its zone of influence and (c) reduced free drainage length for liquefied soil

Colloidal silica on the other hand is permeated into sand and it displaces water and fills up void space. The silica particles form a matrix that suppresses the dilation of sand and increases the liquefaction resistance as shown in Figure 1.7. Being a non-toxic and environmentally benign material with low viscosity and controllable gel times allows it to treat areas that are usually inaccessible to conventional methods (Figure 1.8).

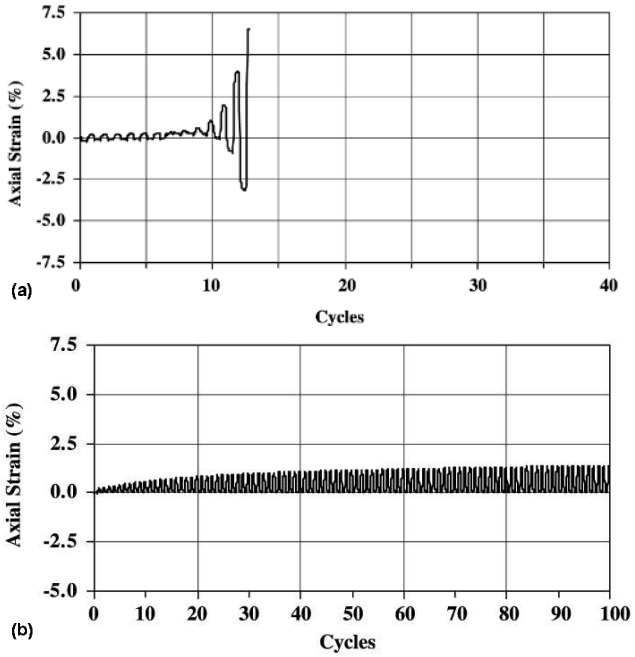

Figure 1.7 Increase in axial strain during cyclic loading (CSR 0.27) for Monterey sand (a) untreated and (b) treated with 10% colloidal silica (Gallagher and Mitchell [8])

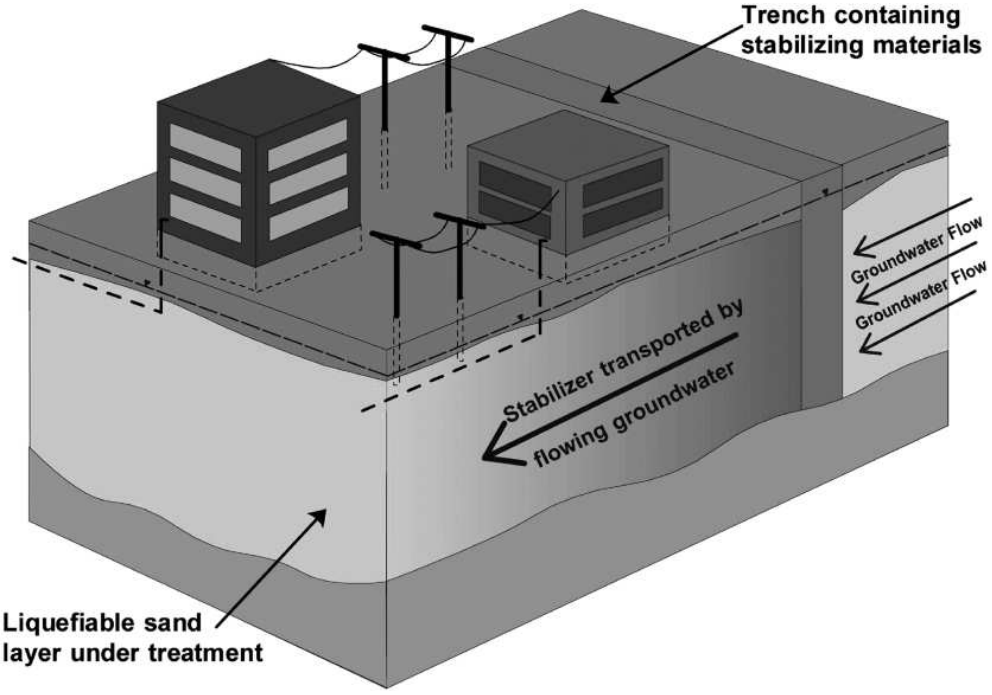

Figure 1.8 Passive site remediation for mitigation of liquefaction risk (Gallagher and Mitchell [8])

To evaluate the cost effectiveness of the new remediation techniques and determine an optimal remediation plan, one needs to estimate the reduction in risk achieved by different remediation options in a chosen configuration. Current engineering practice for seismic risk reduction for port facilities is typically based on design or retrofit criteria for individual physical components (e.g., wharf structures) expressed in terms of levels of force and/or displacement. However, the viability of a port following an earthquake depends not only on the performance of these individual components, but on their locations, redundancy, and physical and operational connectivity as well, i.e., on the port system as a whole. For example, if the operational capacity of a port system is controlled by the capacity of cranes, a higher reduction in risk may be possible by a combination of ground remediation and structural retrofitting than either of these two alone. Statistically sound risk assessment studies for such systems are based on a large number of alternative hazard analyses. Given the large number of components in the system, the total computational time required for assessment of response of all components under all possible hazard scenarios can be excessively large. Thus computational efficiency plays a big role in ultimate success of such comprehensive risk analyses programs.

As part of a multi-disciplinary project focusing on the seismic risk mitigation of port structures, scope of the proposed research is the development of simplified methods for the numerical simulation of pile-supported port waterfront structures subjected to earthquake loading. The target models will capture the important components of soil-structure interaction in an optimal computationally-efficient formulation to allow their implementation for multiple hazard realizations in an integrated risk analysis of port systems. The broad range of technical research issues addressed in this program, including liquefaction remediation, structural retrofitting options, and their integration in an efficient and effective prediction framework for soil-structure interaction are considered to be the most challenging and timely in the field of earthquake engineering

(NRC [5]). The development of the target soil-structure interaction models based on physical principles, validated via small and full scale experiments and coded into a broadly used finite element platform will contribute to the development of novel risk assessment methodologies for port structures, while being applicable for the seismic analysis of pile-supported structures beyond the scope of this project.

The thesis layout consists of nine chapters. Chapter 2 discusses the mechanisms of soil structure interaction along with its importance for pile supported wharves. A description of different methods available for soil-structure interaction along with their advantages and disadvantages is also presented. Chapter 3 presents the numerical framework used for simulations and parametric analyses along with detailed description of non-linear soil model. The parametric analyses are next presented in Chapter 4 along with the important observations. The critical governing parameters are identified and expressed in dimensionless form. Based on the observation in Chapter 4, a macro-mechanical model is proposed in Chapter 5. The different components are described first followed by the overall numerical scheme. The macroelement parameters are calibrated next as a function of soil properties in Chapter 6. Finally, the calibration is verified with 3D FEM simulations in Chapter 7 and benchmarked against field tests with blast induced liquefaction and centrifuge tests. Chapter 8 presents the extension of drained loading model to account for coupling in both horizontal directions. Due to lack of field or centrifuge biaxial lateral loading data, the model is verified by comparison with 3D FEM data. The conclusions and scope for future work is discussed in Chapter 9.

CHAPTER 2

SOIL STRUCTURE INTERACTION

Soil-structure interaction is the set of mechanisms that account for the flexibility of the foundation support beneath a given structure, and result in altering the motion in the vicinity of the foundation compared to the free-field. It determines the actual loading experienced by the structure-foundation-soil system resulting from the free-field seismic ground motions.

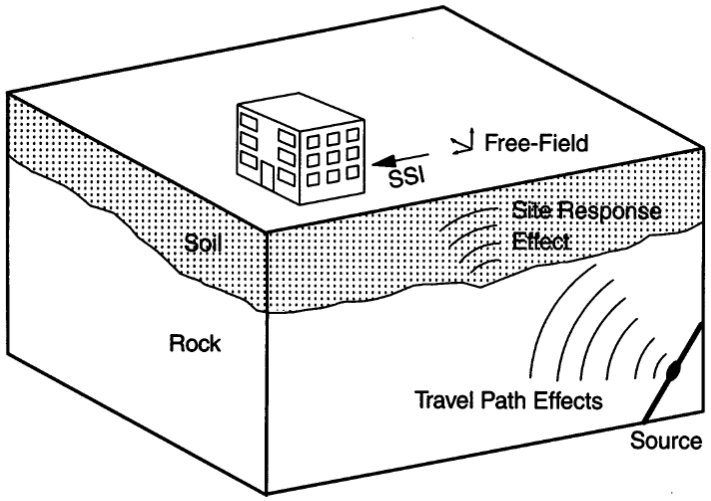

Figure 2.1 Context of SSI in engineering assessment of seismic loading of a structure (Stewart et al. [11])

Components of Soil Structure Interaction

During a dynamic loading like ground shaking during an earthquake, the deformations of a structure are affected by interactions between three linked systems: the structure, the foundation, and the geologic media (soil and rock) underlying and surrounding the foundation. A soil-structure interaction (SSI) analysis evaluates the collective response of these systems to a specified free-field ground motion. Two

physical phenomena comprise the mechanisms of interaction between the structure, foundation, and soil as shown in Figure 2.2:

a) Inertial interaction: This mechanism refers to the response of the complete structure-foundation-soil system to excitation by D' Alembert forces associated with the acceleration of the super-structure due to kinematic interaction.
b) Kinematic interaction: Even if the mass of super-structure is zero or there is no super-structure present, the presence of stiff foundation elements either on the formation or embedded in the underlying soil, result in the deviation of the foundation motion with respect to the corresponding motion of the so-called free-field, namely the response of the soil formation in absence of the structure. Three prominent mechanisms contributing to such deviations, according to Stewart et al. [11] are
    a. Base-slab averaging: Free-field motions associated with inclined and/or incoherent wave fields are "averaged" within the footprint area of the base-slab due to the kinematic constraint of essentially rigid-body motion of the slab.
    b. Embedment effects: Since the foundation is rigid and cannot deflect in exactly the same shape as far-field, the far field motion is filtered by the foundation depending on the wavelength of excitation. This is similar to 'Base Slab' averaging effect but is observed in case of coherent wave fields as well.
    c. Wave Scattering: Scattering of seismic waves off of corners and asperities of the foundation.

In the case of linear elastic or moderately nonlinear soil-foundation systems, inertial interaction analysis may be conveniently performed in two steps (Kausel & Rosset [12]) as shown in Figure 2.3. The foundation dynamic impedances (springs and dashpots) associated with each mode of vibration are computed first and then used to

evaluate the seismic response of structure and foundation supported by these springs and dashpots and subjected to the kinematic accelerations of the base.

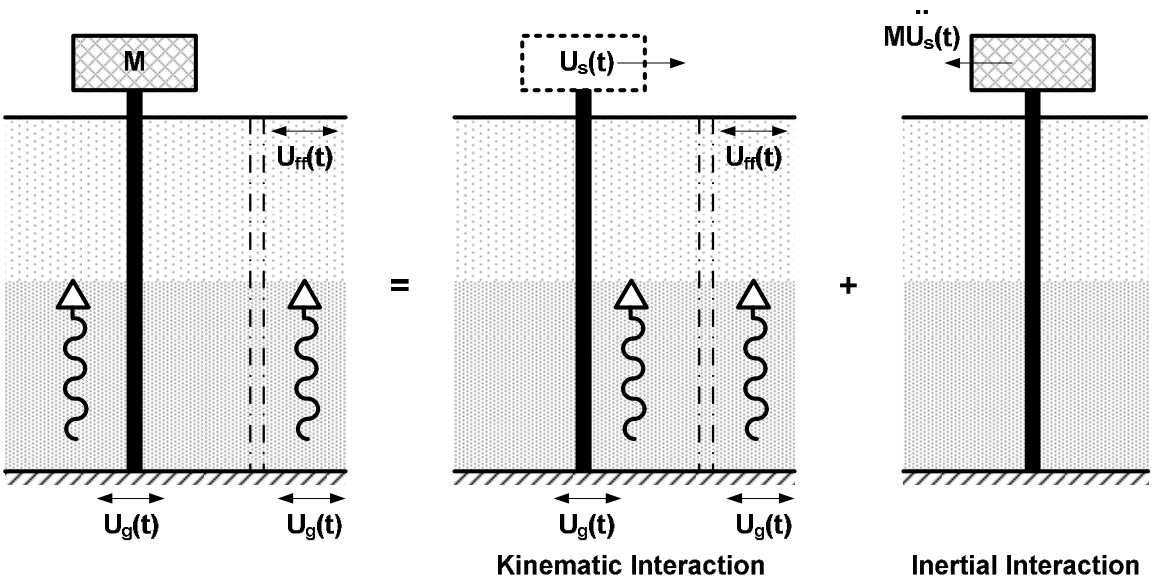

Figure 2.2 Components of Soil-structure Interaction

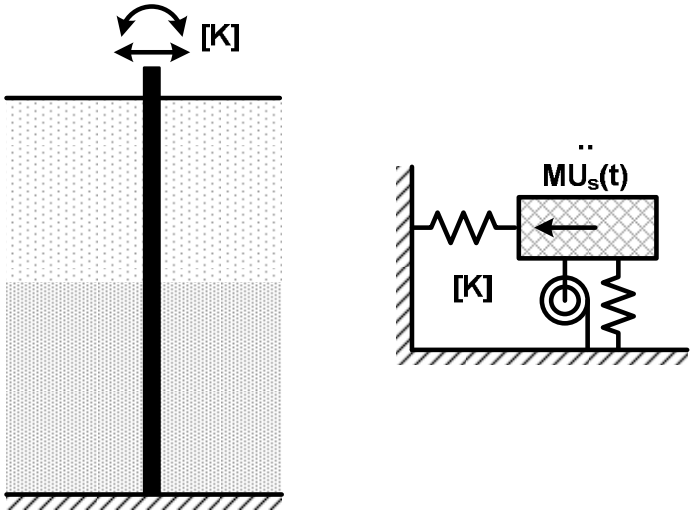

Figure 2.3 Schematic representation of two step inertial interaction analyses

The dynamic impedance is a complex function, where the real and imaginary parts represent the dynamic stiffness and energy attenuation of the system, respectively. The attenuation represented by the imaginary part of the impedance function is a

consequence of hysteretic damping in the soil and foundation, and radiation of seismic energy away from the foundation through the soil. Generally it is the radiation damping that mostly dominates the imaginary part and in most cases the analytical expressions are derived for elastic medium with no damping and then the damping is taken into account using the correspondence principle by multiplying the impedance function with (1+i2D'), where D' is the coefficient of material damping. However, hysteretic damping becomes more significant with increasing soil non-linearity.

As can be readily seen, accounting for the effects of soil-structure interaction may significantly alter the predicted response of the soil-foundation-structural system, a fact that renders these phenomena critical in engineering design. It should be also noted that for the fictional condition of an infinitely stiff soil, the amplitude of the transfer function for translational motion is unity and the phase is zero (i.e. the foundation and free-field motions are identical), and the impedance function has infinite real part and zero imaginary part. As a result, ignoring the effects of soil-structure interaction effects (which is common practice in structural design) inherently implies the unrealistic assumption of an infinitely rigid underlying soil medium.

Methodologies for Soil-Structure Interaction Analysis

The general methods to quantify soil structure interaction effects are:

a) Direct approach: In a direct approach, the soil and structure are simultaneously accounted for in the mathematical model and analyzed in a single step. Typically, the soil is discretized with solid finite elements and the structure with finite beam elements. Since assumptions of superposition are not required, true nonlinear analyses are possible in this case. Nonetheless, the analyses remain quite expensive from a computational standpoint. Hence, direct SSI analyses are more commonly performed for structures of very high importance and are not employed for the design of regular structures.

b) Substructure approach: In a substructure approach, the SSI problem is decomposed into three distinct parts discussed above which are combined to formulate the complete solution. The superposition principle is exact only for linear soil, foundation and structure behavior. Nevertheless, approximations of soil nonlinearity by means of iterative wave propagation analyses allow the superposition to be applied for moderately-nonlinear systems. The principal advantage of the substructure approach is its flexibility. Because each step is independent of the others, it is easy to focus resources on the most significant aspects of the problem.

For each one of the three analysis steps, several alternative formulations have been developed and published in the literature, including finite-element, boundary-element, semi-analytical and analytical solutions, a variety of simplified methods, and semi-empirical methods. In addition to the dynamic finite element methods, the most popular approaches used in practice for the analysis of soil-structure interaction problems are briefly presented in the ensuing:

a) Boundary element type methods: The methods of this class are essentially semi analytical in the sense that they use closed-form solutions to the pertinent wave equations for the soil domain, and discretize only the boundaries and interfaces of the system. These closed-form solutions (referred to as fundamental solutions or Green's functions depending on the particular solution) have the ability to reproduce exactly the radiation of wave energy to infinity, without requiring special lateral boundaries, as is the case for the finite element methods. Evidently, this class of methods is the most versatile in treating a variety of incident wave fields (such as inclined body waves and Rayleigh waves, in addition to vertical waves). Usually however, they cannot accommodate material and interface nonlinearities associated with foundation seismic motion. Therefore in current

state of practice, such sophisticated tools are also used in conjunction with finite element methods, which can better model the nonlinear soil-structure response.

b) Winkler models: Used primarily for the inertial interaction analysis, the foundation in these methods is supported by a series of independent vertical, rotational and horizontal springs and dashpots along the soil-foundation interface, which correspond to the different vibration modes.

Given the need for simplified computationally efficient models for risk analyses of port structures, we investigate state-of-the-art for existing formulations used for simulating soil-structure interaction for piles. Different methodologies to account for liquefaction effects and their merits and drawbacks are also presented.

Soil Structure Interaction for Pile Supported Wharfs

The seismic response of pile-supported wharves is inherently a complex problem dominated by soil-structure interaction involving large ground displacements and pore pressure generation potentially leading to liquefaction of the backfill. In addition, coupled transverse, longitudinal, and torsional response of the wharf is a critical component for the damage state predictions of pile-supported waterfront structures. The unequal embedment of piles in sloping ground coupled with the differential ground motion (due to wave propagation effects), induces significant torsional effects that cause rocking and uplift of crane structures adding further complexity in the chain of soil-structure interaction effects. Figure 2.4 shows various mechanisms of pile damage during backfill liquefaction as reported by Tokimatsu et al. [13]. For a comprehensive assessment of the soil-structure system performance during seismic loading, detailed 3D finite element coupled solid-fluid simulations should be ideally conducted, where the soil and structural components would be represented by means of appropriate non-linear constitutive models.

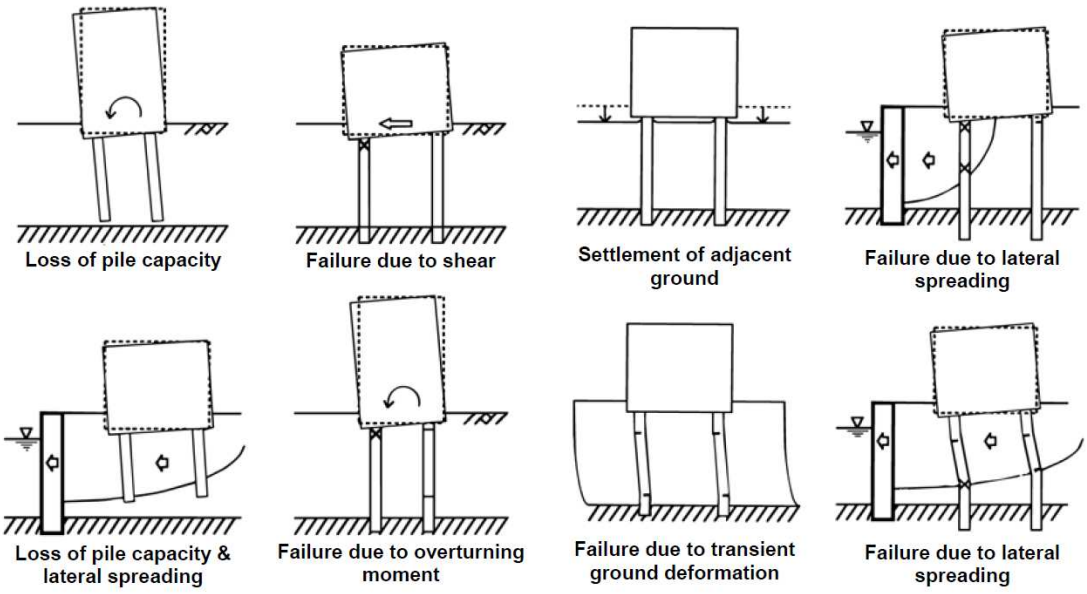

Figure 2.4 Pile damage mechanisms in liquefied soils (Tokimatsu et al. [13])

Inasmuch such analyses are feasible, however, they are associated with increased cost resulting from the input parameter acquisition for the constitutive models, and the engineering expertise necessary for the numerical modeling and the target result interpretation. Furthermore, the substantial computational effort involved in the realization of these analyses prohibits their use in statistically sound risk assessment studies mentioned above. Hence, simplified methodologies capable of capturing the important aspects of the problem at the optimal computational effort are required. The most common approach for simplified analyses is the use of Winkler spring models. According to this approach, the soil continuum is replaced by a series of independent springs in horizontal, rotational and vertical direction to represent soil resistance for each mode of vibration. The radiation damping due to waves emanating away from the foundation-soil interface is represented by means of corresponding dashpots along with the springs. The different approaches for analyzing soil structure interaction are shown in Figure 2.5. The state-of-the-art in all the methods is described below as well.

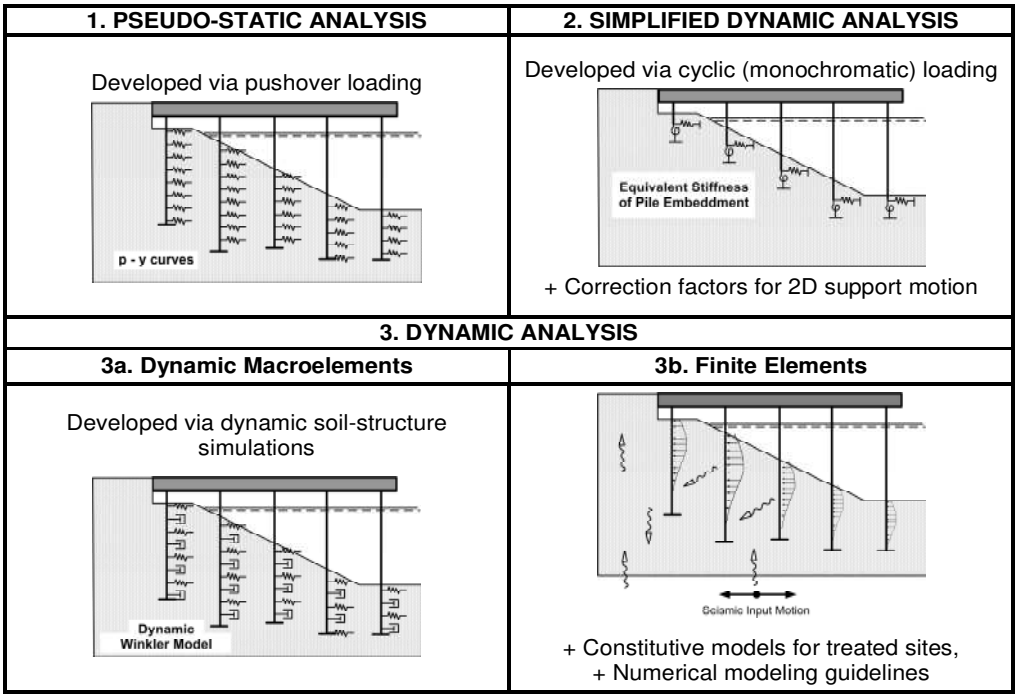

Figure 2.5 Different approaches for soil structure interaction of wharf structures

Pseudostatic analysis or p-y approach:

As the name suggests, a static analysis is carried out to obtain the maximum bending moment and shear force developed in the pile due to earthquake loading. The soil resistance is represented by means of non-linear Winkler springs or p-y curves and the inertial force acting on the pile head is given by product of cap-mass and spectral acceleration (Dowrick [14]). The most popular p-y curves for nonliquefiable soils include those developed by Matlock [15], Reese et al. [16] and API [17]. However, these approaches are based on static and cyclic lateral load tests, and are not necessarily applicable to seismic loading conditions as the tests didn't necessarily excite the mechanisms involved in seismic loading (e.g. loads from the soil profile, local and global pore pressure generation). Since peak bending moments and/or peak superstructure displacements may occur before or after liquefaction develops and the p-y curves for both conditions are completely different, the accuracy for such methods largely depends on the

accuracy in selection of the correct curves and the material parameters for that instant of time. Furthermore, it has been observed from centrifuge experiments that the inertial forces and soil resistance are not always in phase and hence the maximum moments are generally over predicted (Brandenberg et al. [18]). These methods are thus attractive for design engineers because they do an acceptable job for providing the maximum moment envelope for design purposes but since development of fragility curves is based on damage states of different components and a higher accuracy is required, these methods are not expected to perform satisfactorily. Furthermore, these analyses fail to distinguish between ground motions on the basis of frequency content and hence are not able to capture resonance controlled phenomenon in soil structure interaction.

Simplified Dynamic Analysis

These analyses account for both the stiffness of soil and radiation of energy away from the piles. The free field motion is first determined by means of 1D analysis and applied at the free-field end of Winkler springs. Both closed form and semi-empirical expressions for frequency dependent complex springs (both stiffness and damping) have been developed for pile foundations for elastic soil by Novak [19]; Dobry et al. [20]; Kaynia and Kausel [21] and Kavvadas and Gazetas [22]. However, since these are frequency dependent they are not suitable for time domain analyses. Approximate frequency independent models have been developed by Penzien [23]; Kagawa [24]; Kagawa and Kraft [25]; Norris [26]; Nogami and Konagai [27] and Tabesh & Poulos [28]. El Naggar and Novak [29]developed a model that takes into account the nonlinear soil behavior by splitting the domain in near field (frequency independent springs) and far-field (the spring values are determined by dominant frequency in input motion). But all such models lack the ability to predict pile behavior when the soil around the pile starts to liquefy. For the seismic analysis of piles in liquefying soil, Winkler type models have been developed by Kagawa [30]; Fuji et al. [31]; and Liyanapathirana & Poulos [32]

in which the strength and stiffness of the springs are degraded as a function of pore pressure which is calculated by a 1D analyses. However, these models still fail in medium dense sands when displacement hardening is observed and also fail to capture effects such as soil-pile gapping at the interface.

Dynamic analyses using Macroelements

Macroelements are derived by integrating the material behavior over the locally affected volume and concentrating the global stress-strain response at representative locations of the soil-structure interface based on the externally applied loading. Bounded by limit equilibrium conditions, macroelements can simulate the coupled effects of soil plasticity and interface nonlinearities, anticipated to be substantially different for dynamic loading than those predicted for pushover or cyclic loading in simplified design procedures. Successively, decomposition of the far-field and near-field domain allows efficient frequency-domain methods to be employed in the far field, since analysis of the superstructure supported by macroelements incorporates nonlinear soil-structure interaction effects. The concept of macroelements has been investigated in the past, for the simulation of nonlinear phenomena in soil -structure interaction problems. In particular, material nonlinearities, associated with the nonlinear constitutive behavior of the supporting soil and components of the superstructure and the foundation, have been investigated in the context of nonlinear FE analyses (Borja et al. [33]), as well as experimentally (Funston & Hall [34]; Stokoe & Richard [35]; Gazetas & Stokoe [36]; Kim et al. [37]), and attempts have been made to develop physical spring-dashpot elements or introduce modification functions in the classical formulation of the foundation impedance matrix, to model the mechanical interaction between rigid body and ground. Nonetheless, results are mainly derived from curve fitting of the numerical or experimental results, and therefore are highly dependent on the constitutive soil model and loading path used to calibrate the input parameters (Finn & Yogendrakumar [38]), or

the mechanical properties of rigid body and ground respectively. Geometric nonlinearities, associated with void formation between the foundation and the soil, have been extensively studied (Wolf [39]; Wolf & Skriherud [40]; Kobori et al. [41]). Recently, quasi-static foundation macroelements have been developed to describe the geometrical nonlinearities at the soilstructure interface, expressed in global variables at the foundation level, for shallow foundations on cohesionless (Nova & Montrasio [42]; Paolucci [43]) and cohesive soils (Crémer [44]). For pile foundations, macroelements have been developed for quasi-static case by Taciroglu et al. [45], Rha and Taciroglu [46] and for dynamic case by Boulanger et al. [47], Curras et al. [48] and Gerolymos & Gazetas [49],[50].

p-y curves for piles in liquefiable soils

For pseudo-static analyses using the BNWF approach, there are multiple approaches to model the behavior of liquefied sand. The first approach uses limit pressures to represent the laterally spreading liquefied sand and any overlying non-liquefied layers and p-y springs to model the layers below the lateral spreading zone. Recommendations for limit pressures include using 30% of the initial overburden effective stress by Japan Road Association (JRA [51]) based on analyses of case histories in 1995 Kobe earthquake; and a depth independent value of 10 kPa for the liquefied layer by Abdoun and Dobry [52] based on centrifuge tests.

Another approach is to treat liquefied sand as undrained soft clay and use the p-y curves for soft clay. The undrained shear strength to be used in this case is obtained as ratio of undrained shear strength to initial effective overburden stress using in-situ data and is a function of relative density and overburden stress.

The third and more widely employed approach that has been used in macroelements as well for the simulation of pile response in liquefiable soils is the use of load-displacement (referred to as p-y) curves developed by Matlock [15], Reese et al.

[16]and API [17] for non-liquefiable soils, scaled by factors referred to as p-y multipliers, which account for the effects of liquefaction by means of the pore pressure ratio expected to develop during the dynamic loading. Among others, multipliers have been suggested by the Japan Road Association (JRA [51]), the Architectural Institute of Japan (AIJ [53]), Liu & Dobry [54], Wilson et al. [55] and Brandenberg et al. [18] as shown in Figure 2.6.

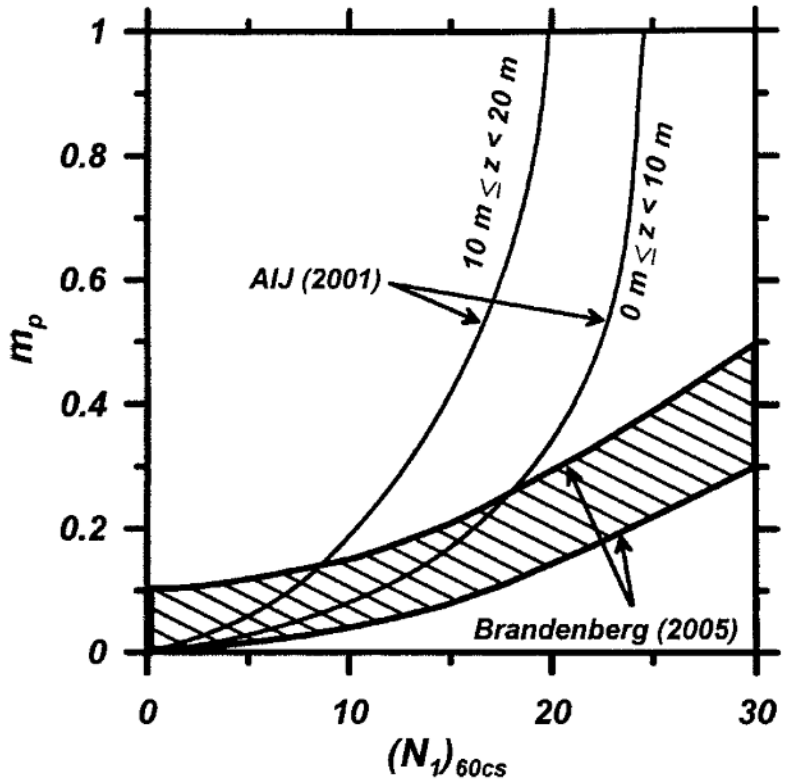

Figure 2.6 p-y multipliers recommended by AIJ [53] and Brandenberg [56]. (figure from Brandenberg et al. [18])

Dobry et al. [57] and Liu & Dobry [54] showed that the pile bending moments could be reasonably predicted if the original non liquefied p-y curves were multiplied by an apparent p-multiplier that decreased more or less linearly with excess pore pressure ratio and reached a minimum value of about 0.1 when the excess pore pressure ratio was unity. While these recommendations were based on dynamic tests, or at least tests involving liquefied soil, the resulting p-y curves were still based on adjusting curves derived from static and cyclic loading tests. Wilson et al. [58] showed that the

dependence of p-y resistance on pore pressure is also a function of relative density of sand and the curves may not even look similar for different relative density. While the p-y resistance of loose sand (e.g., Dr =35%) is much smaller and softer than for medium-dense sand (e.g., Dr =55%), the p-y behavior in medium-dense sand progressively softens with time during shaking as pore pressures, strains, and number of load cycles increase and shows displacement hardening whenever the previous displacement values are exceeded. This behavior may be attributed to the nearly undrained loading conditions and the tendency for the soil to dilate under these loading conditions (i.e., large enough strains to move the sand through a phase transformation). Similar observations of strain hardening p-y behavior have since been reported based on the blast induced liquefaction testing at Treasure Island (Ashford and Rollins [59]; Ashford et al. [60]; Rollins et al. [61],[62]; Weaver et al. [63]) and based on large shaking table tests (Tokimatsu et al. [64] and Tokimatsu and Suzuki [65]).

Pore pressure observations near the pile during blast induced liquefaction tests also showed pore pressure buildup and degradation of response during cyclic pile loading due to compactive tendency of soil during shearing imposed by pile motion. This was followed by transient drops in excess pore pressure during later cycles when the shear strains imposed by the pile became large enough to push the soil above the phase transformation line and exhibit dilative tendency. The importance of soil structure interaction effects in near field have also been reported by Abdoun et al. [52] and Gonzalez et al. [66] where the shearing of pile caused reduction of pore pressure in a inverted conical zone around the pile and significantly affected the soil resistance as seen from pile. Furthermore, the formation of zone was controlled by the soil permeability, with lower permeability soils not allowing the smaller near-field pore pressures to equalize with the higher far-field ones and thereby exhibiting a stiffer response than higher permeability soil which is somewhat contrary to the expected response.

Based on similar results observed in centrifuge experiments, Boulanger et al. [47] proposed a macroelement for soil-pile interaction, which combines scaled replicas of the original p-y curves for non-liquefiable soils with a dashpot to account for radiation damping, and a gap element to account for strain hardening. While this approach has been shown to predict pile response more realistically, however, the strain-hardening simulation capabilities of the macroelement are independent of soil properties. As a result, it is unable to distinguish the response of pile in soils that differ in terms of hydraulic conductivity, liquefaction resistance or dilation angle. Furthermore, while it does account for rate-dependence due to radiation damping, it doesn't account for seepage effects (Kutter & Voss [67]; Palmer [68]; Yoshimine [69]). Thus, extrapolation of its predictive capabilities to configurations that deviate from the experimental setup, in terms of soil properties or foundation characteristics, may not be guaranteed.

CHAPTER 3

DYNAMIC SOIL PILE INTERACTION SIMULATIONS

We investigate the soil parameters governing the response of soil-pile interaction problems in liquefiable soils by means of 3D finite element simulations, and propose a generic soil-pile interface macroelement formulation based on the parametric investigation results as a function of the critical soil properties. Numerical analyses were selected for the problem parameterization and subsequent calibration of the mechanical components due to the limited number of available physical tests. The latter, however, shall be used for validation of both the large scale FE simulations providing the "experimental" data, and of the performance of the macroelements for transient analyses of pile supported wharves in liquefiable soils.

Numerical Framework

Numerical simulations are performed using the finite element computer code DYNAFLOW (Prevost [70]). Parametric analyses are conducted for a single pile in homogeneous liquefiable soil, replicating the response of a slice of the full 3D numerical domain perpendicular to the cross section of the pile as shown in Figure 3. Both soil and pile are modeled as porous solids using four node quadrilateral elements. The pile is simulated as an elastic material with very low permeability to avoid coupling of structural non-linearity with the soil response. The soil is simulated by means of a pressure dependent multi-yield plasticity model with associative flow rule for the deviatoric (distortional) component and a non-associative flow rule for the volumetric component (Prevost [71]). Dynamic soil-fluid coupling in the soil material necessary for the simulation of liquefaction is achieved via extension of Biot's theory (Prevost [72]). The range of parameters for the constitutive soil model used in this study is presented in Table 3.1.

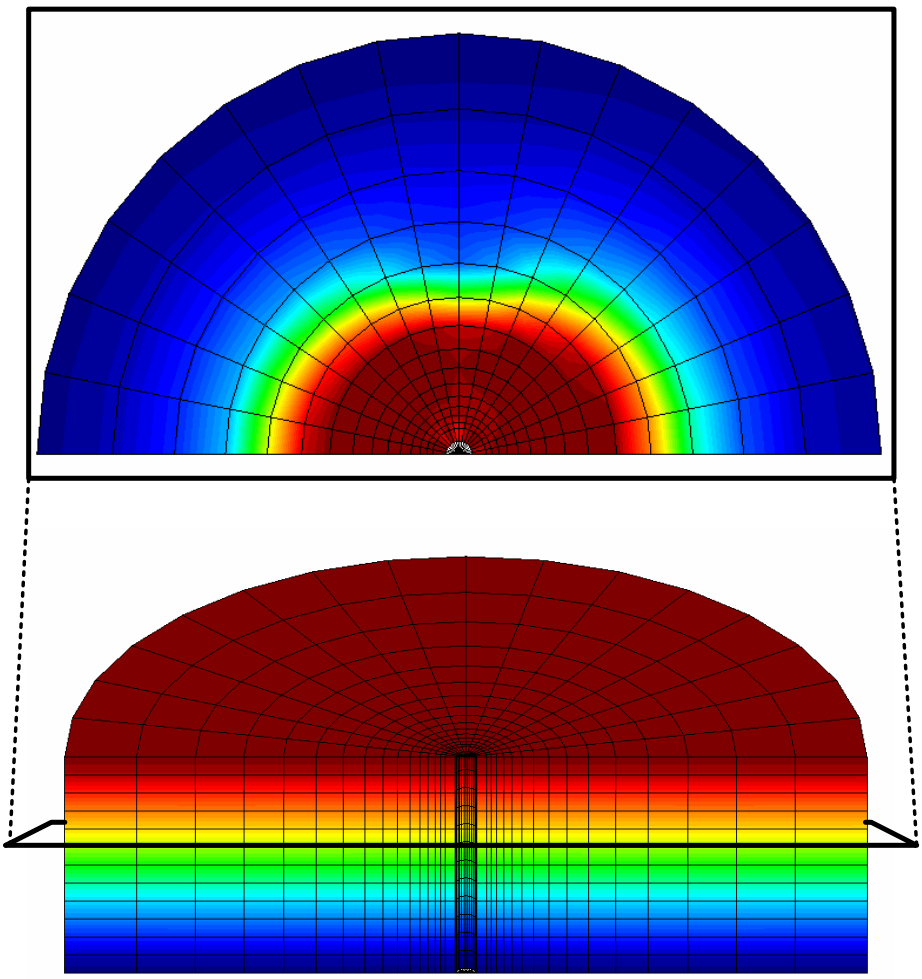

Figure 3.1 The 3D FEM model used for this study and the 3D slice (cross-section) at different depths which is equivalent of the macroelement in BNWF approach

In the simulated numerical domain, the far-field lateral boundary is defined 10 pile diameters away from the pile centerline. The element size in radial direction is smallest around the pile and increases geometrically away from the pile. The element size in vertical direction is constant throughout and is equal to one half of pile radius. The aspect ratio of element dimensions is kept less than 1:3 for all elements. At the boundary, both the solid and liquid phase are constrained from moving in radial direction. Both the pile and soil elements are provided a depth dependant initial effective stress equal to the geostatic equilibrium stress state to avoid differential settlement between the structure and soil which leads to shearing of soil around the pile in the consolidation phase itself.

In the first phase, the whole model is initialized by allowing it to consolidate. This is achieved by using Newmark's time integration with parameters $\alpha = 1.5$ and $\beta = 0.5$ and results in a stress and pore pressure distribution as shown in Figure 3.2.

In second phase, the pile is loaded in lateral direction by imposing prescribed displacements along the whole length of pile. For the second phase, the system of hyperbolic equations is solved using Newmark's time integration scheme with $\alpha = 0.65$, $\beta = 0.33$ which corresponds to some 'numerical damping'. This combination was chosen over 'no damping' $\alpha = 0.5$, $\beta = 0.25$ combination to damp out any high frequency numerical noise. Non-linear iterations were performed using Quasi-Newton technique with BFGS (Broyden, Fletcher, Goldfarb and Shanno) update formula where the updated Jacobian is approximated from previous one using "secant" equation rather than finite-difference approximation at each time step. Reaction forces at all the center nodes of pile were recorded to compute p-y curves. Representative displacement field during loading are shown in Figure 3.3 (vertical) and Figure 3.4 (total).

Table 3.1 Range of parameters used for soil model

Property	Symbol	Range
Elastic Parameters		
Shear Modulus	G_s	2 MPa
Bulk Modulus	K_s	4 MPa
Power Exponent	n	0.5-0.7
Yield Parameters		
Peak Friction Angle	φ	32-38°
Max. shear strain	γ_{max}	0.04-0.08
Dilation Parameters		
Critical state Friction angle	φ_{ss}	22-30°
Liquefaction Strength	χ	0.0-0.15
State Parameters		
Porosity	n^w	0.2-0.4
Hydraulic conductivity	k	10^{-3}-10^{-6} m/s
Solid phase density	ρ_s	2650 kg/m^3
Fluid phase density	ρ_w	1000 kg/m^3
Fluid Bulk Modulus	K_f	2 GPa

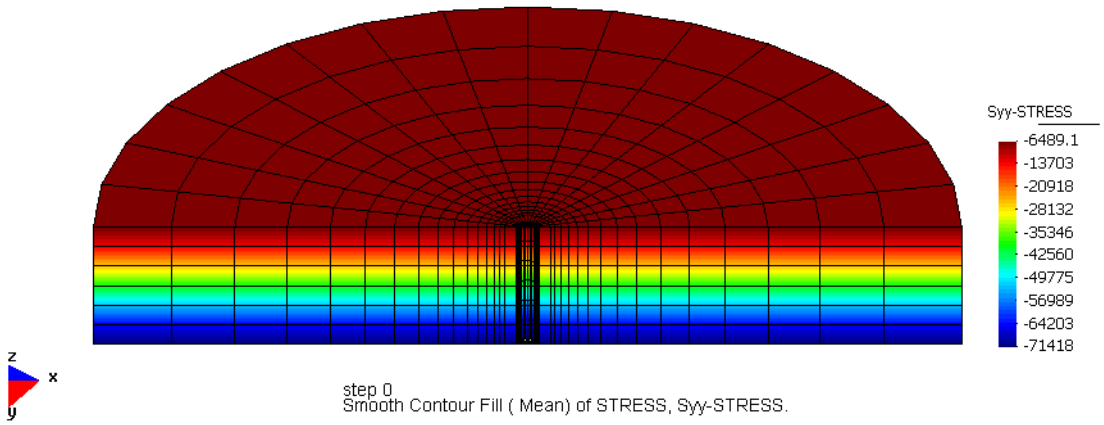

Figure 3.2 Effective vertical stress contours after consolidation phase

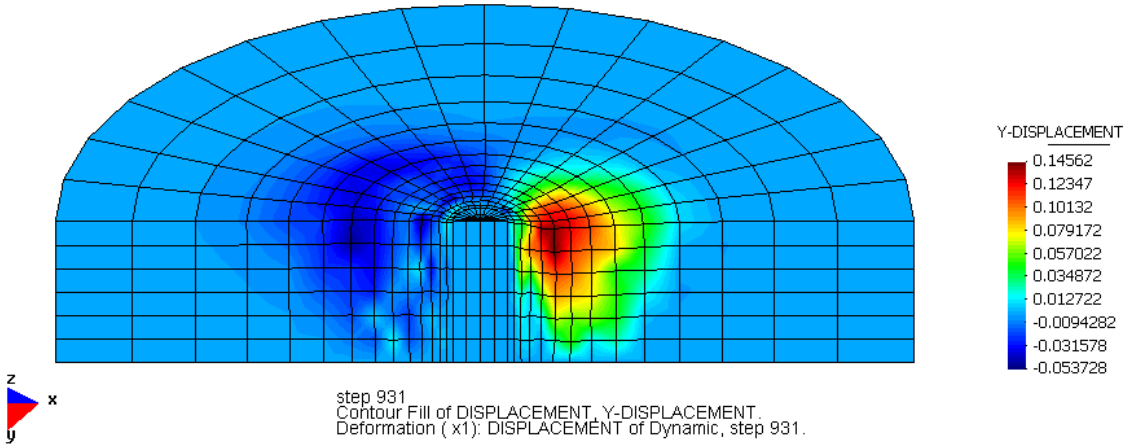

Figure 3.3 Vertical displacement contours showing vertical settlement of soil due to shearing during loading

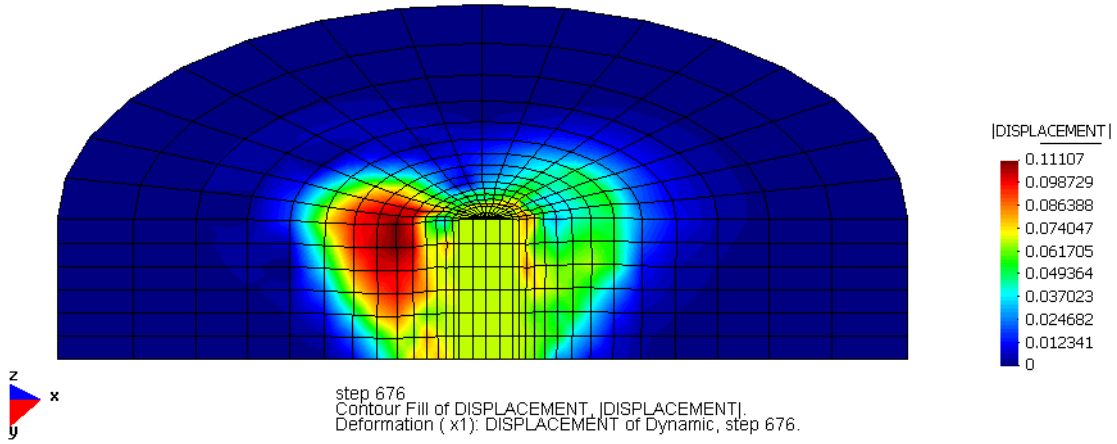

Figure 3.4 Total displacement contours showing formation of active and passive wedges

The Soil Model

The multi-yield constitutive soil model is a kinematic hardening model based on relatively simple plasticity theory (Prevost [71]) and is applicable to both cohesive and cohesionless soils. The concept of a "field of work-hardening moduli" (Iwan [73]; Mroz [74]; Prevost [75]) is used by defining a collection of nested yield surfaces in the stress space (figure). Von Mises type surfaces are employed for cohesive materials, and Drucker-Prager / Mohr-Coulomb type surfaces are employed for frictionless materials (sands).

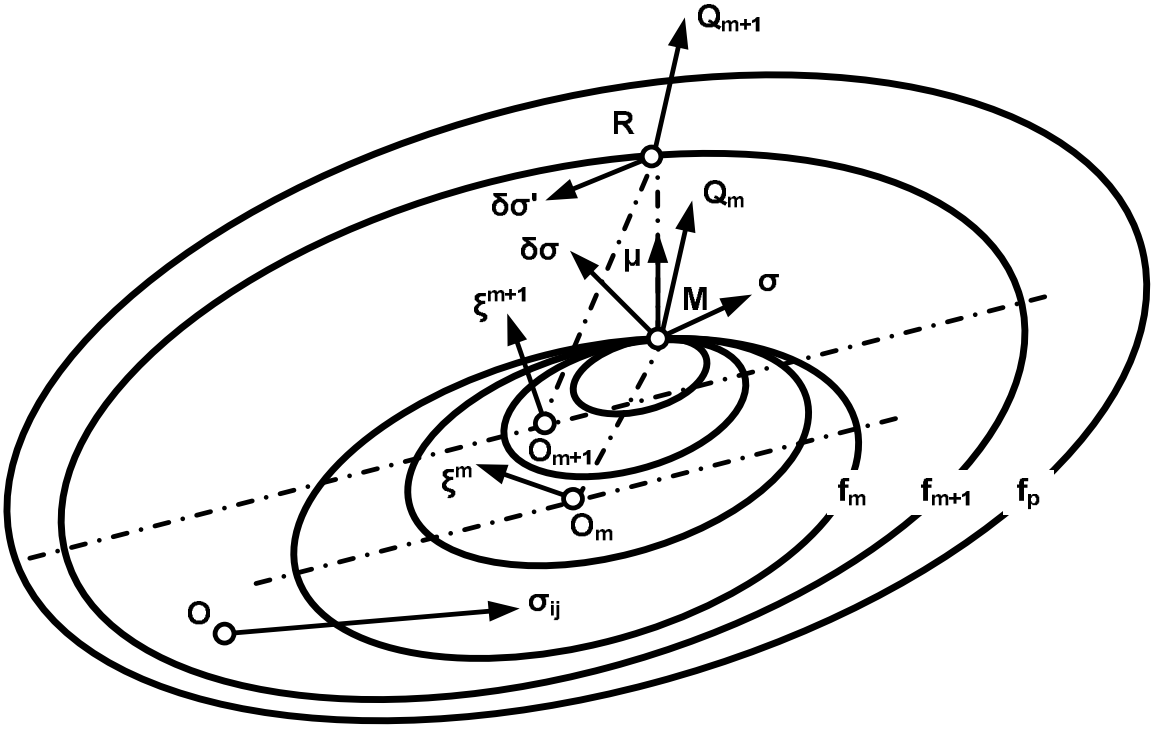

Figure 3.5 Field of yield surfaces in stress space - hardening rule

The yield surfaces define regions of constant shear moduli in the stress space, by means of which, the model discretizes the smooth elastic-plastic stress-strain curve into n linear segments. When the stress point reaches the yield surface f_m, all the yield surfaces $f_1, f_2 \ldots f_m$ are tangent to each other at the contact point M, as shown above. If a stress-rate σ_{ij} is then applied to the material element such that the stress-vector σ points out of the

yield surface f_m (.i.e. such that $Q^m.\sigma \geq 0$, where Q denotes a vector normal to the yield surface), the plastic-strain vector components are evaluated for the plastic Modulus H_m 'associated with the outermost yield surface. The plastic potential g_m associated with f_m is selected such that, in agreement with experimental observations, the plastic deviatoric strain vector remains normal to the projection of the yield surface onto the deviatoric stress subspace (Figure 3.5). The outermost surface f_p corresponds to zero shear strength.

For yield function for each yield surface is defined differently based on the type of material being simulated (pressure dependant or independent). For the pressure dependant model used in this study, the yield surface is given as

$$f = \left\{ \frac{3}{2} tr\left(s - \bar{p}a\right)^2 \right\}^{1/2} + k\bar{p}g\left(\theta\right) = 0 \tag{3.1}$$

where $\bar{p} = p - a$, $a = c/\tan\varphi$ is the attraction and $g(\theta)$ determines the shape of the cross-section on the deviatoric plane and is defined as follows:

$$g\left(\theta\right) = \frac{2M_k}{\left(1+M_k\right) - (1-M_k)\sin 3\theta} \tag{3.2}$$

where $\sin 3\theta = -\sqrt{6}\bar{J}_3 / \bar{J}_2^{3/2}$, $\bar{J}_2 = tr\bar{s}^{-2}$, $\bar{J}_3 = tr\bar{s}^3, \bar{s} = s - \bar{p}$ and M_k is a material parameter defined as $M_k = 1.0$ for Drucker-Prager cone and $M_k = (3-\sin\varphi)/(3+\sin\varphi)$ for round-cornered Mohr-Coulomb cone.

The plastic flow rule is defined as $\dot{\varepsilon}^p = \left\langle \dot{\lambda} \right\rangle P$, where $\dot{\varepsilon}^p$ is the strain-rate, P is the plastic potential ($P = P' + \delta P'''$), and $\dot{\lambda}$ is the plastic load factor and associative in the deviatoric component. To account for experimental evidence from tests on frictional materials, a non-associative flow rule is used for the dilational component:

$$3P''' = \frac{\left(\eta/\bar{\eta}\right)^2 - 1}{\left(\eta/\bar{\eta}\right)^2 + 1} \chi_{pp} \tag{3.3}$$

where $\bar{\eta}$, χ_{pp} are material parameters. This equation expresses the dependence of soil dilational behavior on the mobilized stress ratio $\eta = (3/2s:s)^{1/2} / p'$.

The material hysteretic behavior and shear stress-induced anisotropic effects are simulated by a kinematic rule. Upon contact, the yield surfaces are translated in the stress space by a stress point, and the direction of translation is selected such that the yield surfaces do not overlap, but remain tangent to each other at the stress point. For the case of pressure-sensitive materials, a purely kinematic rule is adopted. The dependence of the moduli on effective mean normal stress is assumed to be of the following form

$$x = x_0 (p / p_1)^n \tag{3.4}$$

where x represents the shear (G), bulk (K) or plastic (H) moduli, and n is the power exponent which can be estimated as $n \approx 0.5$ for cohesionless soils and $n \approx 1$ for cohesive soils.

The constitutive equations, $\dot{\sigma}' = E:(\varepsilon - \dot{\varepsilon}_p)$, where $\dot{\varepsilon}$ is the rate of deformation tensor and E is the fourth order isotropic elastic tensor, are integrated numerically using a stress relaxation procedure.

Constitutive model parameters

The required constitutive parameters of the multi-yield plasticity model are summarized in Table 1 along with the range and are described below.

State parameters

(a) Mass density of the solid phase ρ_s

For the case of porous media,

(b) Porosity n^w

(c) Permeability k

(d) Fluid mass density ρ_f

(e) Fluid Bulk Modulus K_f

Low strain elastic parameters

(a) Low strain reference Shear Modulus G_0

(b) Low strain reference Bulk modulus B_0

(c) Power exponent n

(d) Reference effective mean normal stress p_0'

The modulii are related through the Poisson's ratio as $B_0 = 2G_0(1+\nu)/3(1-2\nu)$.

For pressure dependant materials, the moduli dependence on mean effective normal stress p' is assumed to be of the form $G = G_0\left(p'/p_0'\right)^n$ and $B = B_0\left(p'/p_0'\right)^n$.

Yield and failure parameters

(a) Friction angle φ

(b) Maximum deviator strain $\gamma_{\max}$

(c) Slope of stress path in p-q' space S

(d) Coefficient of lateral stress K_0

These parameters describe the position a_i, size M_i and plastic modulus H_i', corresponding to each yield surface f_i. For a given number of yield surfaces, these parameters can be evaluated based on experimental stress-strain curves obtained from triaxial or simple shear soil tests (Prevost [71]). Alternatively, generation of stress-strain curves may be based on field information (Prevost [76]). For pressure dependant materials, a modified hyperbolic expression proposed by Prevost [76] and Griffiths and Prevost [77] is used to simulate soil stress-strain relations. The necessary parameters are: (i) the initial gradient and (ii) the stress and strain levels at failure. The initial gradient is given by the small stain shear modulus G_0. The maximum strain level $\gamma_{\max}$ is estimated from laboratory soil test results and the stress level at failure is expressed as a function of the friction angle at failure (φ) and the stress path slope (S). Finally, the coefficient of

lateral stress K_0 is required to evaluate the initial positions a_i of the yield surfaces. The material parameters necessary to describe shear stress-strain behavior are discussed in more detail in later section.

Dilation parameters

(a) Phase transformation angle φ_{ss}

(b) Dilation parameter χ_{pp}

These are used to evaluate the volumetric part of the plastic potential $3P'''$. The phase transformation angle φ_{ss} is related to the parameter $\bar{\eta}$ as $\bar{\eta}_{C/E} = \pm \frac{6\sin\varphi_{ss}}{3 \mp \sin\varphi_{ss}}$ where C stands for triaxial compression and E for triaxial extension. For general three-dimensional stress state, $\bar{\eta} = \bar{\eta}_C$ if $trs^3 < 0$ and $\bar{\eta} = \bar{\eta}_E$ if $trs^3 > 0$

Dilation parameter (also called liquefaction resistance parameter) χ_{pp}, which is a scaling parameter for plastic dilation and depends on relative density and sand type (fabric, grain size).

With the exception of dilation parameter, all the required constitutive model parameters are traditional soil properties, and can be derived from results of conventional laboratory (e.g., triaxial, simple shear) and in-situ (e.g., cone penetration, wave velocity, etc) soil tests. The dilation parameter is evaluated based on results of liquefaction strength analyses. For further details, the reader is referred to Popescu [78].

Solid-Fluid Coupling

Dynamic soil-fluid coupling in the soil material necessary for the simulation of liquefaction is achieved via extension of Biot's theory by means of modern mixture theories (Prevost [72]). The soil skeleton is modeled as a piecewise-linear time-independent porous medium. The field equations for non-linear case are given as follows: For the solid phase:

$$\rho_{se}\alpha_s = \nabla.\sigma_s\,' - (1-\varphi)\nabla p_w - \xi.(v_s - v_w) + \rho_{se}b \tag{3.5}$$

For the fluid phase:

$$\rho_{we}\frac{dv_w}{dt} = \rho_{we}(v_s - v_w).\nabla v_w - \varphi\nabla p_w + \xi.(v_s - v_w) + \rho_{we}b \tag{3.6}$$

where $\rho_{se} = (1-\varphi)\rho_s$ is the effective solid density, $\rho_{we} = \varphi\rho_w$ is the effective fluid density and $\xi = \frac{\varphi^2\rho_w g}{k}$ is the drag coefficient. For compressible fluids, the pressure is calculated as

$$\frac{Dp_w}{Dt} = -\frac{\lambda_w}{\varphi}\left[\nabla.(1-\varphi)v_s + \nabla.\varphi v_w\right] \tag{3.7}$$

In the field equations $\rho_{se}\alpha_s$ and $\rho_{we}\alpha_w$ represent the intertial forces whereas $\rho_{se}b$ and $\rho_{we}b$ are the body forces for solid and fluid, respectively. $\nabla.\sigma_s = \frac{\partial(\sigma_s)_{ij}}{\partial x_j}$ represents the stress gradient for the skeleton. $(1-\varphi)\nabla p_w$ and $\varphi\nabla p_w$ represent the effective fluid pressure gradient for solid and fluid case, respectively. $\xi.(v_s - v_w)$ represents the viscous drag force due to relative movement between solid and fluid whereas $\rho_{we}(v_s - v_w).\nabla v_w$ is the convective force that appears due to material derivative.

CHAPTER 4

PARAMETRIC INVESTIGATION

Parametric analyses were conducted for the following soil properties and loading characteristics: (a) dilation angle, δ (b) soil permeability, k; (c) initial overburden effective stress, σ_i' or depth, D; (d) liquefaction resistance, χ; (e) loading frequency, f and (f) displacement amplitude, u. The sensitivity of the macroscopic system behavior to the selected parameters was investigated by fixing all but one parameter, and monitoring the load-displacement response at the pile centerline. Unless specified otherwise, the results are presented for shear modulus (G = 20 MPa), Bulk Modulus (K = 40 MPa), power exponent (n = 0.5), solid phase density (ρ_s=2650 kg/m^3), friction angle (φ=32), phase transition angle (φ_{ss}=30), porosity (n^w=0.4), max devaitoric strain (γ_{max}=0.08) and liquefaction resistance parameter (χ=0.15) which correspond to the properties of loose (D_r=40%) Nevada sand (Popescu and Prevost [79]). The soil permeability is set to 10^{-9} m/s to simulate completely undrained loading. The pile diameter is 1 m and forced cyclic vibrations are applied with displacement amplitude of 20 mm at a frequency of 0.1 Hz to avoid any significant contribution to response from radiation damping. The range of parameters implemented in the ensuing is also specified in Table 1.

Effect of soil dilation angle (δ)

The dilation angle (δ) is the soil parameter that indicates the potential of the material to develop positive (compression) or negative (dilation) volumetric changes when subjected to shearing, and is defined as the difference between the peak friction and critical state friction angles, $\delta = \varphi - \varphi_{ss}$.

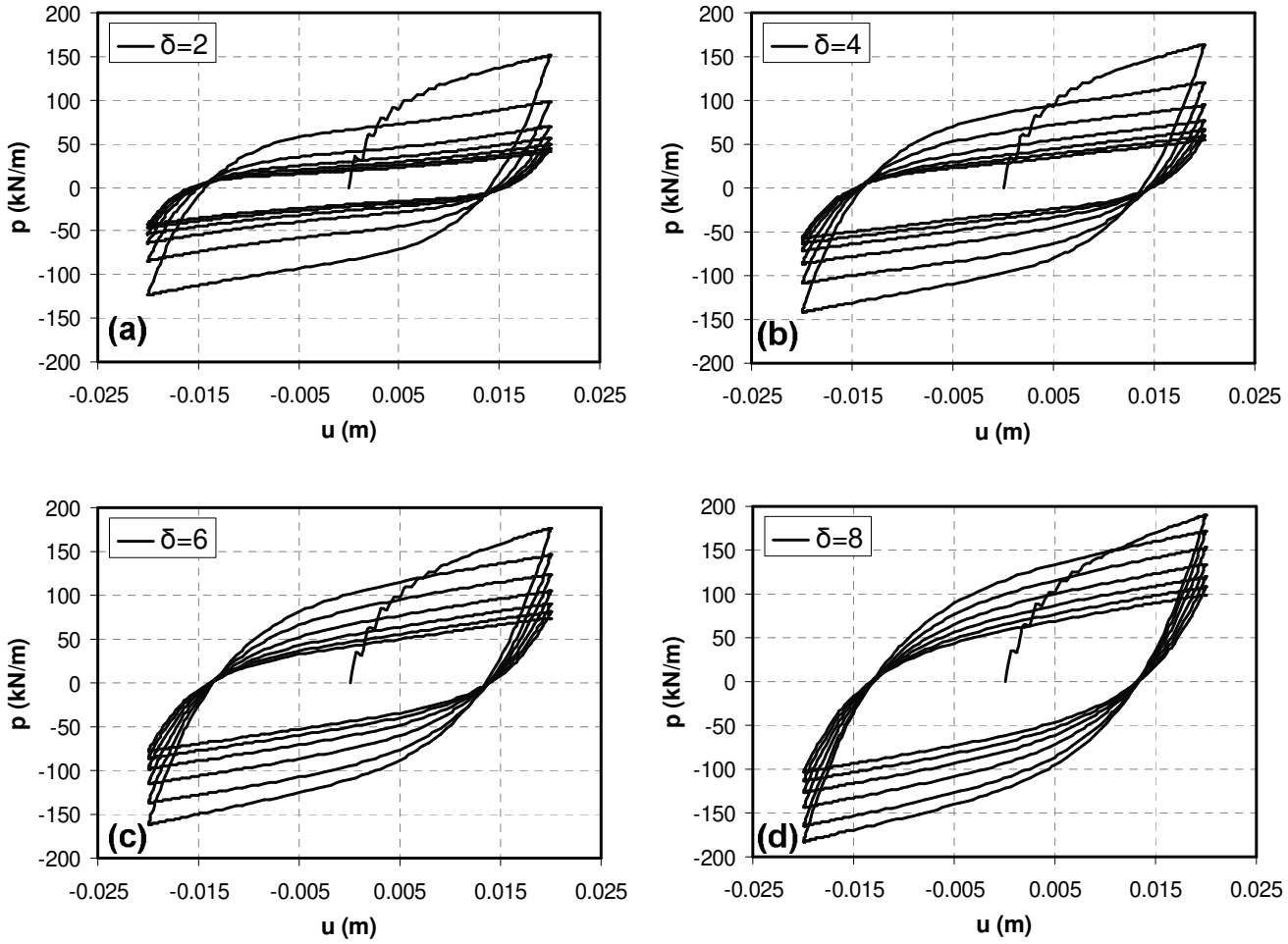

Figure 4.1 (a)-(d) Variation of pile response with dilation angle (at depth 2m)

To investigate the sensitivity of the response to variations of the dilation angle, the critical state friction angle -a function of soil type, grain size, shape (Been & Jefferies [80]) - is fixed at 30° that is typical for uniformly graded sub-rounded quartz soil, while the peak friction angle is allowed to vary between 32-38°.

The soil resistance vs displacement (p-y) curves at depth 2m are shown in Figure 4.1(a)-(d). The pile response obtained at other depths is also similar. Initially, the p-y curves show strain-softening behavior with stiffness decreasing as displacement increases. Since, the soil has a tendency to contract for stress ratios τ/σ' below the phase transition line, the initial cycles of cyclic loading lead to accumulation of excess pore pressure and the response degrades with increasing number of cycles. However, after the effective stress in the vicinity of the pile reaches a lower-bound threshold, phase transformation is observed in the soil and strain-hardening response results from the dilating tendency of soil. For soil with low dilation angle (2-4 degrees), the degradation in response with number of cycles is quite severe compared to higher dilation angle (6-8 degrees) that still retains more than 50% of their strength even after seven loading cycles.

Effect of soil permeability (k)

Figure 4.2 (a)-(d) shows the pile response in soils with hydraulic conductivity varying from 10^{-3} m/s to 10^{-5} m/s, which is representative of fine sands. The response shows a gradual variation from completely drained behavior for k=10^{-3} m/s to completely undrained behavior for k=10^{-5} m/s. For k=10^{-3} m/s, the rate of drainage of excess pore pressure is faster than rate of generation and hence the response shows almost no degradation; as hydraulic conductivity decreases, pore pressure generation starts dominating with the response for k=10^{-5} m/s being almost the same as the completely undrained response shown before. As can be seen from Figure 4.2, after a certain number of cycles, the pile response reaches a temporary steady-state condition, which is a function of the soil permeability.

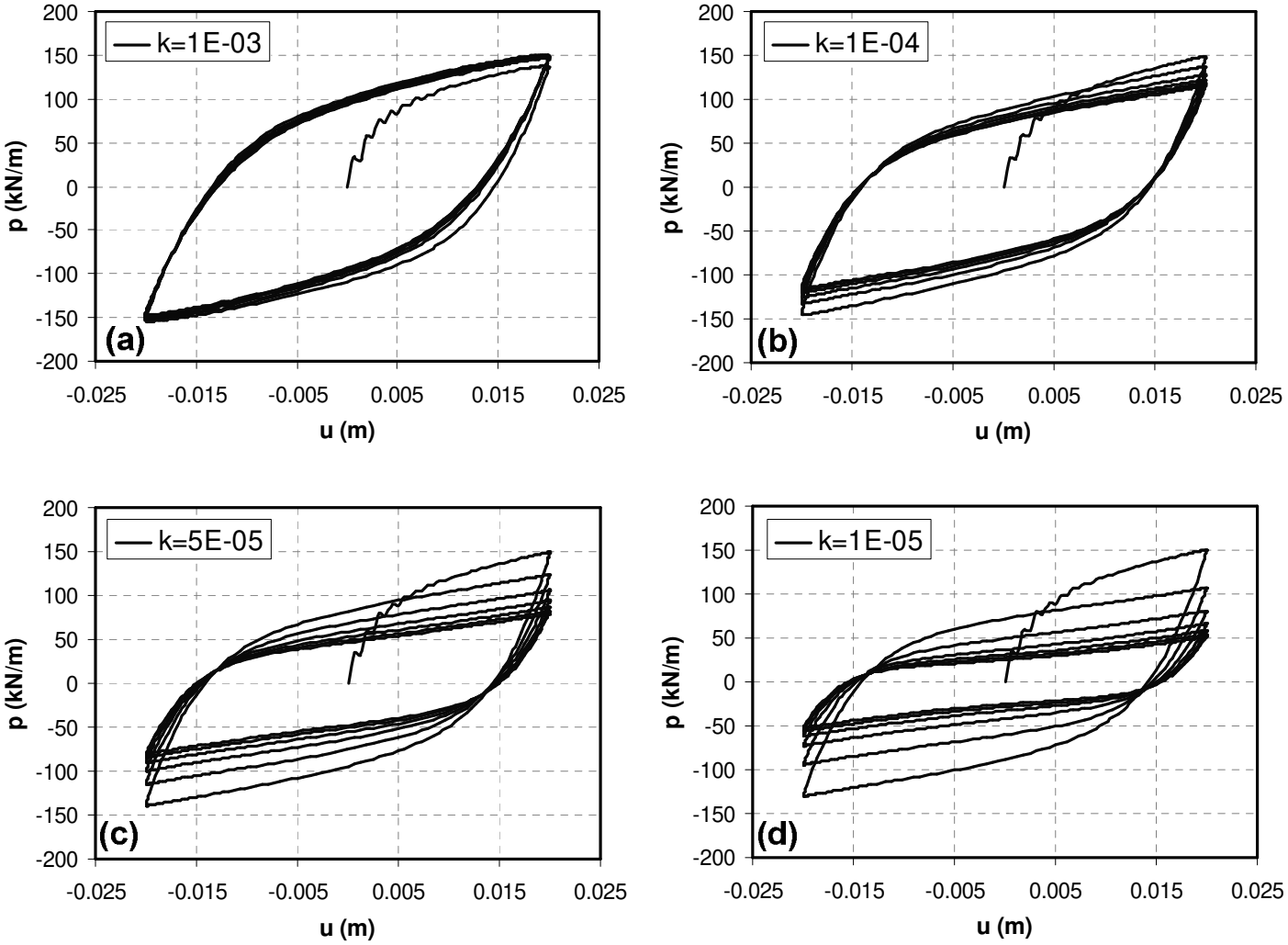

Figure 4.2 (a)-(d) Variation of pile response with soil permeability

More specifically, during steady state, the rate of increase in pore-pressures equals the rate of dissipation causing the average soil effective stress in the immediate vicinity of the pile during a cycle of loading to remain constant. And while the rate of pore pressure buildup is a function of the amplitude and frequency of loading, the pore-pressure dissipation is partially achieved via radial flow away from the pile, and this phenomenon is controlled by hydraulic conductivity of soil. This was verified by the fact that the same response was observed by keeping the ratio of permeability and frequency the same for very low frequencies, for which the effects of radiation damping are insignificant.

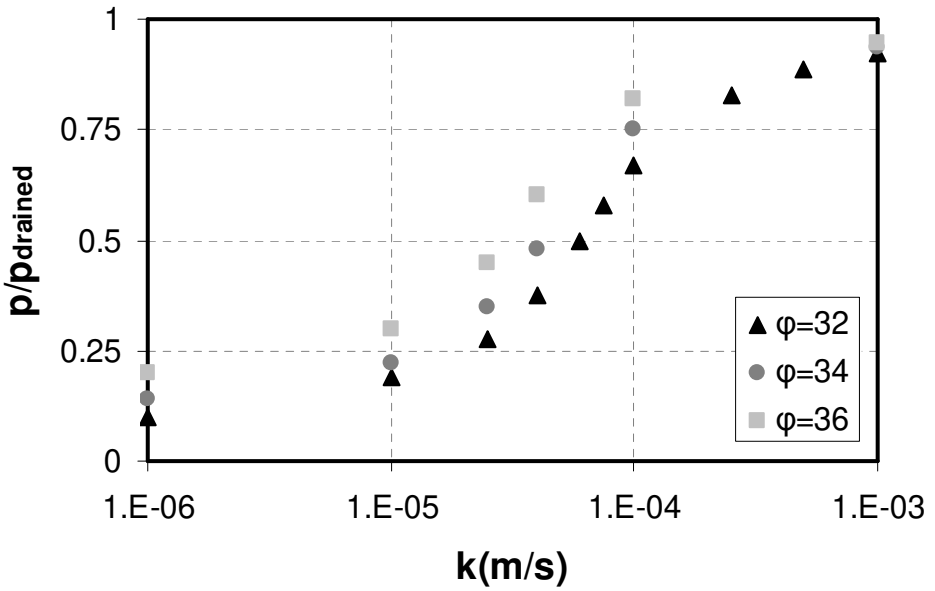

Figure 4.3 Normalized steady state response for different dilation angles as a function of soil permeability

Furthermore, it is observed that the steady-state response depends on the dilation angle (δ) as well. Figure 4.3 shows the steady state response for a partially drained case normalized with respect to drained response ($p / p_{drained}$) as a function of soil permeability for different dilation angles. Soils with higher dilation angle retain higher percentage of their original strength at lower permeability compared to others. While at k=10^{-6} m/s, soil with $\delta = 2^{\circ}$ looses 90% of its strength, soil with $\delta = 6^{\circ}$ still retains around

20% of its original strength. This observation agrees well with those from centrifuge tests by Wilson at el. [55] where medium-dense sands were found to retain much higher (25-30%) of their original strength compared to loose sands (10%) during liquefaction.

Effect of Initial Effective Overburden Stress (σ')

The variation of pile response with increasing depth (in terms of pile diameter) is shown in Figure 4.4(a)-(d). While the liquefaction resistance parameter for all depths is the same (χ=0.15), the soil at lower depth (0.5B) liquefies earlier (in about 3 cycles) as compared to soil at depth D=2B that reaches liquefaction after 6 loading cycles. For displacement levels between -5 mm to 5 mm, the soil resistance is attributed primarily to the drag force exerted by the liquefying soil flowing around the pile and is observed to be almost constant at $p \approx 10$ kN/m, irrespective of the depth. Given the pile diameter of B=1m in the model, this observation matches very well with Abdoun et al. [52] and Dobry et al. [81], who recommended a depth independent constant lateral pressure of 10.3 kPa for liquefied sands based on centrifuge observations.

However, once phase transformation takes place in the soil surrounding the pile, the residual resistance increases with increasing depth, an observation in agreement with the recommendation by JRA [51] according to which lateral forces exerted by liquefied soils are proportional to the depth of soil below ground surface. The magnitude of residual resistance predicted in our simulations is quite high compared to 30% of overburden pressure recommended by JRA, which is attributed to the fact that: (a) excess pore pressure ratio falls below 1.0 once phase transition takes place, and the soil in the near-field is no longer completely liquefied, and (b) the soil in the far-field is also not liquefied in our parametric simulations, by contrast to an actual case of lateral spreading where both the near and far-field material are in liquefied state.

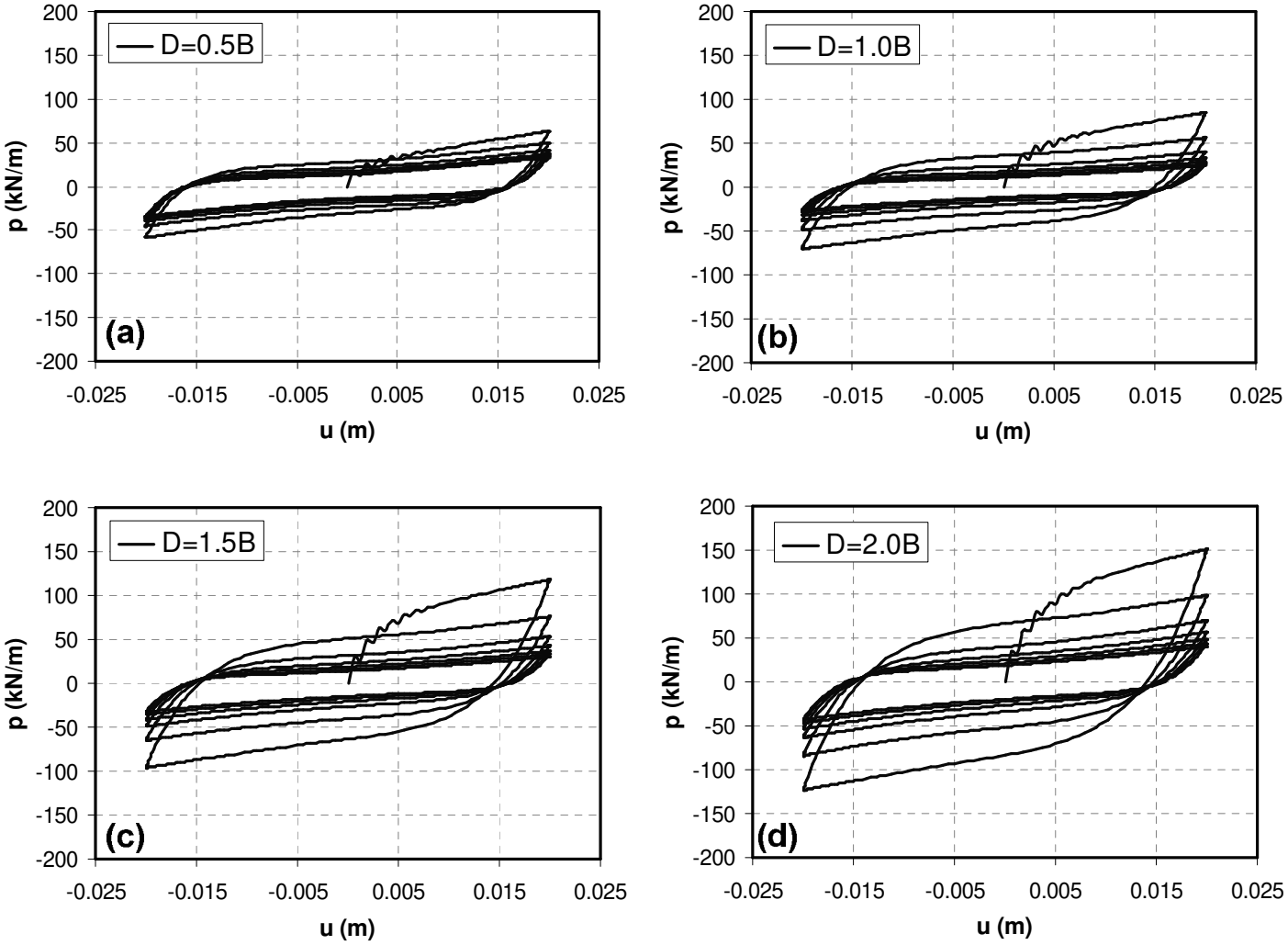

Figure 4.4 (a)-(d) Variation of pile response with depth (in terms of pile diameter)

Effect of Liquefaction Resistance Parameter (χ)

The plastic potential function used for the non-linear soil model in our simulations is given as $P = P' + \delta P'''$, where P' is the deviatoric component (associative) and P''' is the volumetric component (non-associative) expressed in terms of mobilized stress ratio $\eta = q / p'$ as

$$3P''' = \frac{(\eta / \bar{\eta})^2 - 1}{(\eta / \bar{\eta})^2 + 1} \chi \tag{4.1}$$

where $\bar{\eta}$ is a material parameter related to critical state friction angle (φ_{ss}) for triaxial compression (C) and triaxial extension (E) as $\bar{\eta}_{C/E} = \pm 6 \sin \varphi_{ss} / (3 \mp \sin \varphi_{ss})$. The liquefaction resistance parameter, χ (also called dilation parameter), is a scaling parameter for plastic dilation, and depends on the relative density and sand type (fabric, grain size). Detailed description of the procedure to determine χ using liquefaction resistance data (cyclic stress ratio vs. number of cycles to liquefaction) can be found in Popescu [82]; note that the liquefaction resistance curve may be obtained from laboratory testing of soil samples or estimated via correlations with field test data.

The effect of liquefaction resistance of the soil directly translates to the liquefaction resistance of the macroscopic pile response as seen in Figure 4.5(a)-(d); results are shown for the liquefaction resistance parameter ranging between 0.0-0.15. The higher the liquefaction resistance parameter, the higher the rate of generation of excess pore pressure, and therefore the higher the degradation in pile response for each cycle.

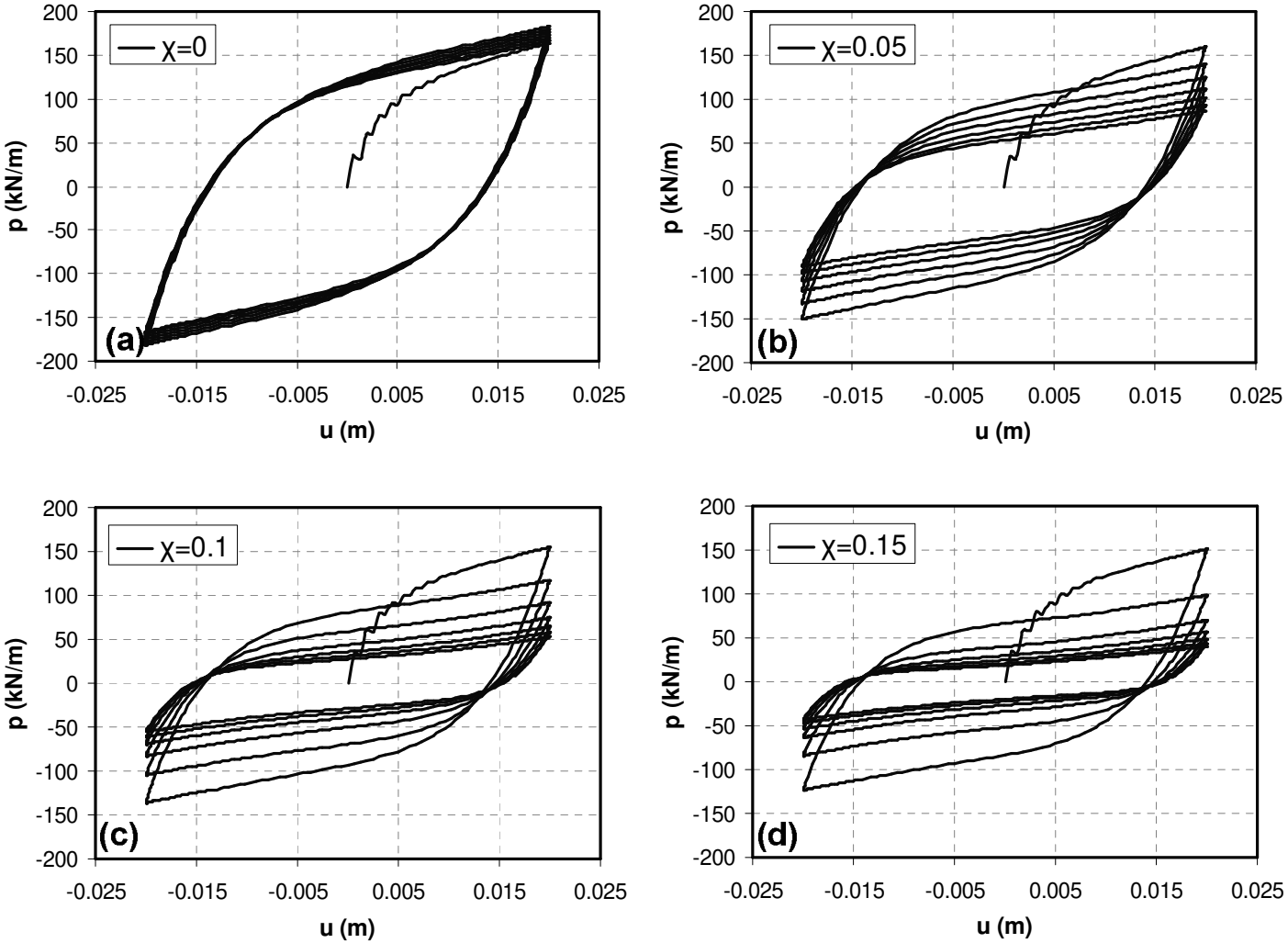

Figure 4.5 (a)-(d) Variation of pile response with liquefaction resistance parameter

Effect of Displacement Amplitude of Cyclic Loading (u)

We here investigate the effect of displacement amplitude of cyclic loading on the pile response. The pile was subjected to different loading amplitudes ranging from 10 mm to 50 mm and the obtained response is shown in Figure 4.6(a)-(c). For u=10 mm, the imposed strain on the soil is low and the soil shows only contractive tendency up to 5 cycles; subsequently, slight strain hardening is observed. On the other hand, for u=50 mm, significant strain hardening due to dilatancy can be observed starting from the second cycle of loading. This phenomenon can be observed more clearly when the response is plotted as resistance normalized with initial vertical effective stress, $r = p / B\sigma_v'$ against resistance normalized with drained case, $S = p / p_{drained}$ (Figure 4.7). It should be noted here that S in this case represents the average effective confining stress in the vicinity of pile.

Two important observations made from this plot are:

(a) The load at which phase transition is observed is directly proportional to effective stress in vicinity of the pile (S). The slope of this phase transition line is independent of amplitude of loading; and

(b) The rate at which the effective stress ratio (S) decreases with each loading cycle is different for different loading amplitudes, however it remains more or less the same for u=20mm and u=50mm. This implies that after the soil in vicinity of the pile has undergone phase transition into the dilative zone, further shearing doesn't contribute much to accumulation of excess pore pressures.

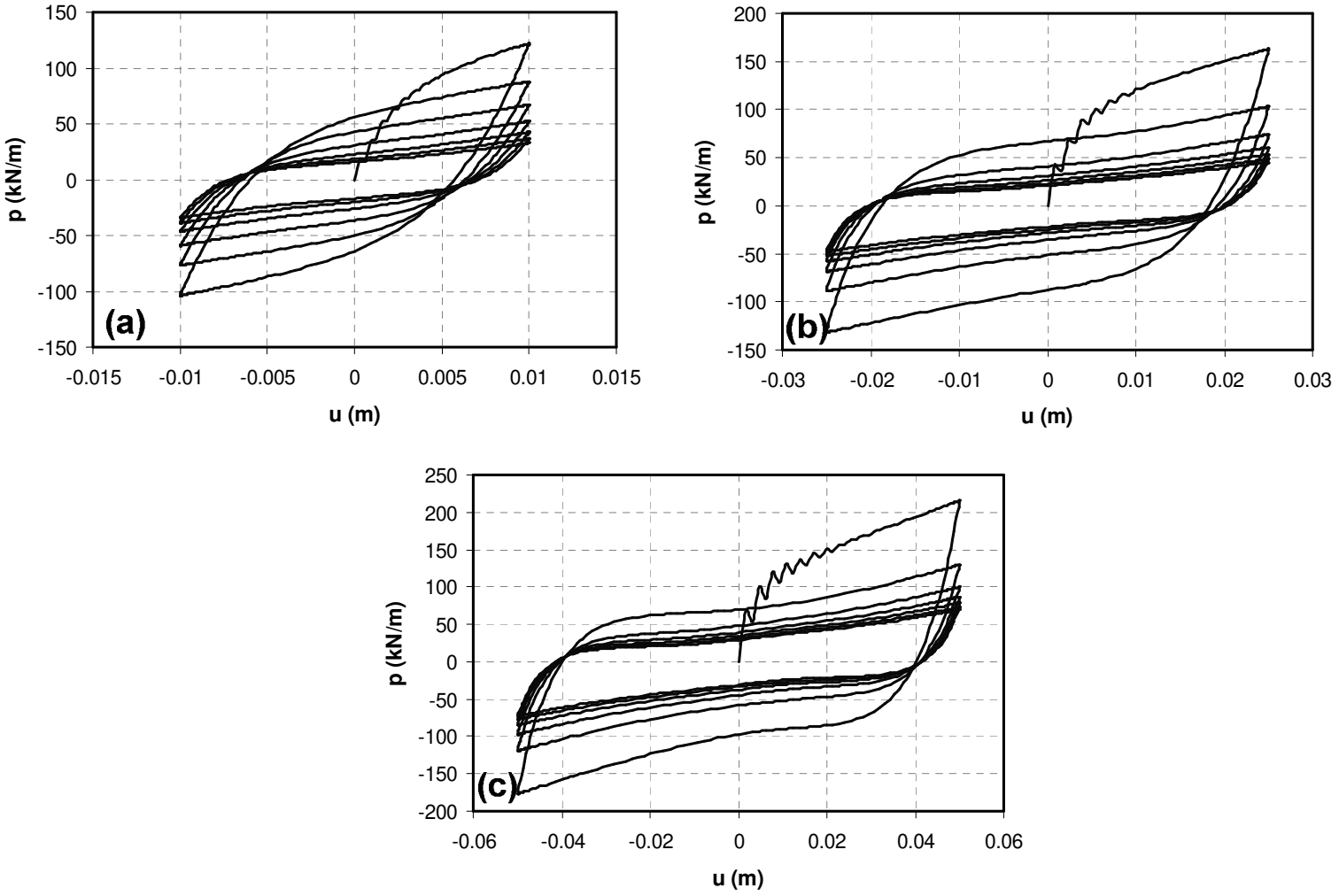

Figure 4.6 (a)-(c) Variation of pile response with amplitude of cyclic loading

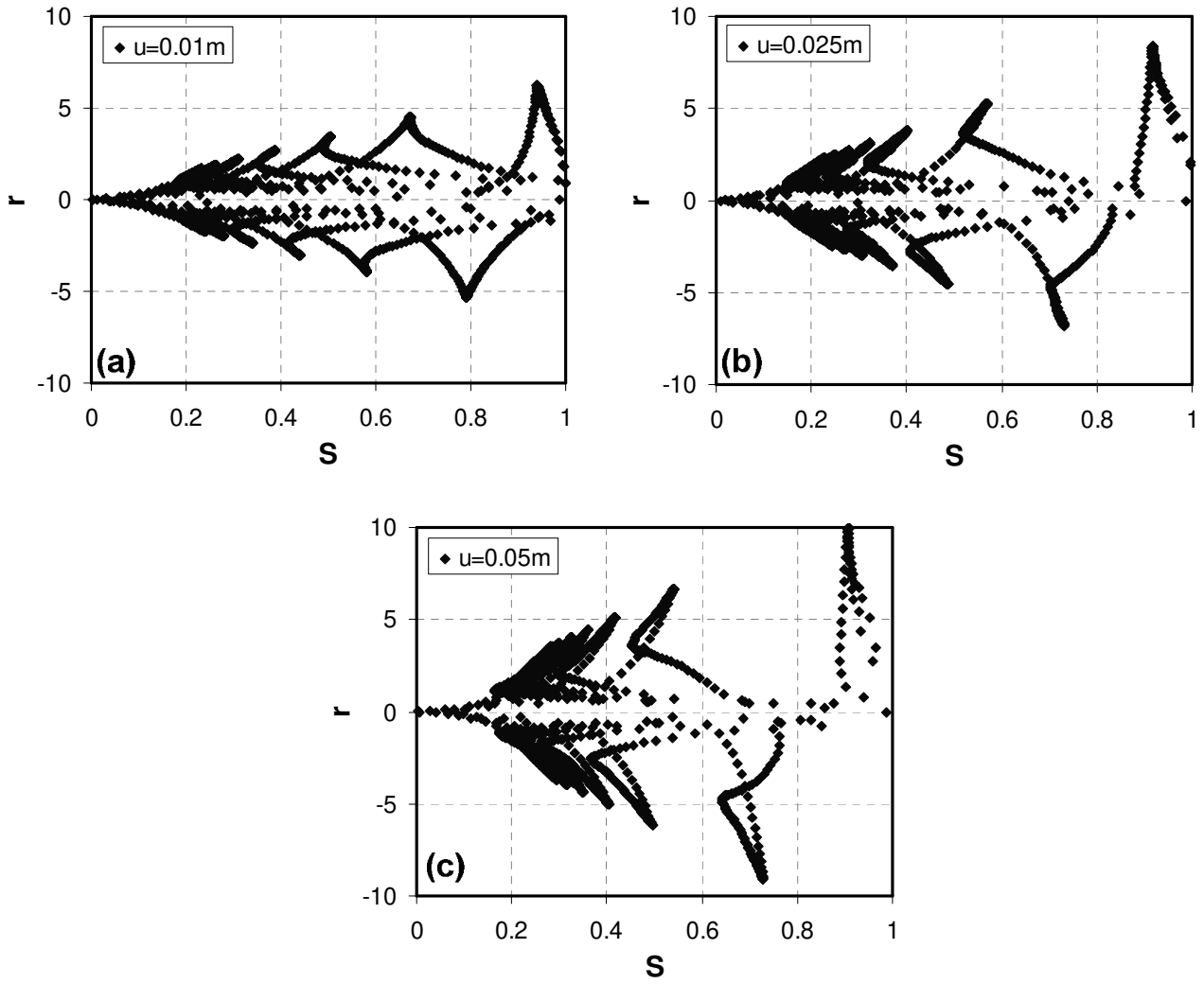

Figure 4.7 Pile response in normalized r-S domain as function of cyclic displacement amplitude.

Effect of Frequency of Cyclic Loading

The cyclic loading frequency has a two-fold effect on the macroscopic pile response. First, the rate of loading governs the rate of pore pressure generation and hence the steady state response as discussed in the permeability section. More importantly, however, the loading frequency controls the radiation damping, namely the energy propagating away from the soil-pile interface towards the far-field (i.e. energy redistribution in larger soil volume). To isolate the effects of soil non-linearity on radiation damping and avoid any interference due to difference in rate of pore pressure generation, the simulations for this section are performed in dry soil, i.e., without solid fluid coupling. Figure 4.8(a)-(d) shows the pile response for dilation angle δ=2, corresponding to loading frequencies f = 1, 2, 4 and 5 Hz, respectively.

The following observations are made:

(a) As the loading frequency increases, the amount of energy dissipated, i.e., the area enclosed by the loop also increases. This is expected since radiation damping increases with loading rate;

(b) There are no clearly demarcated regions of unloading-reloading since the stiffness and damping response are 90 degrees out of phase. While one is decreasing (unloading), the other one is increasing (loading) and vice-versa;

(c) The dynamic stiffness modulus is higher than the quasi-static, and increases with increasing frequency. This is also an observation expected, since for the dynamic case, the complex stiffness modulus is given as $K_{dynamic} = K_{static} + i\omega C$ which is higher in magnitude than the static stiffness modulus.

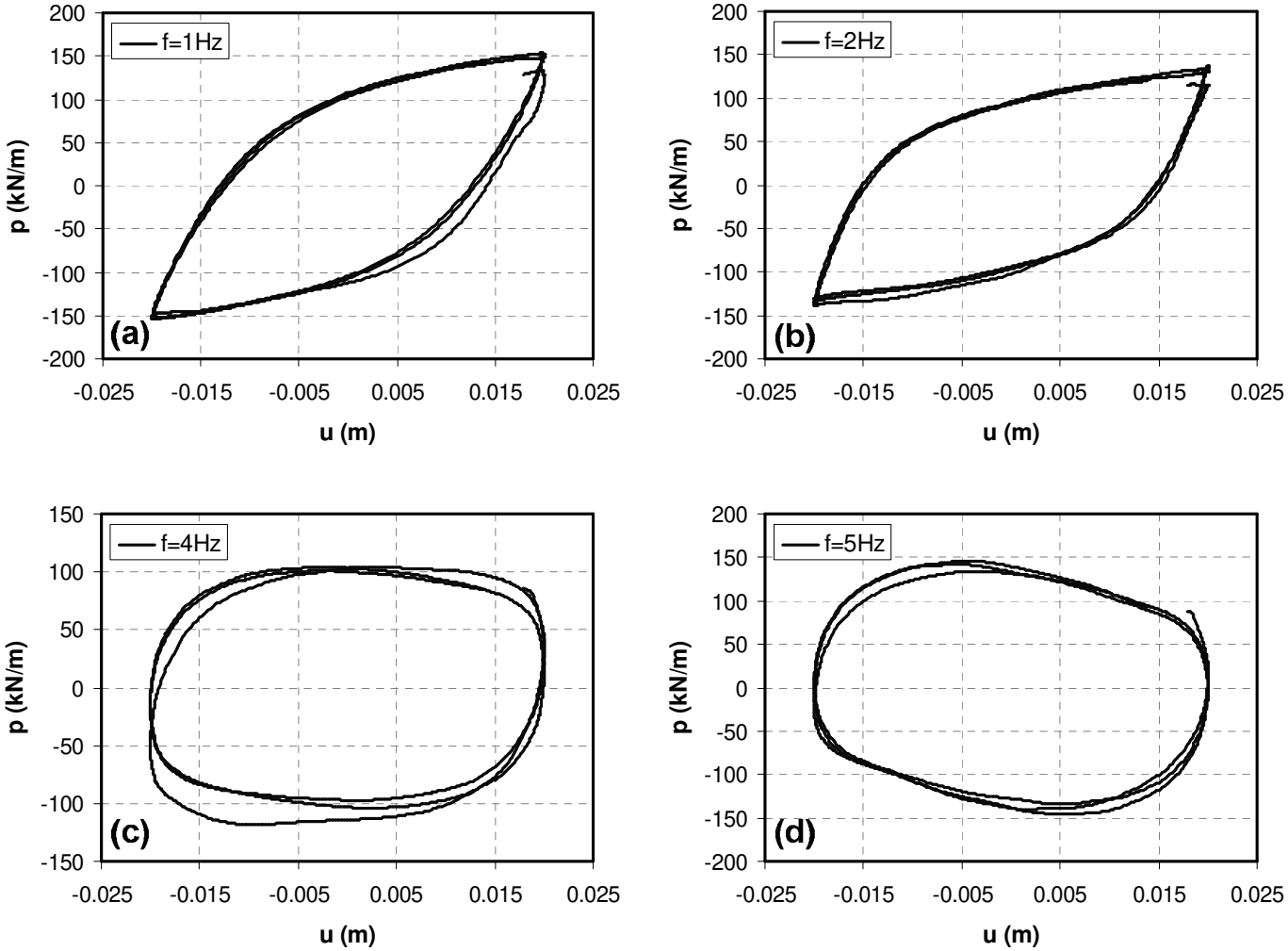

Figure 4.8 (a)-(d) Variation of pile response with cyclic loading frequency

CHAPTER 5

MACROELEMENT FORMULATION

Results of the parametric investigation suggest that the total resistance as seen from the pile centerline is a function of the effective stress distribution around the pile, which in turn is a function of permeability of the soil and the frequency of loading. Based on this observation, we propose a macroscopic constitutive model to capture pile response in dry soil. We next modify the response by means of a pore pressure generator to account for the response in drained and partially drained conditions.

Drained / Dry Loading

To model the response of a pile subjected to lateral loading in dry / drained soil conditions, a modified Bouc-Wen type hysteresis model (Bouc [83]; Wen [84]) is used. Similar models have been implemented in the past by Badoni & Makris [85] for modeling seismic response of pile foundations and by Gerolymos & Gazetas [49] for the lateral response of caisson foundations. The governing equation for the quasi-static case is given as:

$$p = p_y \zeta \tag{5.1}$$

where p_y is the ultimate lateral resistance and ζ is a hysteretic dimensionless quantity controlling the nonlinear behavior of the lateral soil reaction, computed incrementally by the following expression:

$$d\zeta = \left\{1 - f_\zeta \left[b + g\,\text{sign}(du.\zeta)\right]\right\}\frac{du}{u_y} \tag{5.2}$$

where $u_y = p_y / K$ is the yield displacement, K is the initial stiffness, du is the incremental relative displacement between the pile and the free-field at the location of macroelement, $b = 1 - g$ are parameters controlling unloading and reloading stiffness, $sign(x) = -1$ if x $<$ 0 and +1 if x $\geq$ 0 is the sign function, and f_ζ is a monotonically

increasing function of ζ such that $f(\zeta)=1$ when $\zeta=1$ and $f(\zeta)=0$ when $\zeta=0$. For the original Bouc-Wen model, $f(\zeta)=|\zeta|^n$.

A dashpot is added to the model to simulate radiation damping caused by energy dissipation and redistribution effects. The dashpot can either be placed in "parallel" or "series" with the spring. However, Wang et al. [86] showed that parallel arrangement can result in excessive forces when loaded in highly non-linear range unless an upper bound is ensured for this case. For this purpose, Badoni & Makris [85] put a maximum limit equal to the value at yield displacement to avoid overestimating the response at large displacements. On the other hand, Boulanger et al. [47] used the "series" approach in their p-y element by putting the dashpot in "parallel" with elastic stiffness spring and in "series" with the plastic spring, so that the total response never exceeds the ultimate soil strength. A "parallel" approach would imply that at maximum displacement level during sinusoidal cyclic loading, the soil resistance should be almost the same for all loading frequencies since the loading rate at maximum displacement is zero and hence there is no contribution to resisting force from the dashpot. However, results from Figure 4.8 show that the soil resistance at maximum displacement level decreases as the loading frequency increases, which is something that is expected from "series" model instead. Therefore, a formulation similar to "series" arrangement is used in our model implemented as follows: The total resistance is calculated in an incremental fashion as

$$dp = dp_s + dp_d = p_y d\zeta_s + p_y d\zeta_d \tag{5.3}$$

The quantity $d\zeta_s$ is calculated as described by equation (3), and the incremental dashpot force is given as:

$$dp_d = c_r d\dot{u} \tag{5.4}$$

where c_r is the radiation damping coefficient; to account for the soil nonlinearity effects on radiation damping, c_r is approximated iteratively using an equivalent linear approach

(i.e. using the linear formulation in conjunction with the tangent modulus of the stress-strain hysteresis loop instead of the elastic stiffness) by modifying the linear damping coefficient by Makris and Gazetas [87] as follows:

$$c_r = c\left[1 - f_\zeta\left(b + g\,\text{sign}(du.\zeta)\right)\right]^{0.5}$$
$$c = \rho_s V_s a_o^{-0.25} QB \tag{5.5}$$

where ρ_s is the density of soil, V_s is the shear wave velocity in soil, B is pile diameter, $a_o = \omega B / V_s$ is the normalized frequency of loading, and Q is a shape factor that depends on the soil Poisson's ratio but can be approximately set to $Q \approx 3$ for shallow depths (Badoni & Makris [85]). In case of transient loading, ω is set equal to the dominant frequency of loading. The non-linear formulation ensures that when $\zeta = 1$, $c_r = 0$ and hence the total force never exceeds the ultimate resistance of soil.

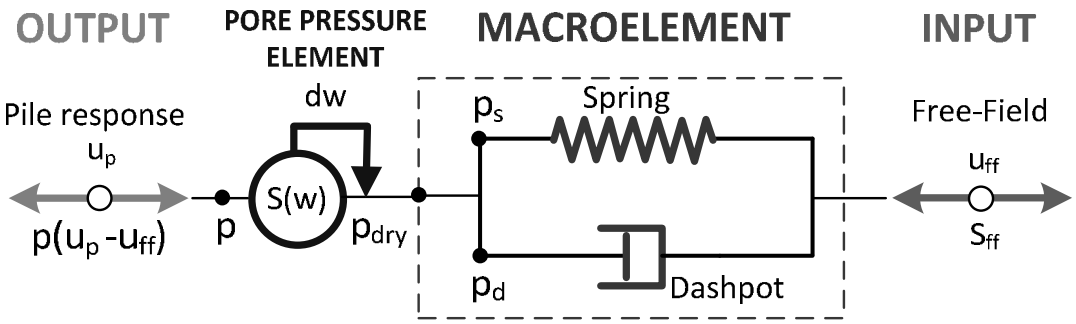

Figure 5.1 Schematic showing the different components, input and output for proposed macroelement

Undrained Loading

We next integrate the effects of effective stress changes on the soil-pile response. For this purpose, the drained response is modified by means of a pore pressure generator. The average effective stress in the vicinity of the pile is evaluated by using the 'liquefaction front' concept developed by Iai et al. [88] and extending it for the case of piles as shown in Figure 5.2.

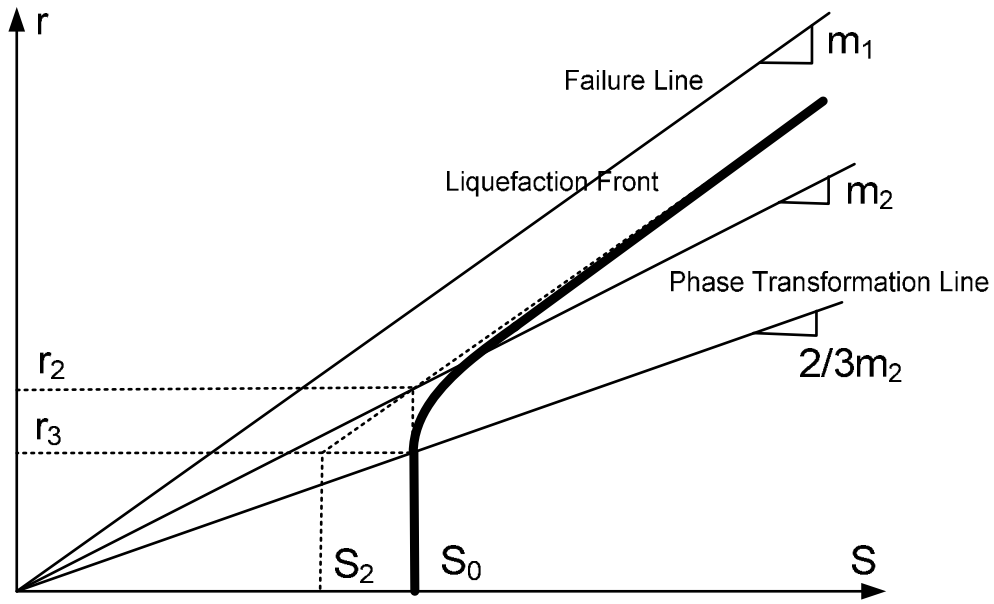

Figure 5.2 Extension of concept of "Liquefaction Front" for piles in r-S space

This approximation is based on the observation that the pore pressure generation is directly proportional to the total amount of plastic shear work done per unit volume of soil (Towhata and Ishihara [89]). As a result, the average effective stress $S = \sigma_v' / \sigma_{v0}'$ can be written in terms of normalized soil resistance $r = p / B\sigma_i'$ as follows:

$$S = \begin{cases} S_o & (r \le r_3) \\ S_2 + \sqrt{\left(S_o - S_2\right)^2 + [(r - r_3)/m_1]^2} & (r > r_3) \end{cases} \tag{5.6}$$

where $S_2 = S_0\left(1 - m_2 / 3m_1\right)$, $r_3 = 2S_0 m_2 / 3m_1$, m_1 is the slope of failure line and m_2 is the slope of phase transformation line. S_0 is defined in terms of normalized plastic shear work (w), parameter controlling liquefaction resistance (w_1) and parameter controlling the shape of strength degradation curve (κ) and is calculated incrementally as follows:

$$S_0 = \exp\left(\frac{w}{w_1}\right)^{\kappa} \tag{5.7}$$

$$dS_0 = \kappa S_0 (-\log S_0)^{(\kappa-1)/\kappa} dw / w_1 \tag{5.8}$$

The quantity dw is the normalized incremental plastic shear work, and is calculated as the difference between total incremental shear work and elastic incremental shear work normalized by the product of ultimate soil resistance and yield displacement (see Equation 10). Since the results from our parametric investigation on cyclic displacement amplitude indicate that the amount of plastic shear work done when the soil is in "dilation" doesn't contribute significantly to the build-up of excess pore pressure, only the plastic shear work done in "contractive" zone is used as follows:

$$dw = \begin{cases} \dfrac{dW - dW_e}{p_y u_y} = \dfrac{p.du - p.(dp/K)}{p_y u_y} & r \le r_3 \\ 0 & r > r_3 \end{cases} \tag{5.9}$$

According to Iai et al [32], a drawback of the formulation in equation (5.6) is that it becomes unstable when the r-S curve approaches the failure line; for the macroelement, this implies that when $\zeta = 1$, $S/S_0 \to \infty$. To avoid this problem and improve the response idealization obtained in parametric analysis, we impose the condition that the failure slope m_1 be increased by a factor of $1.05 + 0.4S_0$. In this way, the increment of 0.05 of the intercept bounds the total response and avoids numerical instability at $\zeta = 1$, while the $0.4S_0$ term prevents overestimation of dilation response when the soil in the vicinity of pile is not liquefied.

Partially Drained Loading

Gonzalez et al. [66] among others reported that the interaction between pile and soil during liquefaction leads to the formation of a zone around the pile where pore pressures are considerably different from those in the far-field. This difference has been attributed to both dilation effects in the soil as well as suction on the 'tension' side of pile. These observations agree with the concept of near-field where soil-structure interaction causes deviations in stress, pore pressure and displacements from the corresponding quantities in the far-field. We observed a similar phenomenon in our

numerical analyses, namely that the liquefaction caused by the relative soil-pile motion was confined within a zone of about five diameters around the pile as shown in Figure 5.3. Due to the pressure difference between near-field and far-field, drainage initiated between the two regions depending on the pressure gradient.

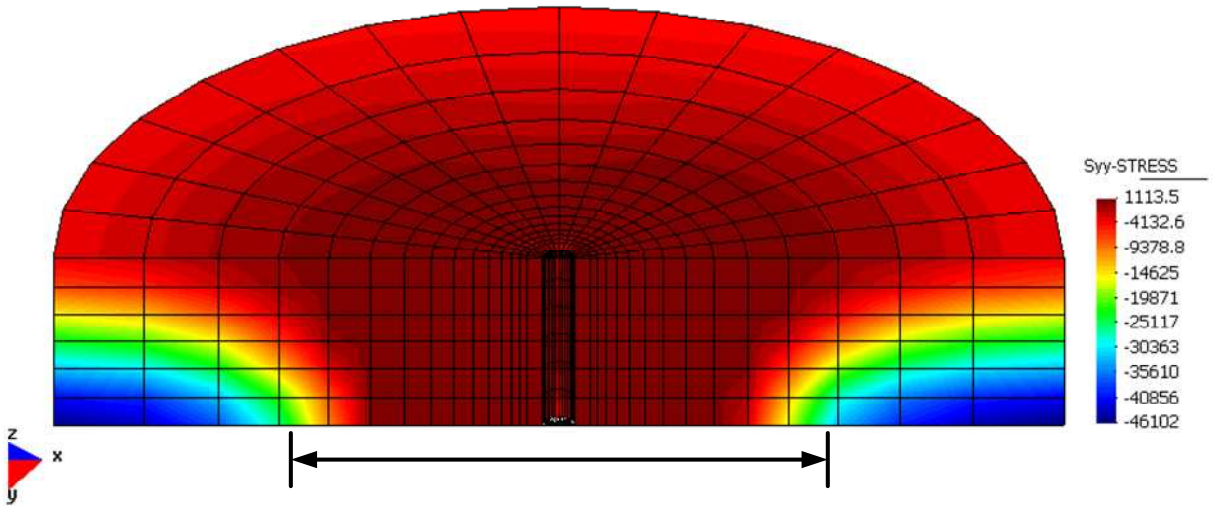

Figure 5.3 Effective vertical stress plot after seven loading cycles showing the formation of local liquefaction zone

To account for the effects of partial drainage, it is assumed that there is a linear pressure gradient between the near-field and the far-field in the radial direction, and that Darcy's Law may be applied. The drainage velocity is thus given as:

$$V = k\frac{\Delta h}{L} = \frac{k}{L}\sigma'_{v0}\left(S_{ff} - S\right) \tag{5.10}$$

where k is the permeability of soil, S_{ff} is the effective stress ratio in free-field and the drainage length $L \propto B$. We also know that

$$V \propto \frac{d\varepsilon_v}{dt} \propto \frac{dS_0}{dt}\frac{1}{K_s} \tag{5.11}$$

where ε_v is the volumetric strain released due to outflow of water, and K_s is the bulk modulus of soil. Since $K_s \propto S^n$, the expression above can be modified and written in implicit form as:

$$dS_0 = \frac{\beta.dtS^n}{1+\beta.dtS^n}\left(S_{ff} - S\right) \tag{5.12}$$

where $\beta = f\left(k/B\right)$.

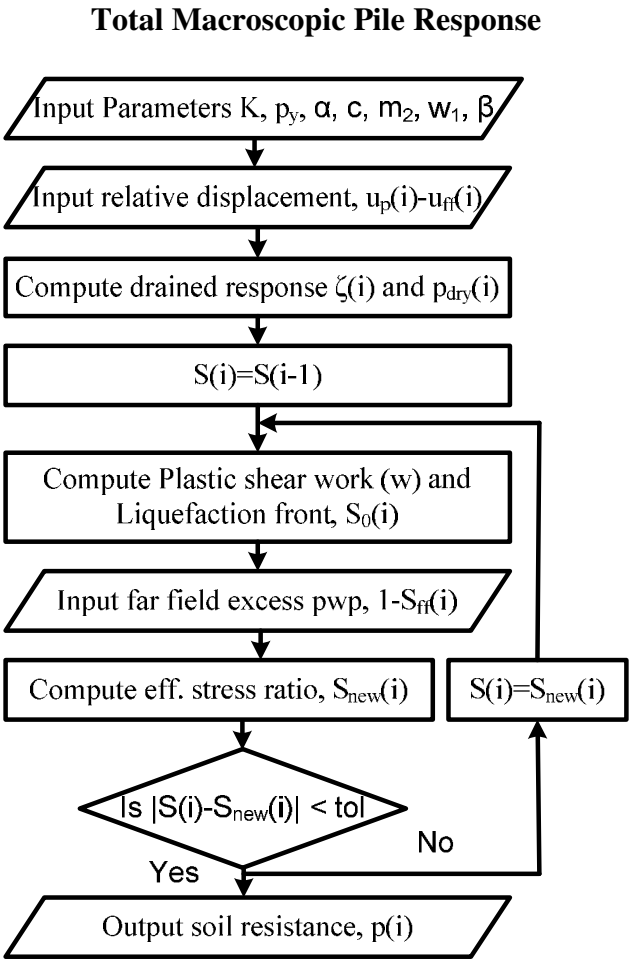

Figure 5.4 Flowchart for calculation of pile response using proposed macroelement

In order to compute the total response, the drained response is first calculated using equation (5.3). The shear work done is calculated incrementally as $dw = p.du/p_y u_y$, and is used to calculate the change in S_0 due to pore pressure generation as described in equation (5.8). The new S_0 is then calculated by adding/subtracting the change in S_0 due to pore pressure generation and dissipation as given by equation (5.12), respectively. Given the current value of ζ, the liquefaction

front parameter S_0, and the shear stress ratio given as $r = m_1 \zeta S$, the current level of average-effective stress ratio (S) is calculated. The total resistance then calculated as $p = p_y \zeta S$. The process is expressed in form of flowchart in Figure 5.4.

CHAPTER 6

CALIBRATION OF MACROLEMENT

Drained Response

To simulate drained conditions, the soil permeability was set to a very high value (k=1m/s) and a very low loading frequency (0.1Hz) was used. Also, to simulate dry conditions, the numerical analyses were performed without using the fluid phase. The results for both cases were found to be in excellent agreement with each other for the same values of effective confining stress. Therefore, in the rest of the paper the drained/dry response is used interchangeably as long as the effective confining stress is the same.

Initial stiffness Modulus (K)

Figure 6.1 shows the initial stiffness modulus of the p-y curves (K) as a function of Young's modulus of the soil (E_s) at different depths and for different reference Young's modulus (E_{s0}).

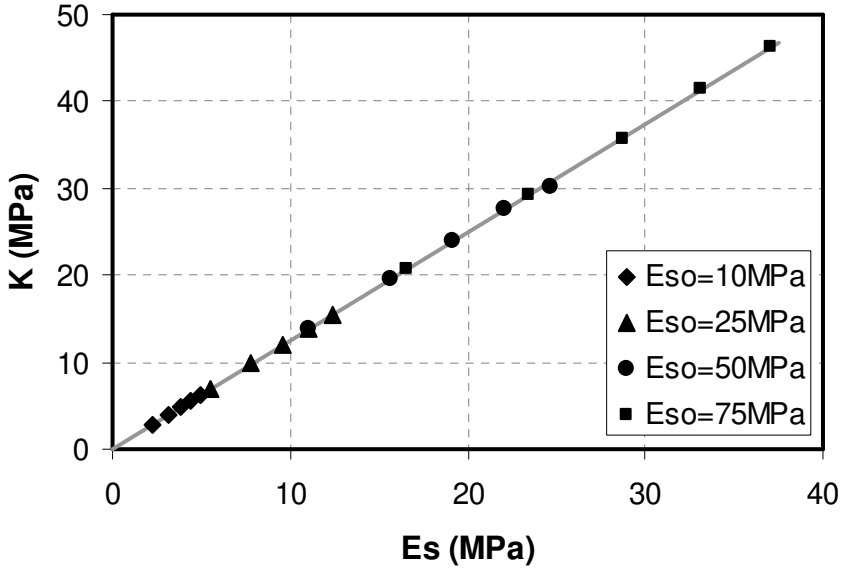

Figure 6.1 Variation of initial stiffness of pile response with Young's modulus for soil

For all cases the stiffness modulus follows the relation:

$$K = 1.25E_s \tag{6.1}$$

This is in excellent agreement with the values proposed in literature (Roesset [90]; Makris and Gazetas [87]) for pseudo-static response of circular piles.

Ultimate Resistance (p_y)

Figure 6.2 shows the normalized ultimate resistance of p-y curves (p_y/σ_v') as a function of the pile diameter. The normalized ultimate resistance is observed to be directly proportional to the pile diameter, which is similar to the formulations $p_y = 3K_pB\sigma'_{vo}$ by Broms [91], and $p_y = K_p{}^2B\sigma'_{vo}$ by Fleming et al. [92] with $K_p = \tan^2(45+\varphi/2)$ being the coefficient of passive earth pressure and φ the friction angle for soil.

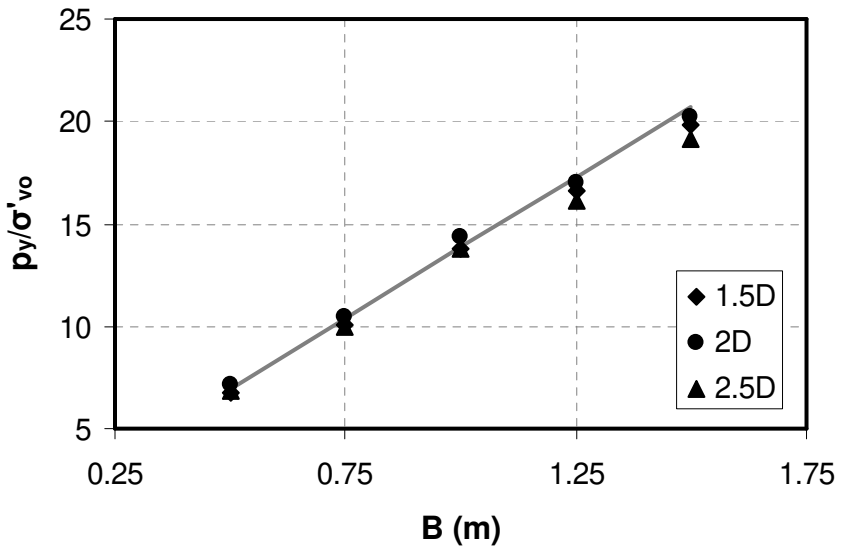

Figure 6.2 Normalized ultimate soil resistance (p_y) as a function of pile diameter

The variation of normalized ultimate resistance with friction angle observed in this study is shown in Figure 6.3. The best-fit curve is obtained as a combination of both aforementioned formulations as:

$$p_y = \left(3.25K_p + 0.3K_p^2\right) B\sigma_v' \qquad (6.2)$$

The coefficient $\left(3.25K_p + 0.3K_p^2\right)$ is slightly higher than $3K_p$ and K_p^2 reported in the literature; the overestimation can be attributed to the fact that there is no gapping (loss of contact) on the tension side of pile while loading in our numerical simulations. While the same formulation is used in this paper for consistency and for the sake of simplicity, other more sophisticated formulations including the one proposed by Reese et al [16] can also be used.

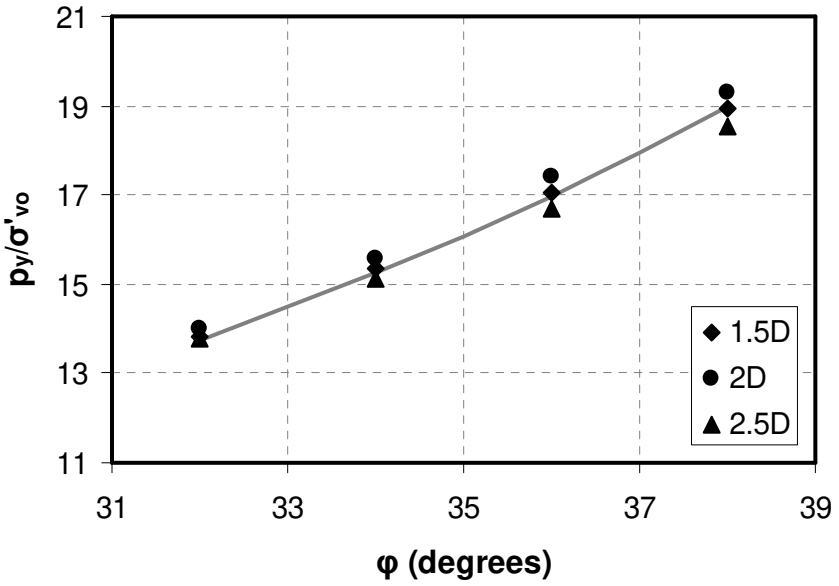

Figure 6.3 Normalized ultimate soil resistance as a function of soil friction angle

Backbone Curve (Monotonic Loading)

Figure 6.4 shows the p-y curves for monotonic loading for different depths and different friction angles. Both soil resistance and displacement are normalized as p/p_y and u/u_y. As long as the reference maximum strain γ_{max} remains constant, the backbone curves in normalized space are the same, i.e, are independent of depth and friction angle. The dependence of backbone curves on γ_{max} is shown in Figure 6.5. As γ_{max} decreases, the response becomes stiffer.

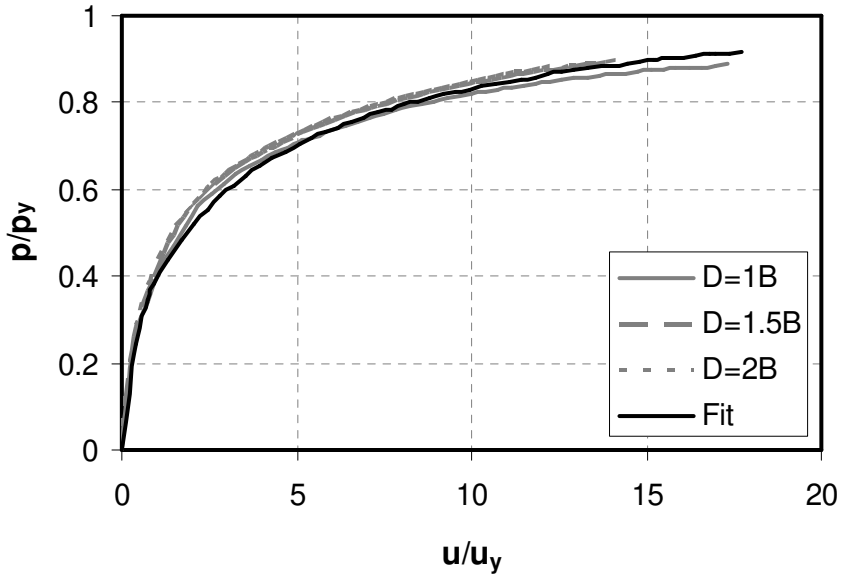

Figure 6.4 Normalized backbone (monotonic loading) curves for pile response at different soil depths

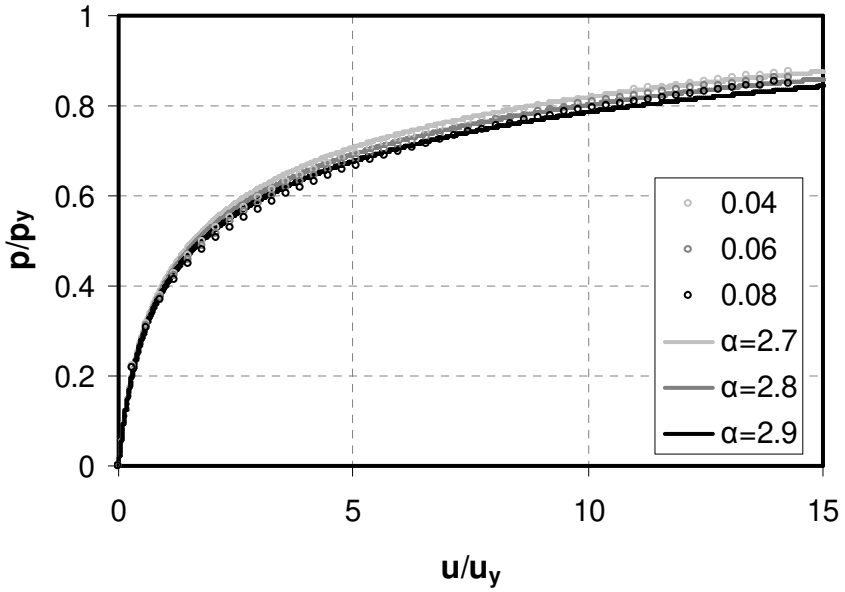

Figure 6.5 Normalized backbone curves as a function of max deviatoric strain in soil along with fitted values using the proposed model

While fitting the backbone curves with the proposed Bouc-Wen model, the function $f(\zeta) = \tanh(\alpha\zeta)/\tanh(\alpha)$ was found to give much better fit compared to the usual function $f(\zeta) = |\zeta|^n$. Since the difference between the backbone curves for

$\gamma_{max} = 0.04 - 0.08$ is not that pronounced, a value of α=2.7 for dense sands (γ_{max}=0.04), 2.8 for medium-dense (γ_{max}=0.06) and 2.9 for loose sands (γ_{max}=0.08) is recommended.

The most widely employed backbone curves for lateral loading of piles in practice are the ones proposed by Reese et al. [16] and later adopted by API [17]. Murchison and O'Neill [93] provided a simpler analytical expression to fit the three-part curve proposed by Reese et al. [16] as $p = p_y \tanh(u/u_y)$ where $p_y = nAp_u$ with n and A being corrections to the ultimate resistance p_u that account for pile shape and depth, respectively. Figure 6.6 shows how the proposed backbone curve compares with the backbone curve recommended by Reese et al. in normalized p-y space. The Reese et al. curve predicts a much stiffer response than actually observed as has been reported before by many other researchers including Yan & Byrne [94].

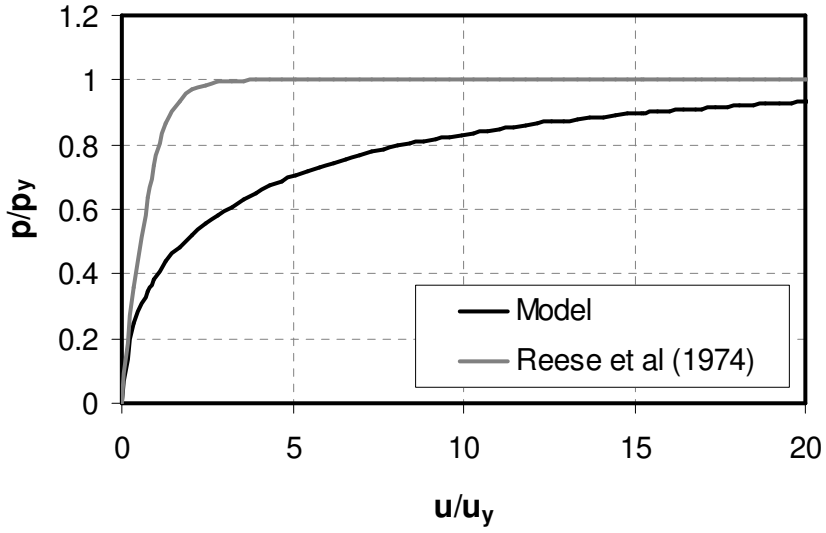

Figure 6.6 Comparison between backbone curves proposed by Reese et al. (1974) and those proposed in this study

Cyclic Loading-Reloading

The pile response when subjected to cyclic loading of different displacement amplitudes is shown in Figure 6.7. The unloading stiffness is observed to be the same as initial stiffness modulus, which implies $b = 0.5$ and $g = 0.5$ for the proposed model. It is

also observed, however, that the modulus starts decreasing during unloading unlike the case of proposed model formulation where it remains constant till reloading, i.e., till the net force has reached zero. However, since the difference is not that significant, a better fit can be obtained by using a slightly reduced unloading modulus with $b = 0.6$ and $g = 0.4$.

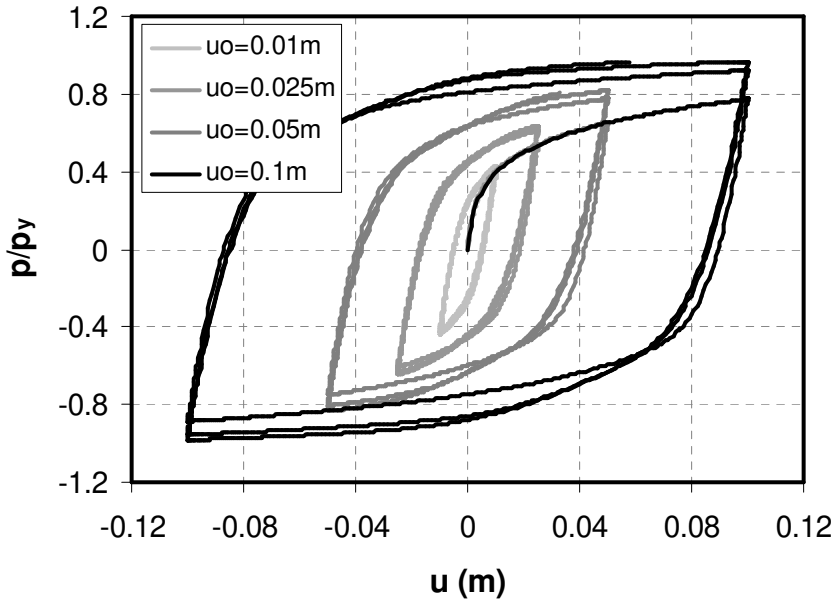

Figure 6.7 Pile response to cyclic loading of different loading amplitude

Figure 6.8 shows the response in a scenario where the pile is loaded monotonically to 0.1 m and then subjected to cyclic loading of magnitude ranging from 0.01 to 0.05 m. The response shows kinematic hardening behavior and as a result, force relaxation is observed after each cycle of unloading-loading. Such kind of kinematic hardening behavior is common in cohesionless soils where the soil collapses and fills up any gap formed behind the pile. As will be shown in later section of paper, the proposed model is able to capture this force relaxation behavior as well.

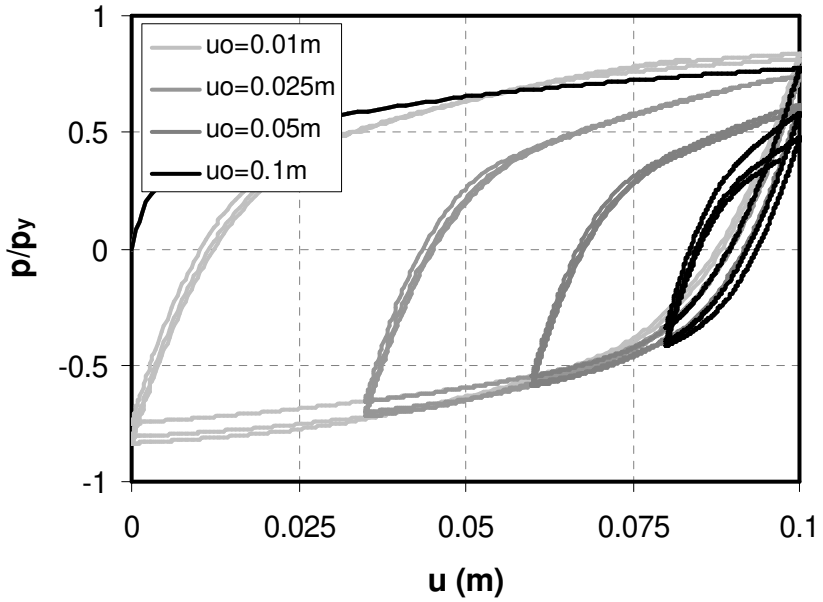

Figure 6.8 Pile response to small loops of cyclic unloading-reloading after monotonic loading

Undrained Response

For the simulation of undrained conditions, the soil permeability was set to a very low value (k=10^{-9} m/s). Simulations were performed for both fully drained and fully undrained cases and the mean effective stress ratio around the pile (S) was calculated as:

$$S = \frac{r}{r_d} \tag{6.3}$$

where $r = p/\sigma_{v0}'B$ is the normalized pile response for the undrained case and r_d is for drained case.

Figure 6.9 shows sample pile response in the r-u domain for both drained and undrained case. Using these curves, the mean effective stress ratio around the pile is calculated and the results are shown in r-S space in Figure 6.10. As loading progresses, the mean effective stress ratio (S) decreases, thereby leading to degradation of pile response (r). But after crossing the phase transformation line, the soil exhibits dilative tendency and strain-hardening is observed.

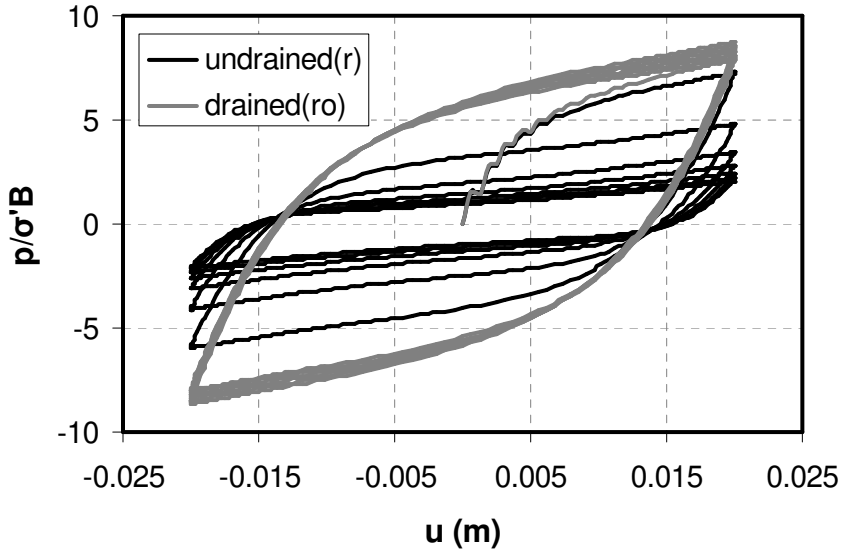

Figure 6.9 Drained and Undrained pile response at depth 2 m in r-u space

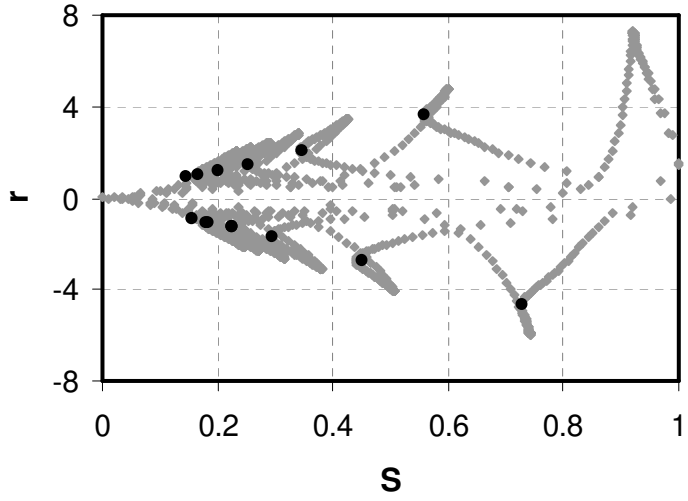

Figure 6.10 Representation of undrained pile response in r-S space (grey) along with points at which phase transition begins (black)

Slope of Phase-transformation Line (m_2)

Figure 6.11 (a)-(d) show the points at which phase-transformation begins in r-S domain for different pile diameters (B), depth below ground surface (D), friction angle (φ) and liquefaction resistance parameter (χ), respectively. It should be noted that according to the proposed model, these points fall along a straight line in r-S space with a slope $m_3 = 0.67 m_2$.

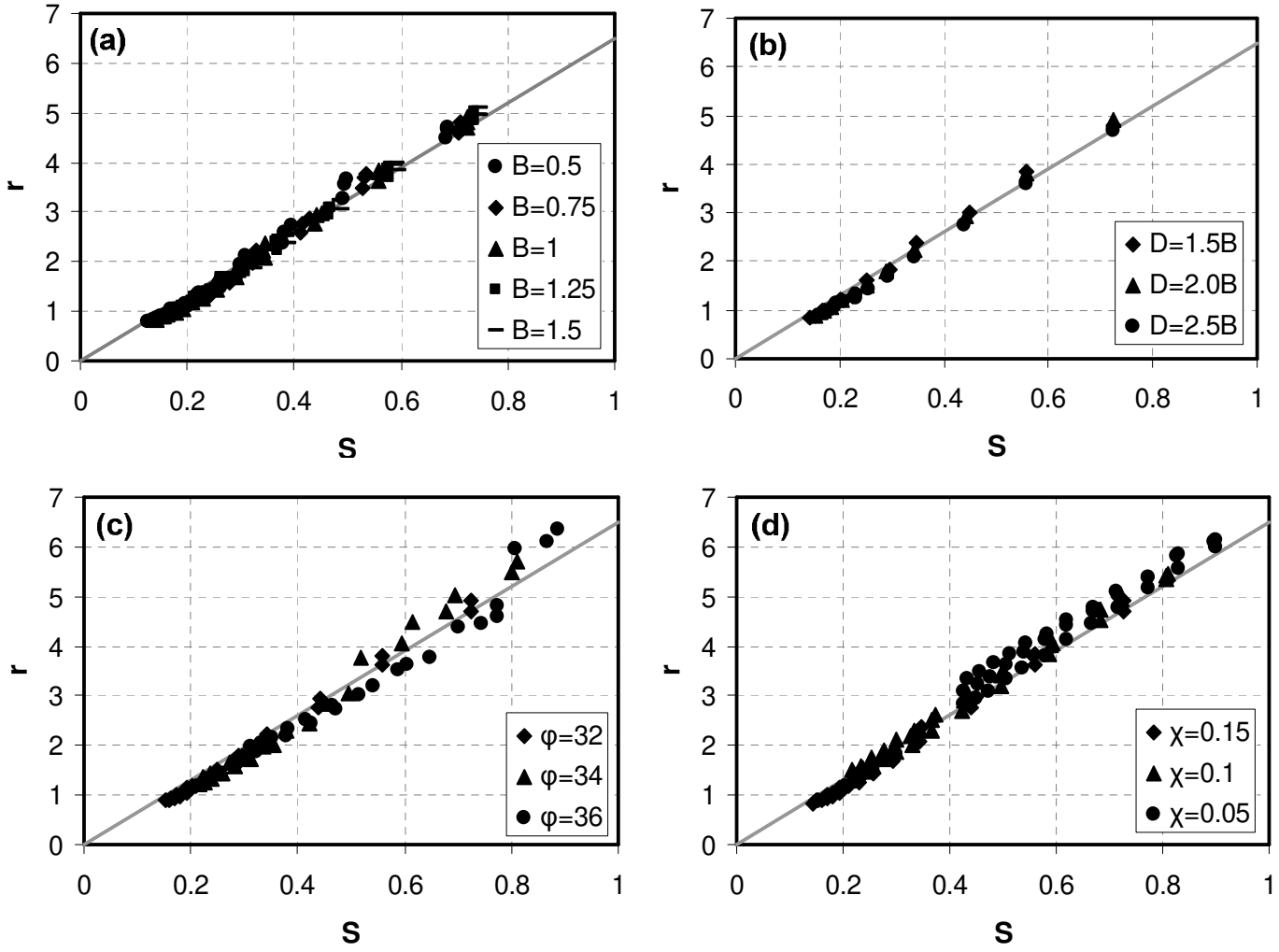

Figure 6.11 Points of beginning of phase-transformation in r-S domain for different (a) pile diameter (b) depth below ground surface (c) friction angle (d) liquefaction resistance parameter

As observed from Figure 6.11, the slope of phase transformation line is independent of all the above mentioned parameters. It is found to be controlled only by the critical state friction angle (φ_{ss}) as shown in Figure 6.12. Along similar lines as compared to slope of failure line, the slope of phase transformation line is fitted as:

$$m_2 = 3.25\tan^2\left(45^\circ + \varphi_{ss}/2\right) \tag{6.4}$$

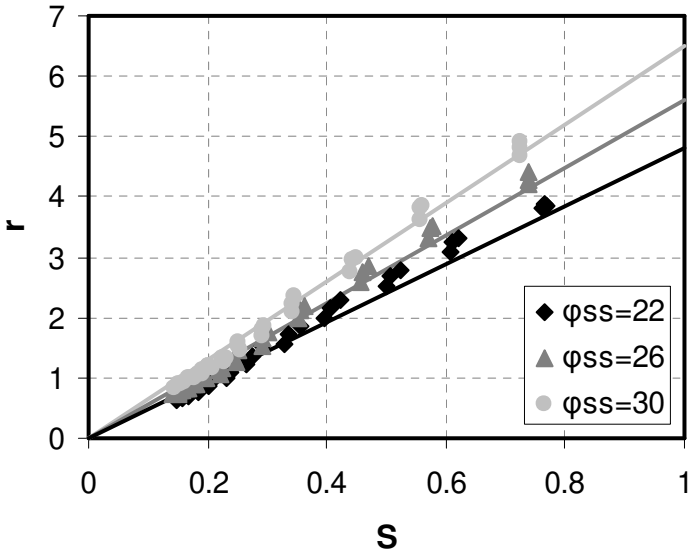

Figure 6.12 Variation of slope of phase-transition line with critical state friction angle. The fitted values are also shown.

Shear Work Correlation Parameter

Figure 6.13 (a)-(c) show the shear work correlation curves, i.e., S_0 vs. w, for different values of critical state friction angle (φ_{ss}), friction angle (φ) and pile diameter (B). While the curves are independent of critical state friction angle and friction angle as expected, they are independent of pile diameter (B) as well. This is because of the fact that while the total shear work done for same value of w increases proportional to B^2 since $p_y \propto B$ and $u_y \propto B$, the volume of soil influenced by pile motion also increases proportional to B^2, thereby keeping the work done per unit volume the same.

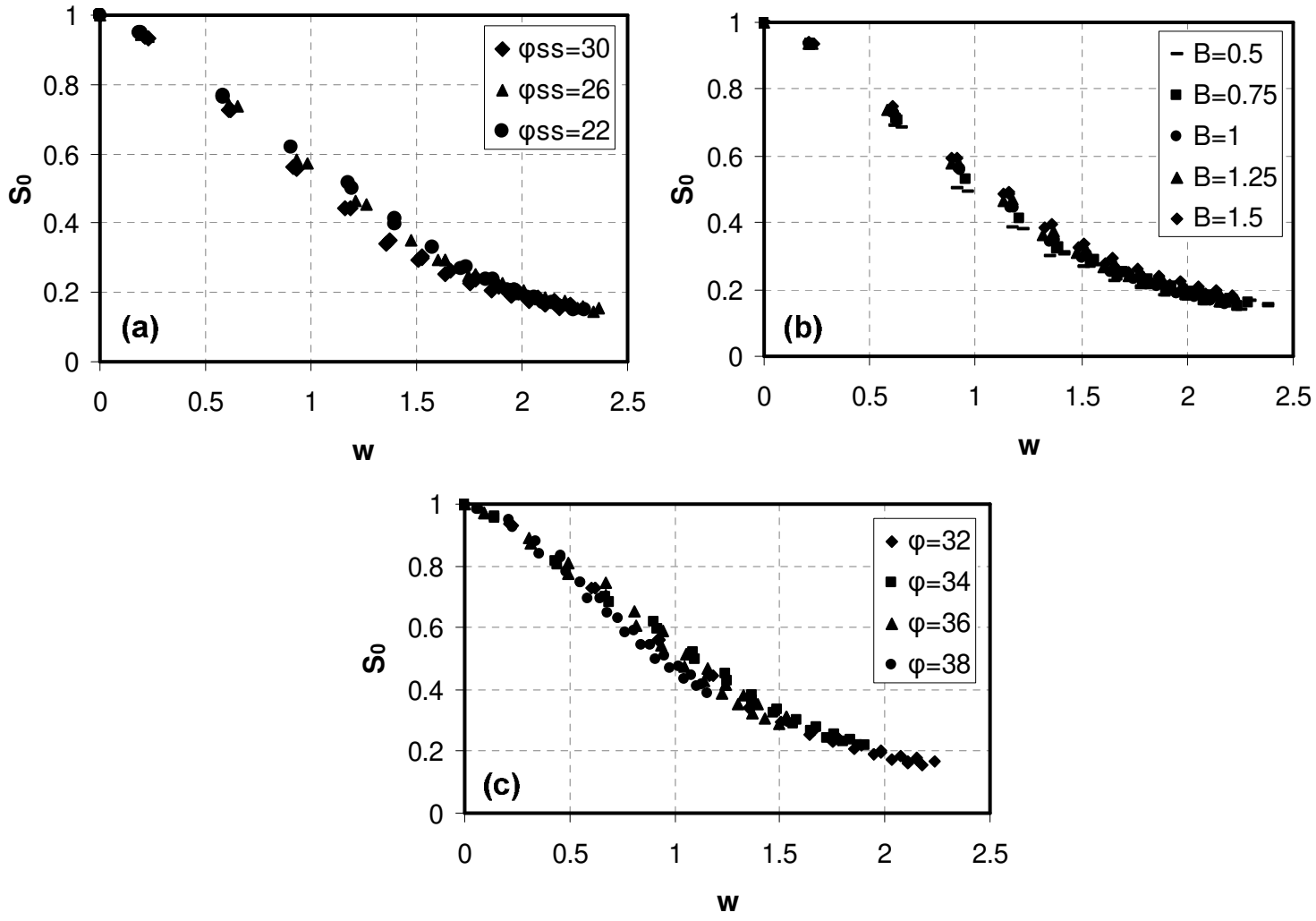

Figure 6.13 Shear work correlation for different values of (a) critical state friction angle (b) pile diameter (c) friction angle

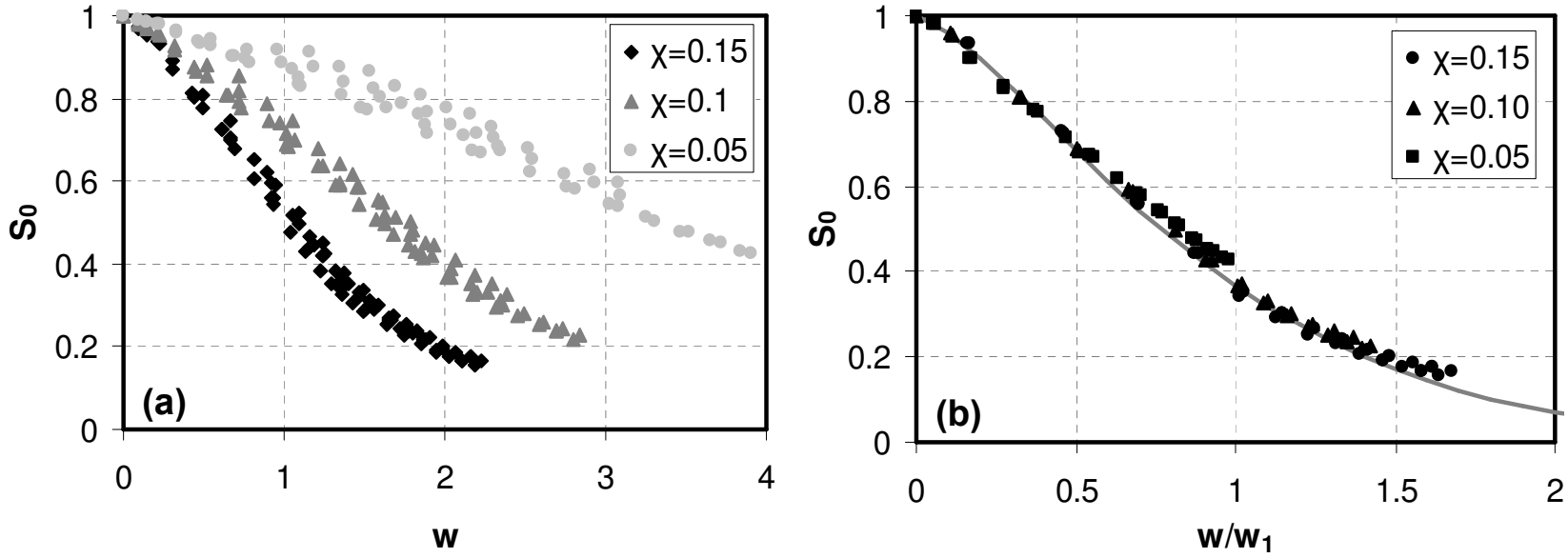

Figure 6.14 (a) Shear work correlation curves as a function of liquefaction resistance parameter (b) Shear work correlation curves after normalization with parameter w_1

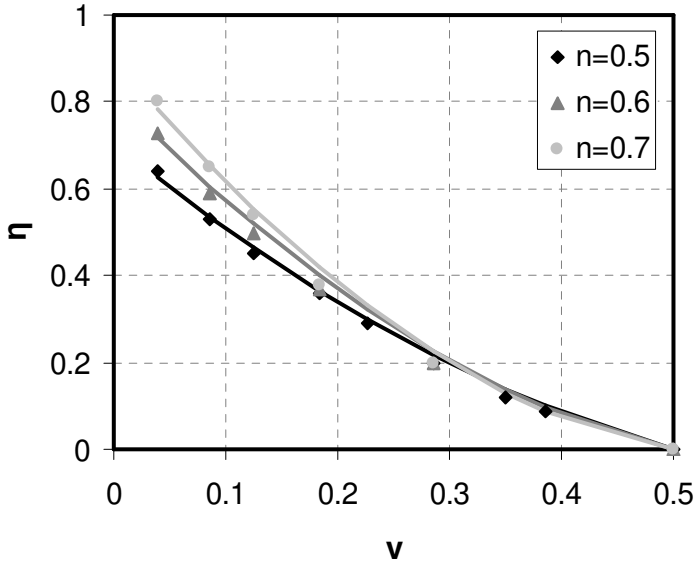

Figure 6.15 Parameter η as a function of Poisson's ratio and power exponent n

The curves depend only on the liquefaction resistance parameter for soil (χ) as shown in Figure 6.14(a), but by scaling the x-axis using the normalization parameter w_1, they follow the same backbone as shown in Figure 6.14(b). The scaling parameter w_1 is found to be inversely proportional to χ and is expressed as

$$w_1 = \eta / \chi \tag{6.5}$$

where η is a function of Poisson ratio of soil as shown in Figure 6.15 and is given as

$$\eta = n^{(1-n)}(1-2\nu)^{2n}(1-\nu)^{2(1-n)} \tag{6.6}$$

where 'n' is the power exponent for soil. A good match is obtained for fitting the curve shape of shear work correlation curves using a value of $\kappa = 1.4$.

Partially Drained Response

Drainage Parameter (β)

Figure 6.16 shows shear work correlation curves for partially drained case for different values of soil permeability. It can be seen that instead of degrading continuously as a function of shear work, the pile response achieves a steady state after some time. The steady state S_{oeq} is plotted as a function of permeability in Figure 6.19. While the dots represent the values obtained from FE simulations, the lines represent the values obtained from fit using the β parameter.

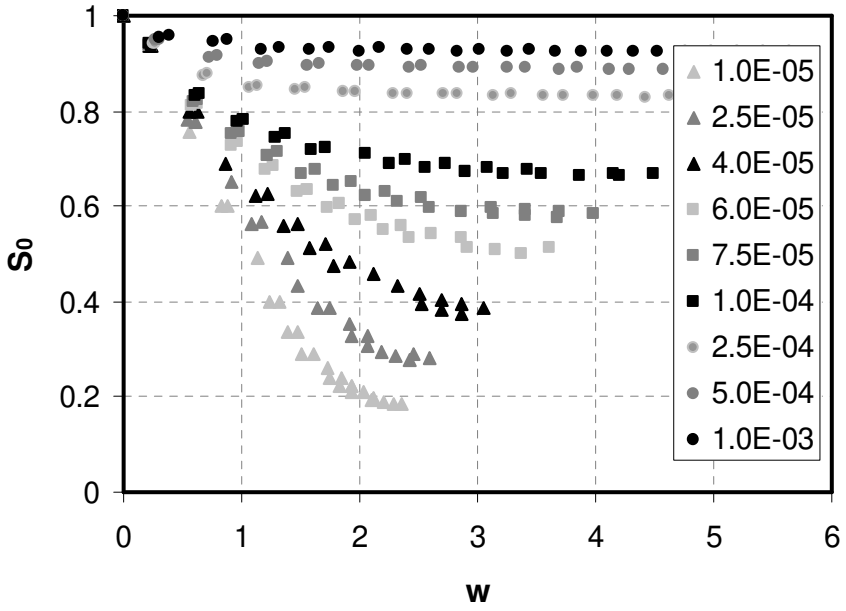

Figure 6.16 Shear work correlation curves for partially drained case for varying soil permeability

Figure 6.17(a)-(b) show the variation of response for different soil porosity and at different depths, respectively. The response is almost independent of porosity and also appears to be independent for depths greater than one diameter indicating that drainage is primarily radial in nature during liquefaction.

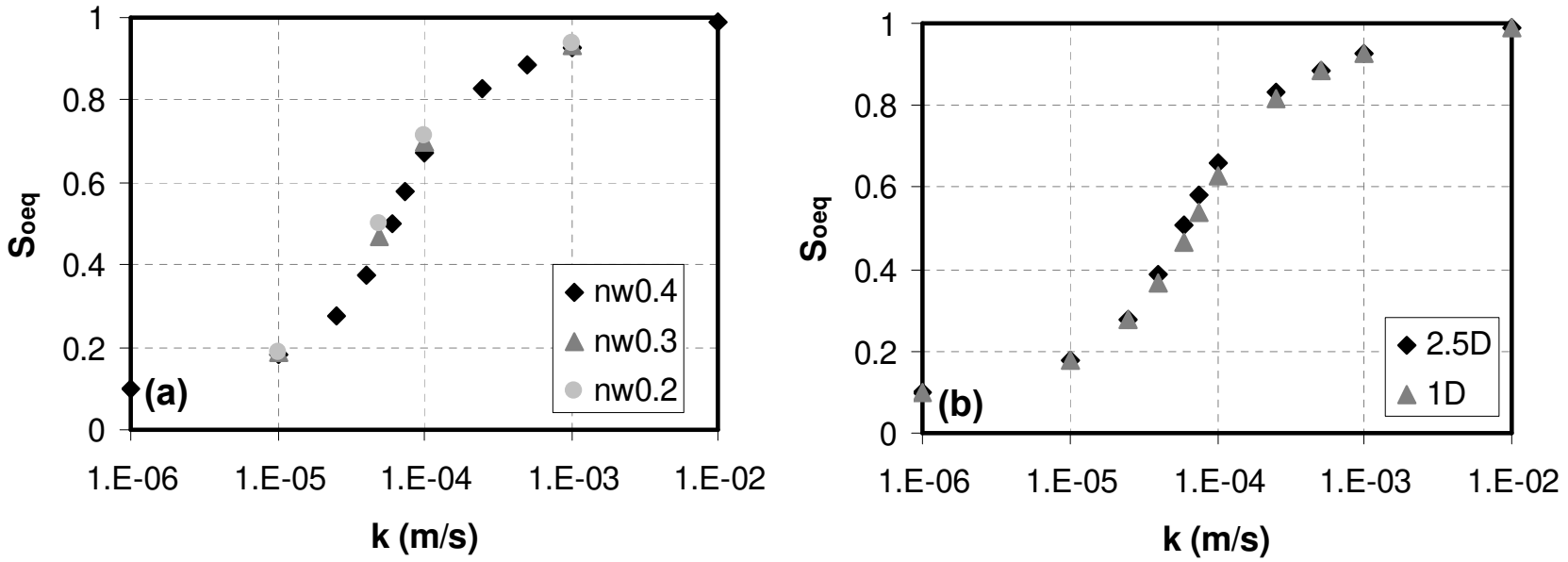

Figure 6.17 S_{oeq} (equilibrium) as a function of soil permeability for (a) soils with different porosity and (b) different depths below ground surface

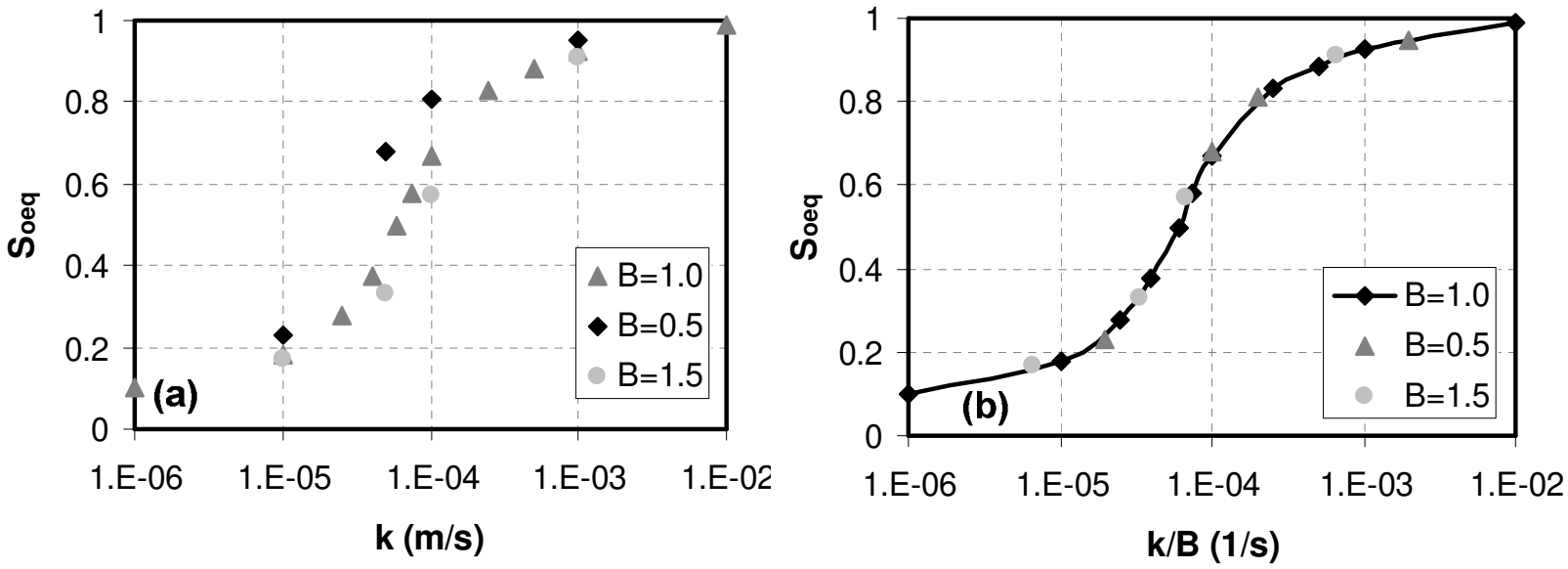

Figure 6.18 S_{oeq} for different pile diameter as a function of (a) soil permeability (b) soil permeability normalized with pile diameter

Figure 6.18(a) shows the response for different pile diameters. Since the near-field liquefied zone is proportional to pile diameter, the drainage length for larger piles is longer and hence the equilibrium average effective stress ratio decreases as pile diameter increases which agrees with the observations from FEM simulations. By normalizing permeability with pile diameter (k/B), similar response is obtained for all pile diameters as shown in Figure 6.18 (b). It should be noted that the effect of loading rate is automatically taken into account in the model by the 'dt' term and the actual dimensionless parameter controlling the response is $k.dt/B$ or k/Bf . Since the response is controlled by bulk modulus (K_s) as opposed to Young's modulus, a similar dependence of β on Poisson's ratio is observed. Nonetheless, the total response as shown in Figure 6.20 is the same for both Poisson's ratio considered, since change in the rate of pore pressure dissipation is cancelled out by the change in rate of pore pressure generation as discussed in previous section. The β parameter is obtained as:

$$\beta = 550\frac{2(1+\nu)}{3(1-2\nu)}\frac{k}{B} \tag{6.7}$$

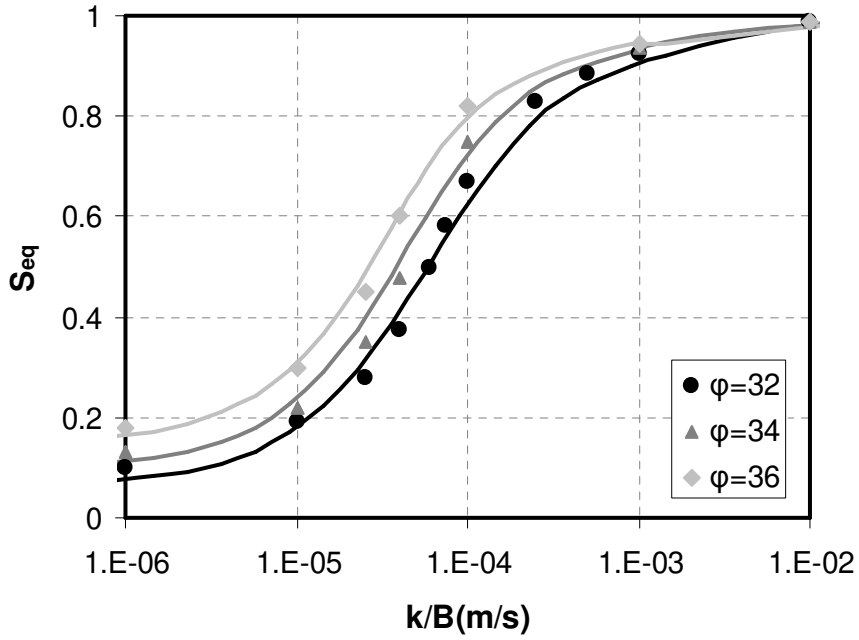

Figure 6.19 Comparison between observed (dots) and predicted (line) S_{oeq} values as a function of soil permeability and friction angle

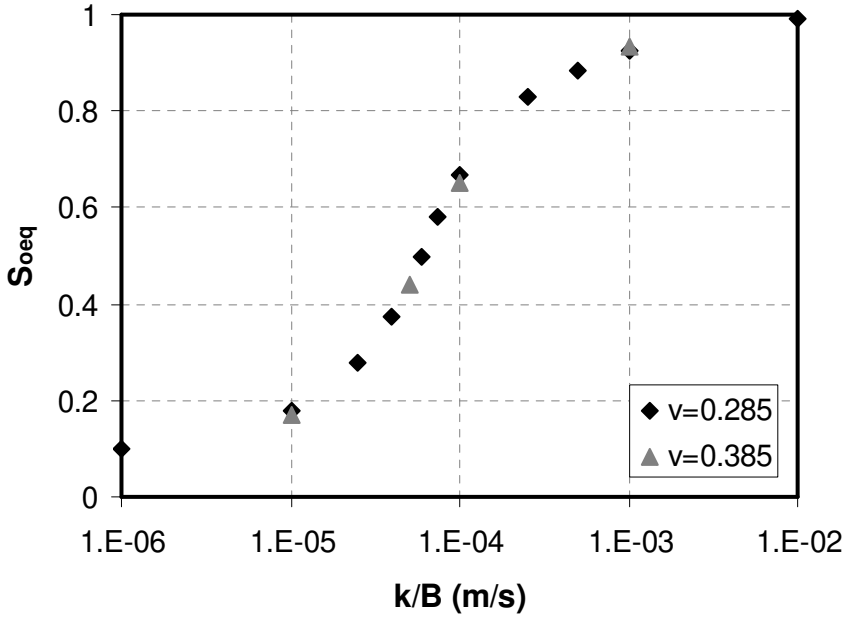

Figure 6.20 S_{oeq} vs. soil permeability variation for different values of Poisson's ratio

CHAPTER 7

VERIFICATION AND VALIDATION OF MACROELEMENT

3D Finite Element Comparison

In order to verify that the components of proposed model replicate the pile response observed during FEM simulations, sample predictions by the proposed model on the element scale are compared with the observed FEM response. In subsequent sections, we also compare the performance of the model to large-scale simulations of pile-supported waterfront structures and field test results. This work is currently under development and results so far are found to be in excellent agreement with observations.

Results presented here are for loose soil with $\varphi = 32^{\circ}$, $\varphi_{ss} = 30^{\circ}$ and $\chi = 0.15$. The comparison for dry/drained case is presented in Figure 7.1 (a)-(b) where (a) shows the predicted and observed response for cyclic loading with different displacement amplitude whereas (b) shows the force relaxation behavior when the pile is loaded monotonically and then subjected to unloading-loading in small loops. Figure 7.2 (a)-(b) shows the comparison for undrained behavior at two different loading amplitudes of 1 cm (almost no dilation) and 5 cm (significant dilation), respectively. Finally, the partially drained behavior for soil permeability ranging from $k=10^{-5}$ to $5x10^{-4}$ m/s is compared in Figure 7.3 (a)-(d). It can be seen that the model is able to simulate the pile response with sufficient degree of accuracy.

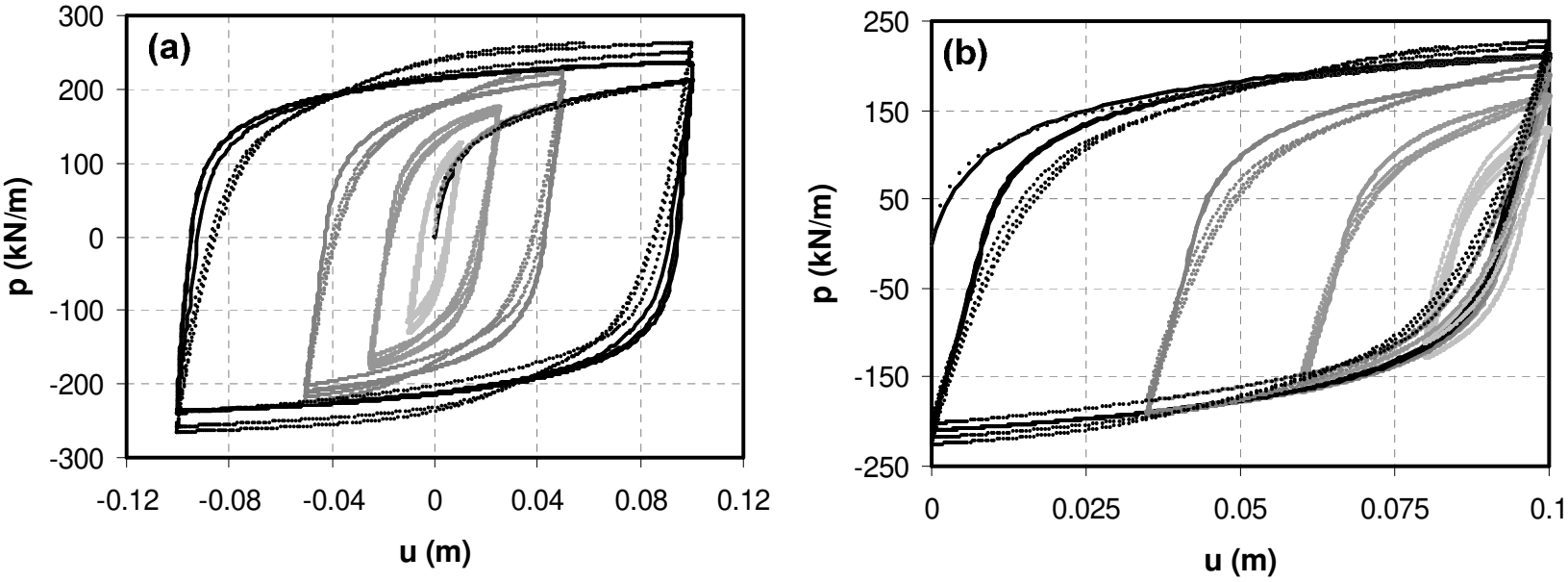

Figure 7.1 Comparison between predicted (solid) and observed (dotted) drained pile response for (a) different cyclic loading amplitudes (b) unloading-reloading in small loops

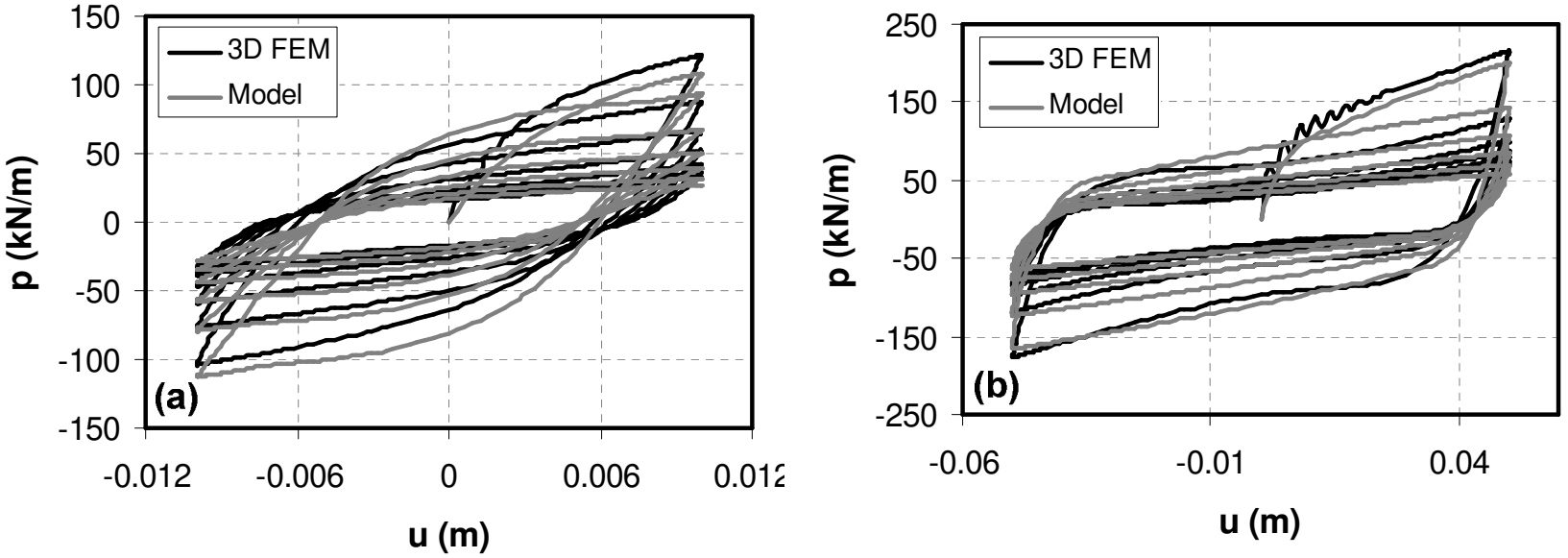

Figure 7.2 Comparison of observed (3D FEM) and predicted (model) response for loose soil (φ=32, χ=0.15) at 2m depth for two displacement amplitudes (a) 1 cm and (b) 5 cm.

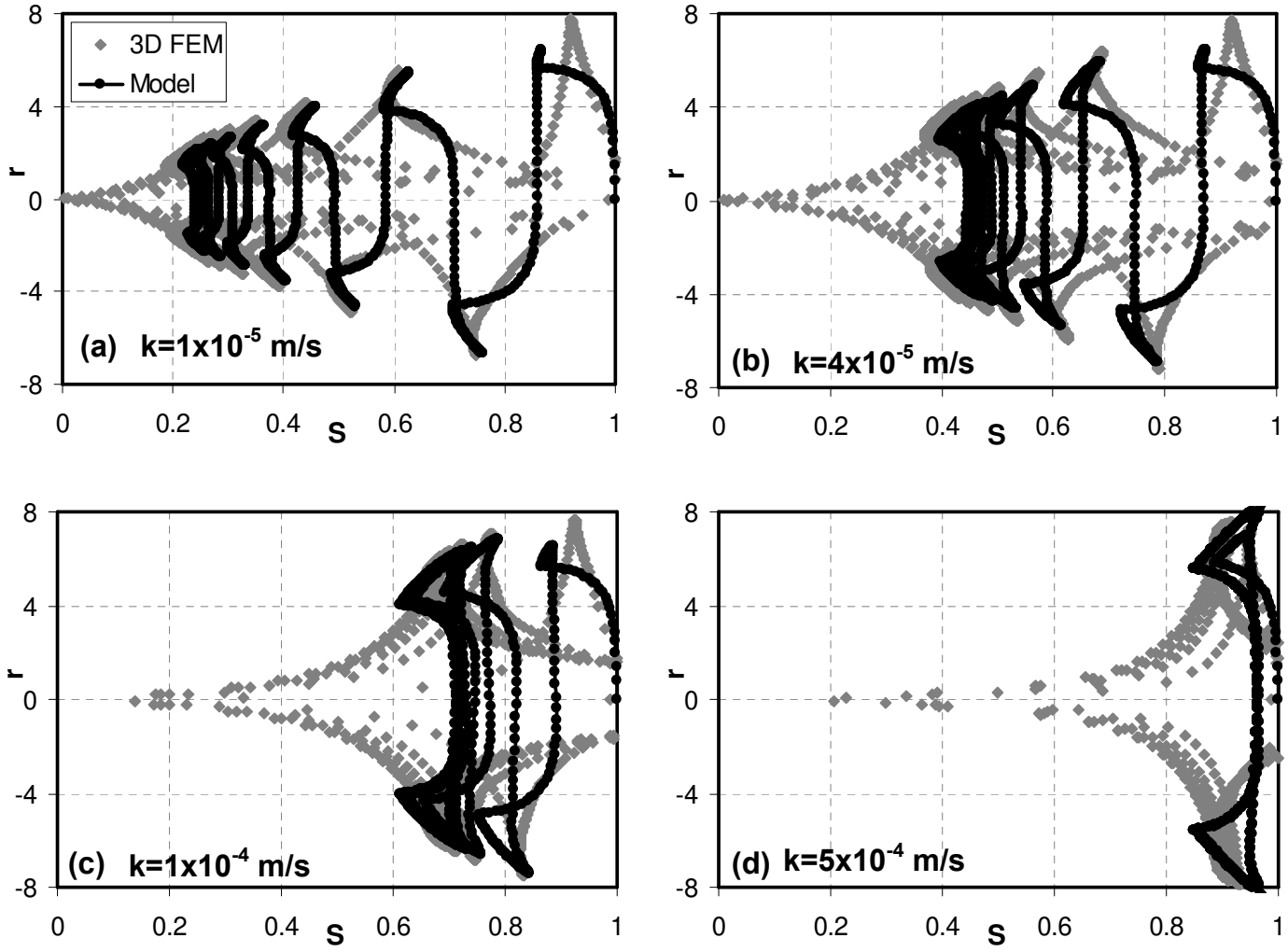

Figure 7.3 (a)-(d) Comparison of partially drained pile response in r-S domain for four different soil permeability

Validation

The performance of macroelement is validated next by comparison with two different kinds of tests. The first type consists of field tests where liquefaction is induced by means of controlled blasting followed by lateral loading of pile. The second type consists of centrifuge experiments where the pile with a superstructure is excited by means of seismic loading.

Comparison with Field Test using Blast Induced Liquefaction

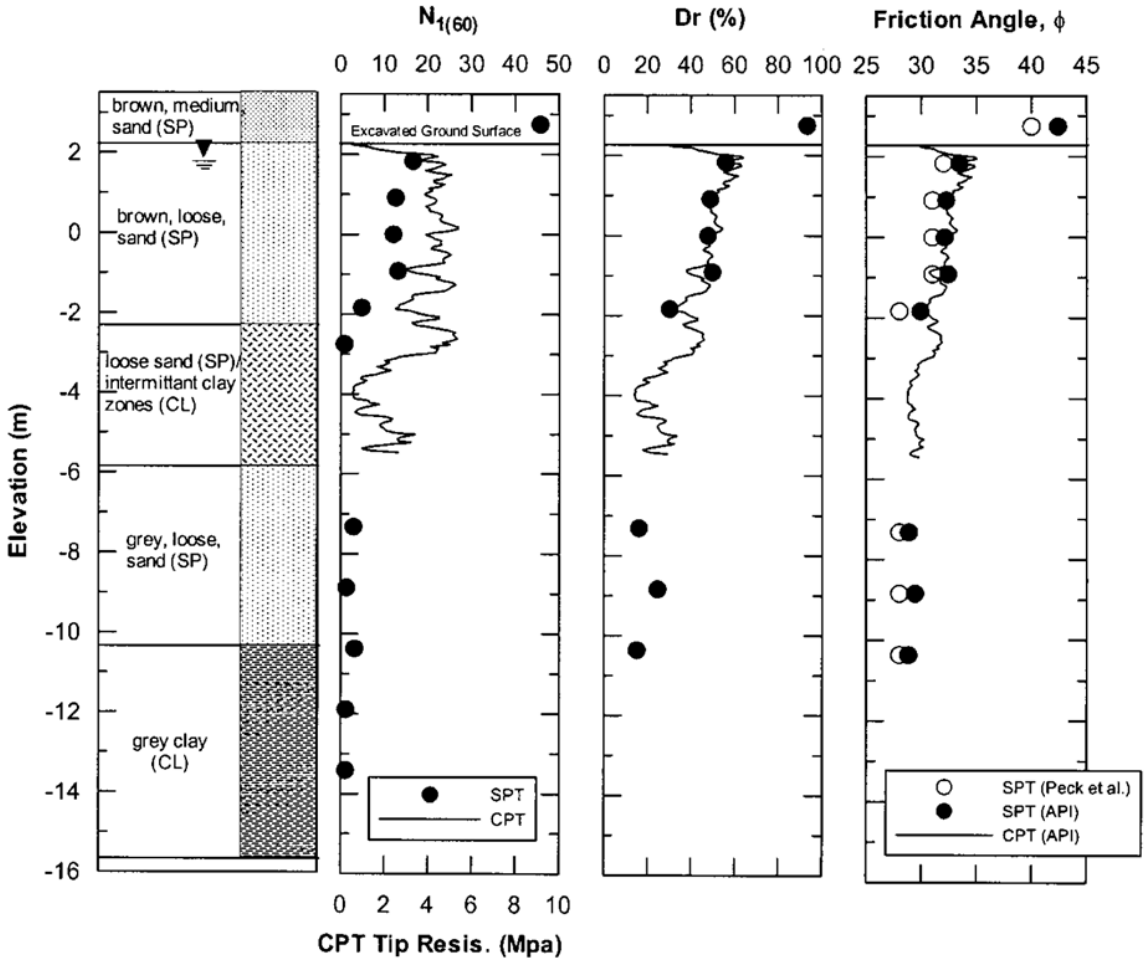

Figure 7.4 (a) Soil profile (b) SPT and CPT records (c) Estimated relative density (d) Estimated friction angles (Weaver et al. [63])

The field test was conducted at National Geotechnical Experimentation site at Treasure Island, California. The island was constructed during Golden Gate International Exposition in 1930s by hydraulic filling dredged material from Sacramento River over shoals of neighboring Yerba Buena Sand. The site conditions have been explored using subsurface investigations (Faris and de Alba [95]). The soil profile along with corrected blow counts (SPT), Cone Tip Resistance (CPT), Relative density (estimated from relationships proposed by Kulhawy and Mayne [96]), and friction angle (estimated from CPT, SPT and Peck et al. [97]) are shown in Figure 7.4. The reader is referred to Weaver et al. [63] for more details.

The soil parameters estimated from the field data are shown in Table 1. The critical state friction angle (φ_{ss}) is estimated using the relative density and friction angle (φ). For very loose sands (D_r = 20%, $\varphi - \varphi_{ss} = 1 - 2^{\circ}$) whereas for loose sands (D_r = 50%, $\varphi - \varphi_{ss} = 3^{\circ}$). The liquefaction resistance parameter is estimated from SPT blowcounts as recommended by Popescu and Prevost [78]. Finally the drainage parameter (β) is estimated directly from the dissipation rate of excess pore pressure right next to pile as shown in Figure 7.5. In t = 300 seconds, the excess pore pressure ratio drops from 0.85 (S = 0.15) to 0.61 (S = 0.39). Assuming the excess pore pressure ratio sufficiently far away from pile to be 1.0, we get

$$\frac{dS}{dt} = \beta . S^{n}(1-S) \tag{7.1}$$

Using, the above equation, the drainage parameter can be calculated as

$$\beta = \frac{1}{300}\int_{0.15}^{0.39} \frac{dS}{S^{n}(1-S)} \tag{7.2}$$

Integrating numerically we get, β = 0.0021 (1/s). Back calculating the soil permeability, we get k = 6.7×10^{-6} m/s which seems a reasonable value for medium to fine sands.

Using the soil parameters, the macroelement parameters were estimated using the relationships described in previous chapters and are shown in Table 2. The parameter S_{oi} is the initial value of effective stress ratio, i.e., $1-r_u$ in the near field just after blasting and is determined directly from the pore pressure histories.

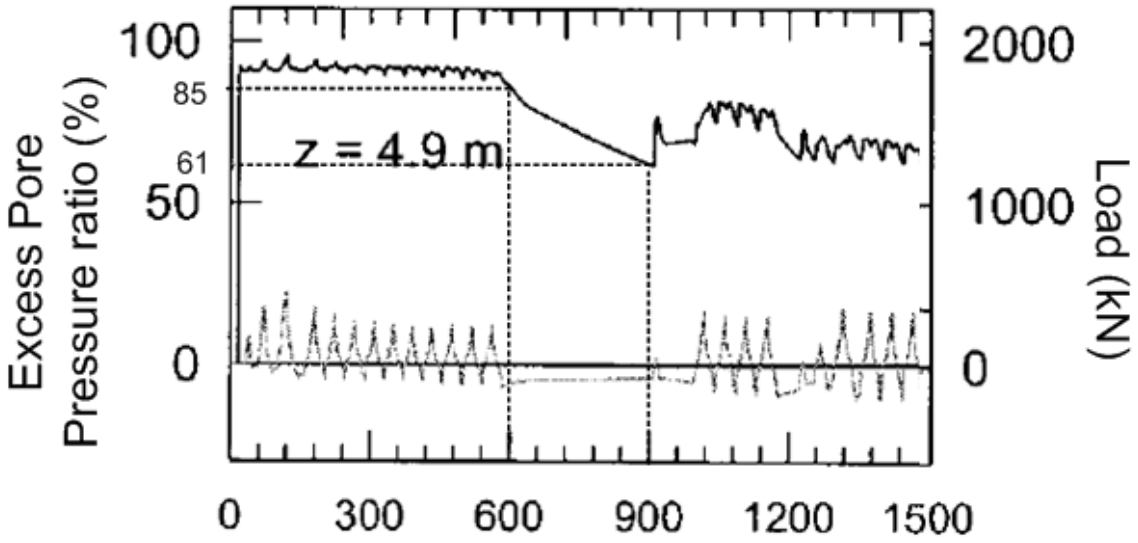

Figure 7.5 Calculation of drainage parameter from field test data (modified from Weaver et al. [63])

The pile has a diameter of 0.6 m and EI = 291,800 kN/m^2. After blasting, the loading was applied using a hydraulic actuator equipped with a swivel head to provide free head condition. Due to rapid dissipation of pore pressure, half loading cycles were used. The first series of loading consisted of one 75 mm, one 150 mm followed by eleven 225 mm displacement cycles at a rate of 10 mm/min. Due to slow loading rate, the radiation damping was considered to be negligible in the model.

Predictions vs Observations: No gap element

First, the field test is simulated using the macroelement without any gapping at soil-pile interface. The numerical model is shown in Figure 7.6. Figure 7.7 shows the comparison between observed and simulated results for force vs. displacement recorded at the top of pile whereas Figure 7.8 shows p-y curves recorded at different depths.

Table 7.1 Soil Properties estimated at the macroelement locations

Soil Type	Depth (m)	ρ (g/cc)	σ_v' (Pa)	φ	φ_{ss}	Xpp	k (m/s)
sand	0.185	1.90	3445	37	29	0.12	5.00E-06
sand	0.75	2.00	10611	33	29	0.14	5.00E-06
sand	1.5	2.00	17961	32	29	0.14	5.00E-06
sand	2.25	2.00	25311	32	29	0.14	5.00E-06
sand	3	2.00	32661	32	29	0.14	5.00E-06
sand	3.75	2.00	40011	32	29	0.14	6.70E-06
sand	4.5	2.00	47361	32	29	0.14	6.70E-06
clayey sand	5.3	2.00	55201	30	28	0.15	6.70E-06
clayey sand	6.3	2.00	65001	30	28	0.15	6.70E-06
clayey sand	7.3	2.00	74801	30	28	0.15	6.70E-06
clayey sand	8.3	2.00	84601	29	28	0.16	6.70E-06
sand	9.3	2.00	94401	29	28	0.18	6.70E-06
sand	10.3	2.00	104201	29	28	0.18	6.70E-06
sand	11.3	2.00	114001	29	28	0.18	6.70E-06
sand	12.3	2.00	123801	29	28	0.18	6.70E-06

Table 7.2 Macroelement parameters calculated from soil properties

S.No	D (m)	K (Pa)	P_y (kN.m)	α	m_1	m_2	w_1	S_{0i}	β (1/s)
1	0.38	16239915	37056	2.8	17.93	9.37	1.65	0.25	0.0016
2	0.75	24430840	92165	2.8	14.48	9.37	1.41	0.22	0.0016
3	0.75	31785271	148233	2.8	13.76	9.37	1.41	0.20	0.0016
4	0.75	37732492	208893	2.8	13.76	9.37	1.41	0.17	0.0016
5	0.75	42862320	269553	2.8	13.76	9.37	1.41	0.15	0.0016
6	0.75	47440657	330213	2.8	13.76	9.37	1.41	0.13	0.0016
7	0.75	51614469	390873	2.9	13.76	9.37	1.41	0.12	0.002
8	1.00	46435839	412351	2.9	12.45	9.00	1.32	0.10	0.002
9	1.00	50389479	485557	2.9	12.45	9.00	1.32	0.10	0.002
10	1.00	54054714	558763	2.9	12.45	9.00	1.32	0.10	0.002
11	1.00	57486734	601948	2.9	11.86	9.00	1.24	0.10	0.002
12	1.00	60725095	671677	2.9	11.86	9.00	1.10	1.00	0.002
13	1.00	63799292	741405	2.9	11.86	9.00	1.10	1.00	0.002
14	1.00	66732017	811133	2.9	11.86	9.00	1.10	1.00	0.002
15	1.00	69541172	880862	2.9	11.86	9.00	1.10	1.00	0.002

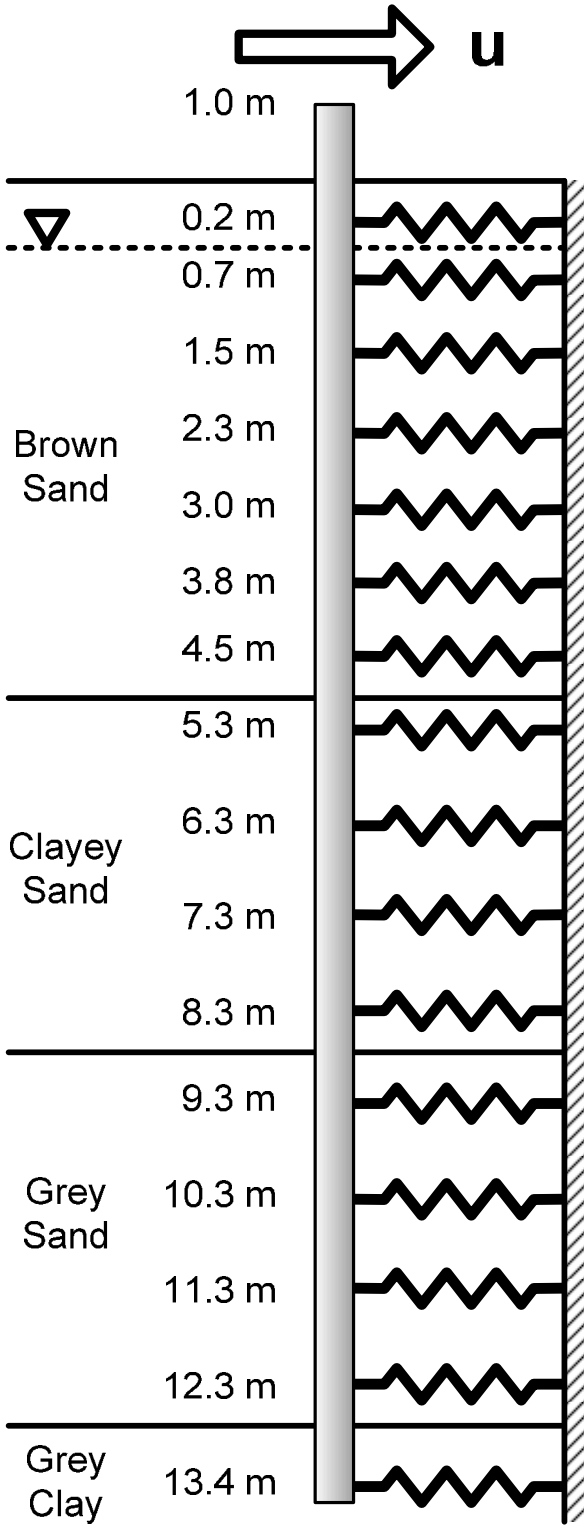

Figure 7.6 Numerical model used to simulate field test

It can be seen that while the magnitude of total force at maximum displacement is captured with reasonable accuracy, the strain hardening behavior exhibited by observed data is not seen in numerical results. Similar observations can be made with p-y response as well. While the authors reported no visible gap formation due to liquefied sand and water flowing behind the pile, the liquefied sand mixture that fills up the gap is expected to be show a softer response than the original soil present in the region.

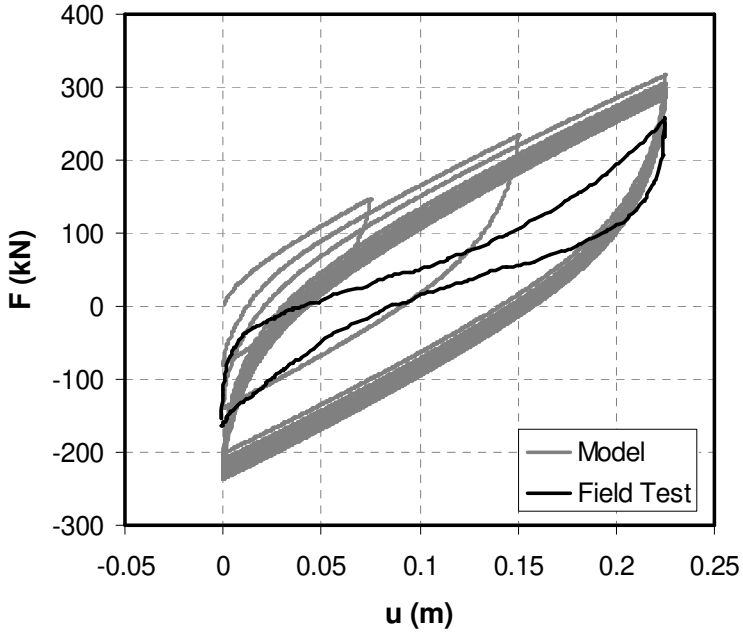

Figure 7.7 Lateral force vs. displacement response at the top of pile without accounting for gapping.

This can also be observed from Figure 7.9, where during first three cycles when the cyclic displacement amplitude is successively increased, the initial part shows a concave region with strain hardening, whereas after the previous maximum displacement is exceeded, the response is almost a straight line that looks more like the predicted response without a gap. The displacement profile shown in Figure 7.10 (b) and somewhat agrees with the observed displacements. Figure 7.10(a) shows the predicted and observed bending moments for last cycle when the load at top of pile is 44, 137 and 232 kN, respectively. The bending moments are generally overpredicted for loads 44 and 137 kN

and the maximum bending moment occurs closer to the ground surface which is expected since the soil resistance in top layers is overestimated when the gapping is not accounted for. However, the bending moments at 232 kN are reasonably well predicted.

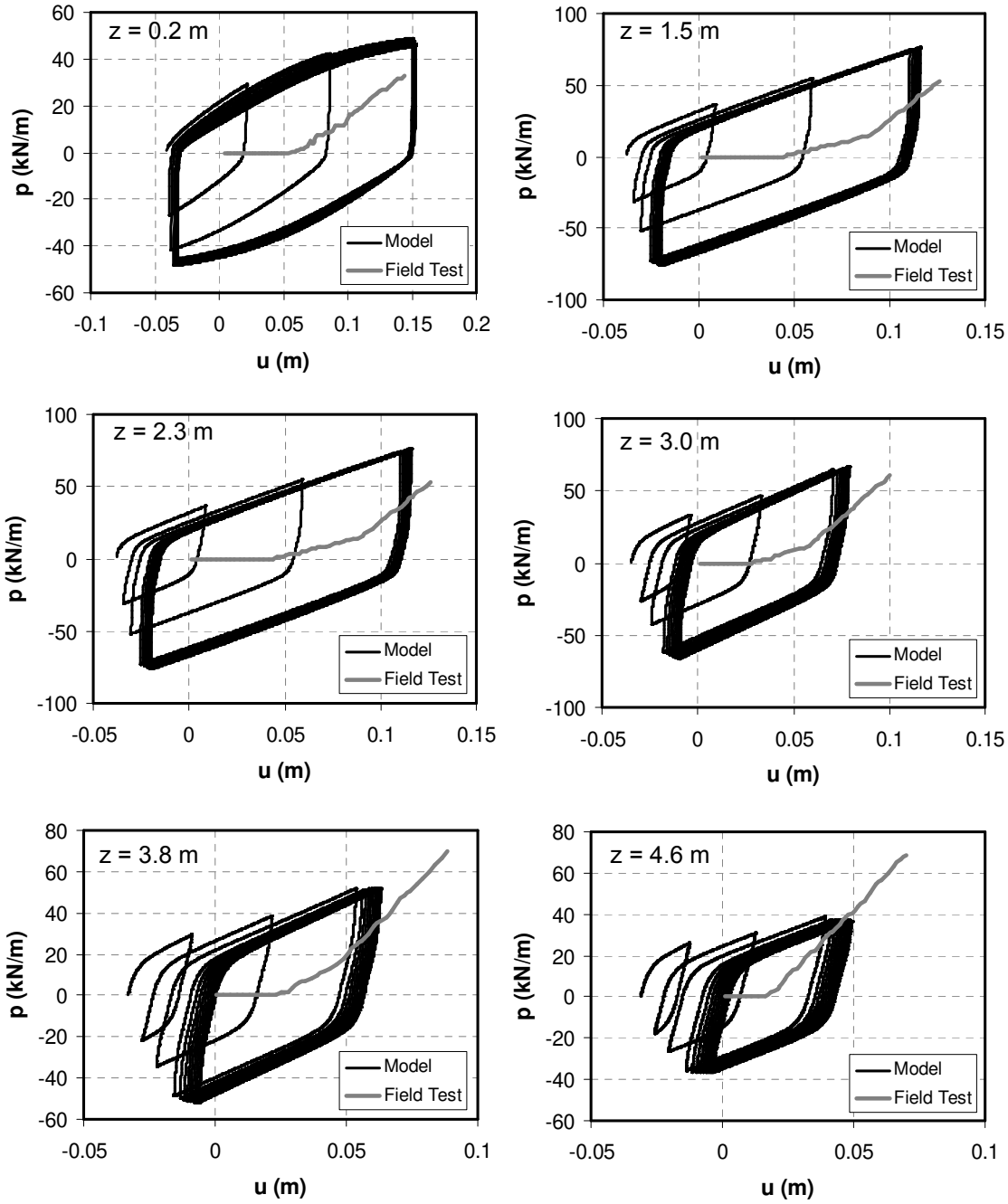

Figure 7.8 Comparison between p-y curves at different depths without accounting for gapping

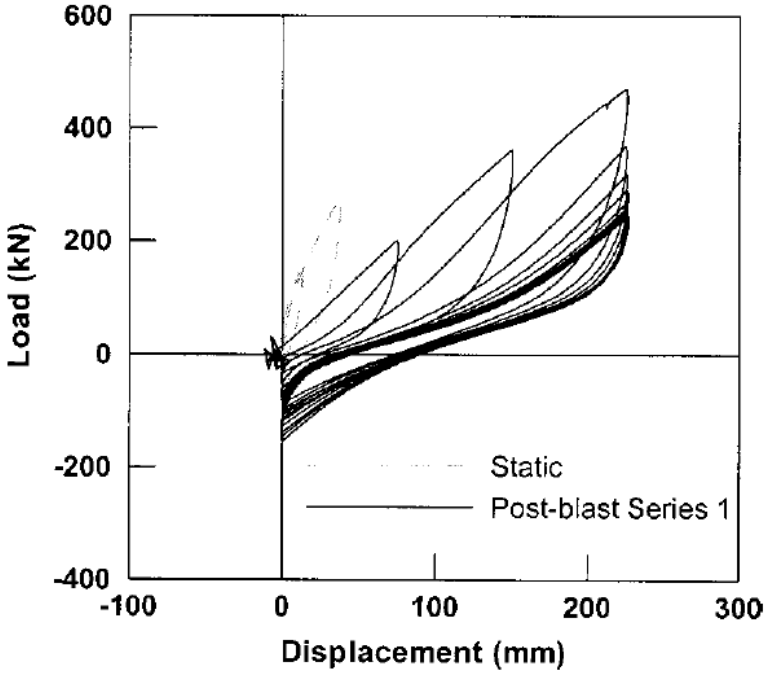

Figure 7.9 Lateral force vs. displacement response at the top of pile as observed in field test (Weaver et al. [63])

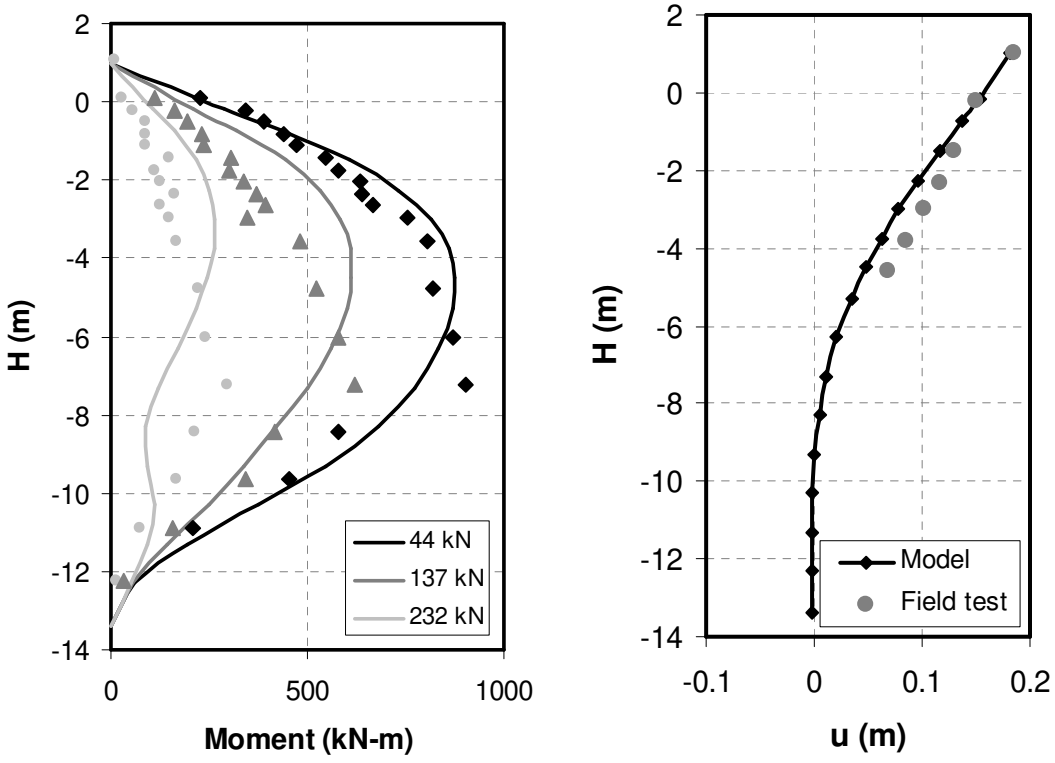

Figure 7.10 (a) Bending moment (b) Displacement profile with depth for simulation without soil-pile gapping

The Gap Element

In order to simulate the effect of gapping, a gap element is implemented as an additional component of the macroelement. The gap element is an envelope function used to scale the total p-y response predicted by the macroelement depending on the current displacement and the maximum previous displacement on each side of the pile. A hyperbolic function is used and the gap multiplier is calculated as

$$m_g = c_d + (1 - c_d)\frac{u_{ref}^{n_g}}{u_{ref}^{n_g} + \left|u - u_{\max}\right|^{n_g}} \quad (7.3)$$

Where c_d is the ratio of drag resistance from sides to total resistance and is typically equal to 0.1-0.2 (reference), $u_{\max}$ is the maximum previous displacement on each side, n_g is a power coefficient and u_{ref} is a reference displacement value used for scaling. The reference displacement is chosen as $u_{ref} = 5u_y$ where $u_y = p_y / K$ is the yield displacement and u_{ref} roughly corresponds to the displacement at which 50% of maximum resistance is mobilized. Figure 7.11 shows the variation of gap multiplier for power coefficient n_g = 1, 2 and 4. A power coefficient of 2 is used in this study.

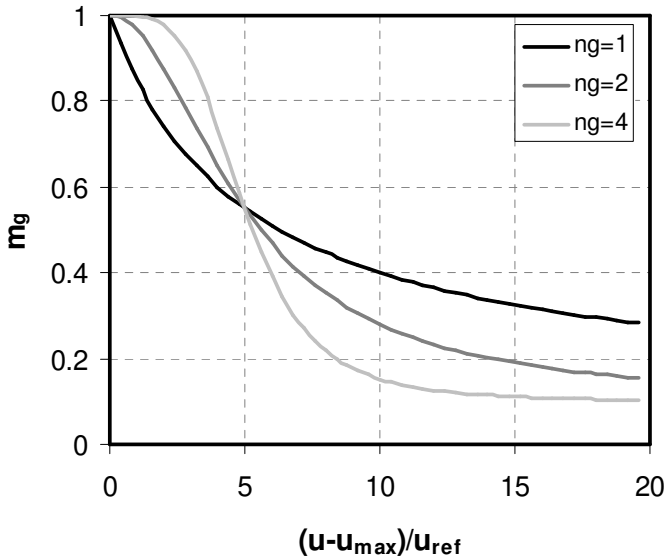

Figure 7.11 Variation of gap multiplier for different power coefficients

Predictions vs Observations: Gap element

Figure 7.12 shows the total force recorded at pile head vs. displacement. Very good agreement is obtained between the observed and predicted values. The agreement between p-y curves recorded at six different depths is also quite good as can be seen in Figure 7.13. Good agreements between displacement and bending moment are also observed as shown in Figure 7.14 (a) and (b), respectively.

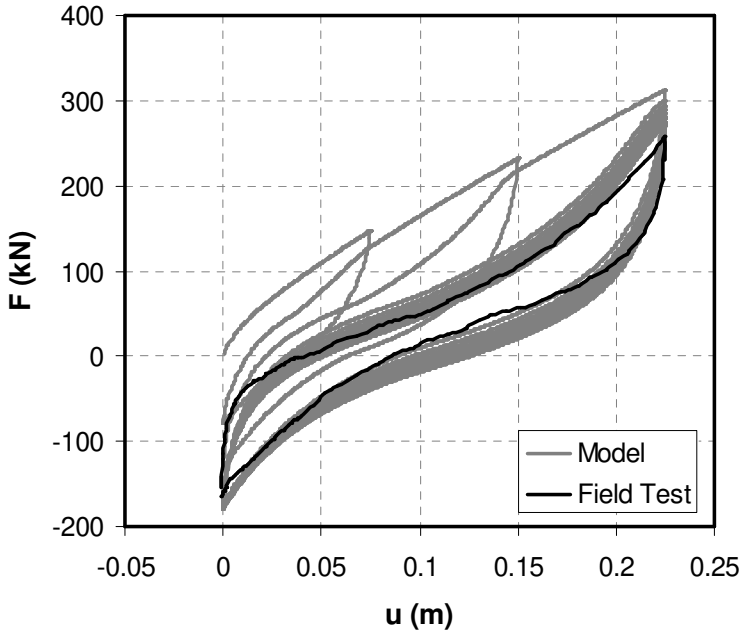

Figure 7.12 Comparison between observed and predicted lateral force at pile top when accounting for soil-pile gapping

Comparison with Pysimple1

To compare with other available formulations, the p-y simple element (Boulanger et al. [47]) was also used to predict the pile response. The element properties were generated using the in-built pysimplegen1 module in OPENSEES [98] using the soil properties provided in Table 1. A drag coefficient of 0.3 and residual strength ratio of 0.1 were used. The ultimate resistance in the module is calculated using the API [17] method. In order to provide a fair comparison, the response of macroelement proposed in this study (henceforth referred to as PYmacro) was also computed using the same p-y

resistance. The parameters used for PYmacro are presented in Table 3. Figure 7.15 presents the total lateral force vs. displacement response for pysimple1 and PYmacro, respectively. It can be seen that the response predicted by PYmacro is still reasonably good and better than the response predicted by pysimple1.

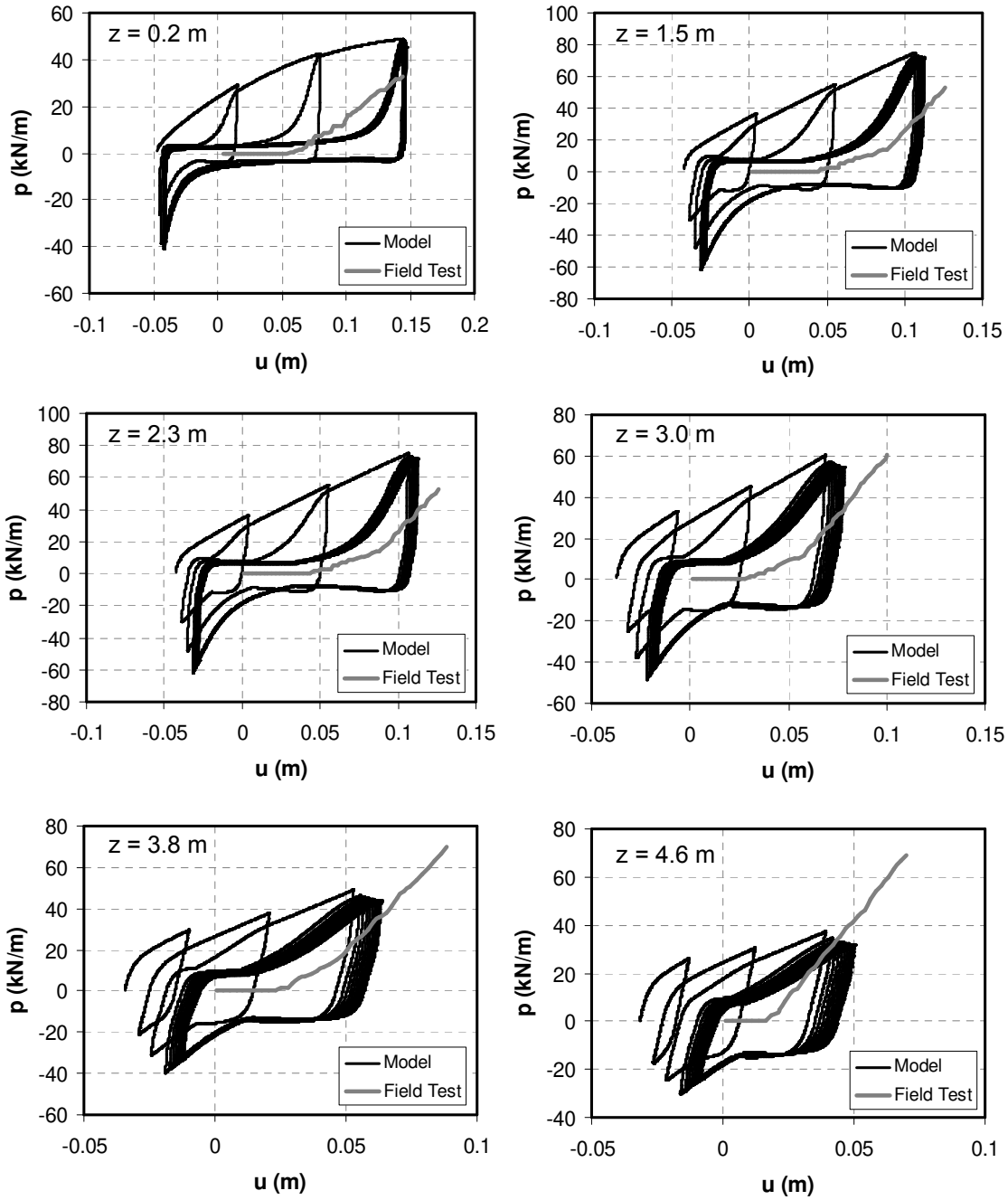

Figure 7.13 p-y curves at six depths with soil-pile gapping

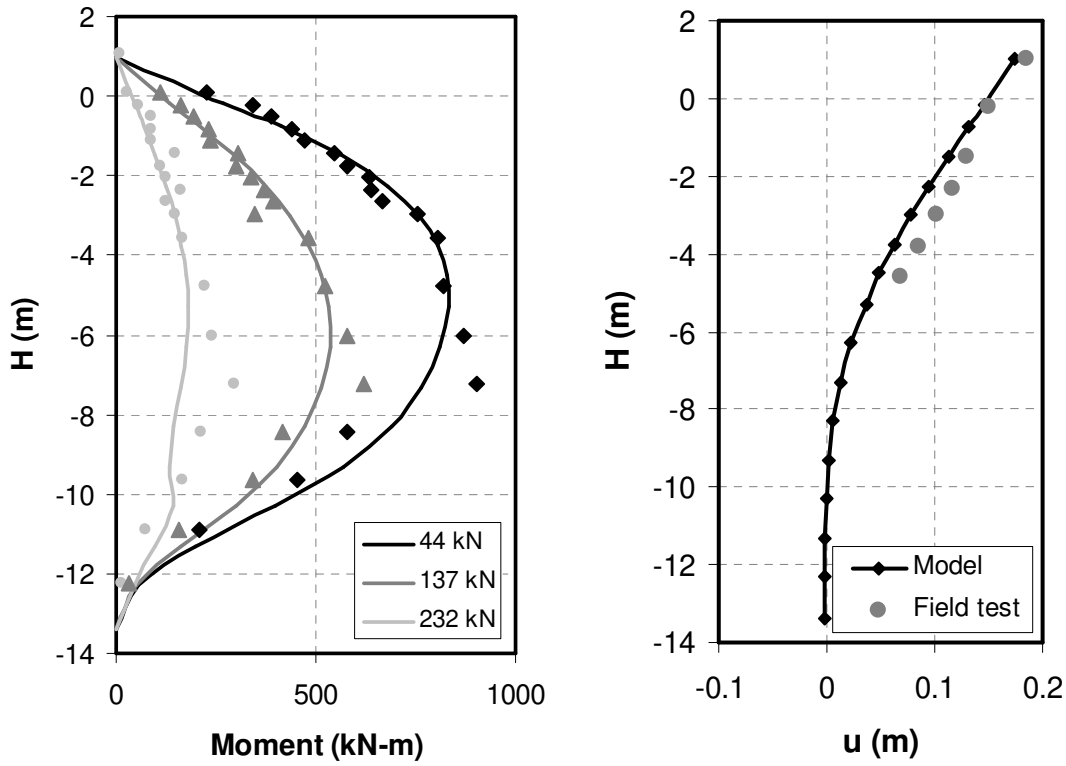

Figure 7.14 (a) Bending moment (b) Displacement profile with depth for simulation with soil-pile gapping

Table 7.3 Macroelement parameters with p_y calculated using API [17] method

S.No	D (m)	K (Pa)	P_y (kN.m)	α	m_1	m_2	w_1	S_{0i}	β (1/s)
1	0.38	16239915	23496	2.8	11.37	5.94	1.65	0.25	0.0016
2	0.75	24430840	45821	2.8	7.20	4.66	1.41	0.22	0.0016
3	0.75	31785271	72867	2.8	6.76	4.60	1.41	0.20	0.0016
4	0.75	37732492	99568	2.8	6.56	4.46	1.41	0.17	0.0016
5	0.75	42862320	132046	2.8	6.74	4.59	1.41	0.15	0.0016
6	0.75	47440657	174580	2.8	7.27	4.95	1.41	0.13	0.0016
7	0.75	51614469	244439	2.9	8.60	5.86	1.41	0.12	0.002
8	1.00	46435839	354994	2.9	10.72	7.75	1.32	0.10	0.002
9	1.00	50389479	505595	2.9	12.96	9.37	1.32	0.10	0.002
10	1.00	54054714	633879	2.9	14.12	10.21	1.32	0.10	0.002
11	1.00	57486734	1131235	2.9	22.29	16.92	1.24	0.10	0.002
12	1.00	60725095	951105	2.9	16.79	12.75	1.10	1.00	0.002
13	1.00	63799292	1334370	2.9	21.34	16.20	1.10	1.00	0.002
14	1.00	66732017	1486940	2.9	21.74	16.50	1.10	1.00	0.002
15	1.00	69541172	1582618	2.9	21.31	16.17	1.10	1.00	0.002

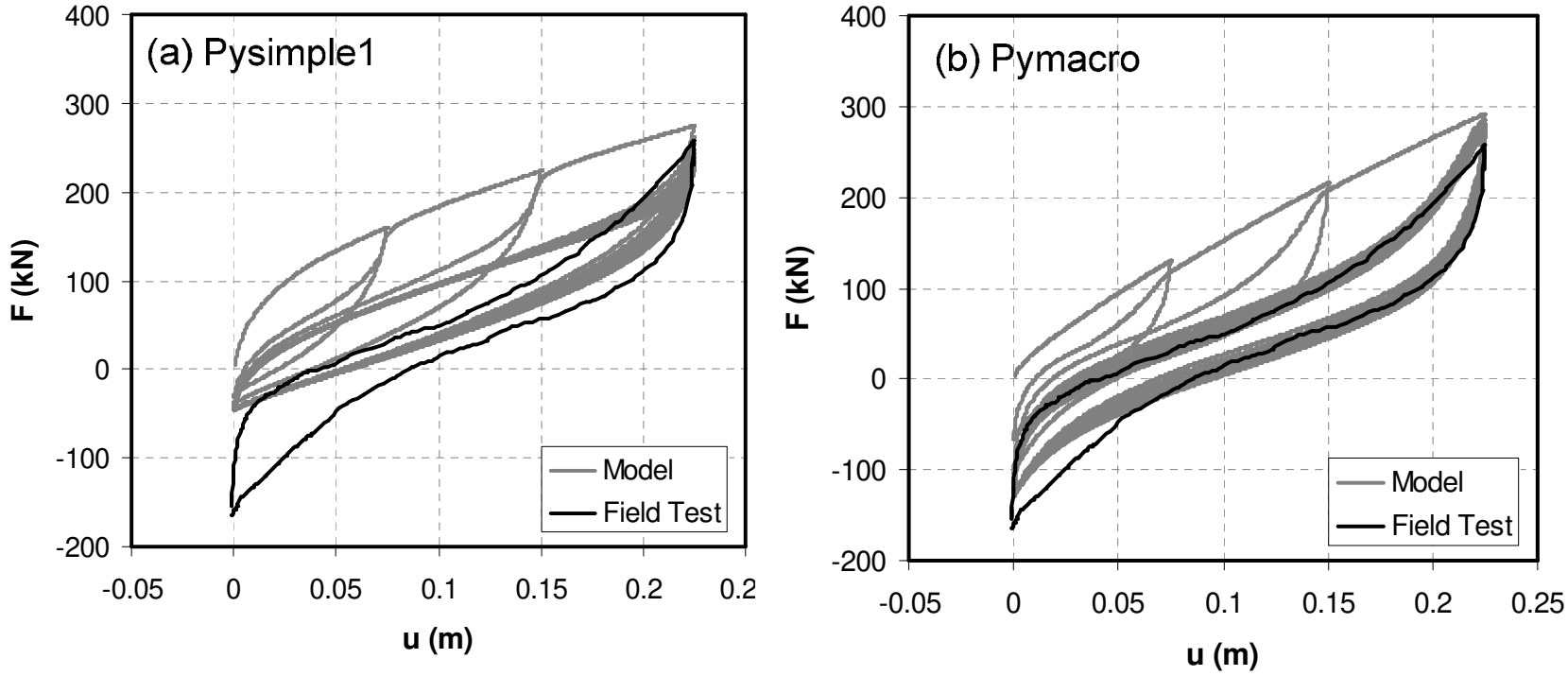

Figure 7.15 Comparison between observed and predicted lateral force at pile top for (a) Pysimple1 and (b) Pymacro

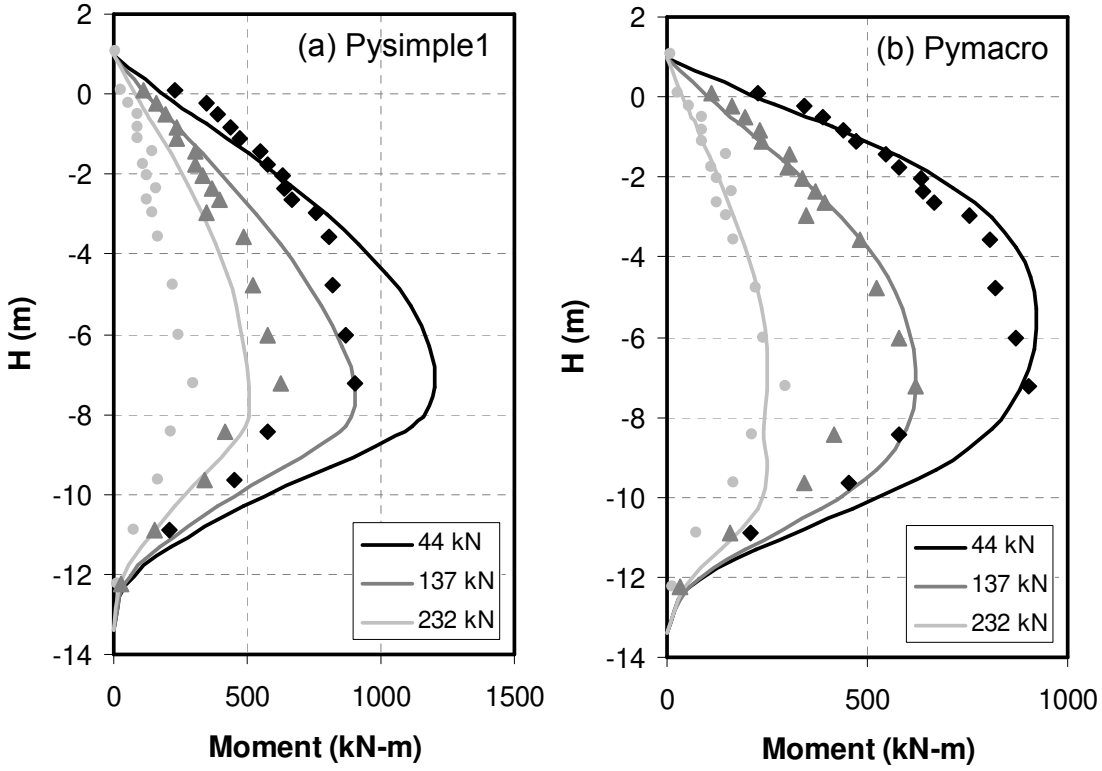

Figure 7.16 Bending Moment profiles for (a) Pysimple1 and (b) Pymacro

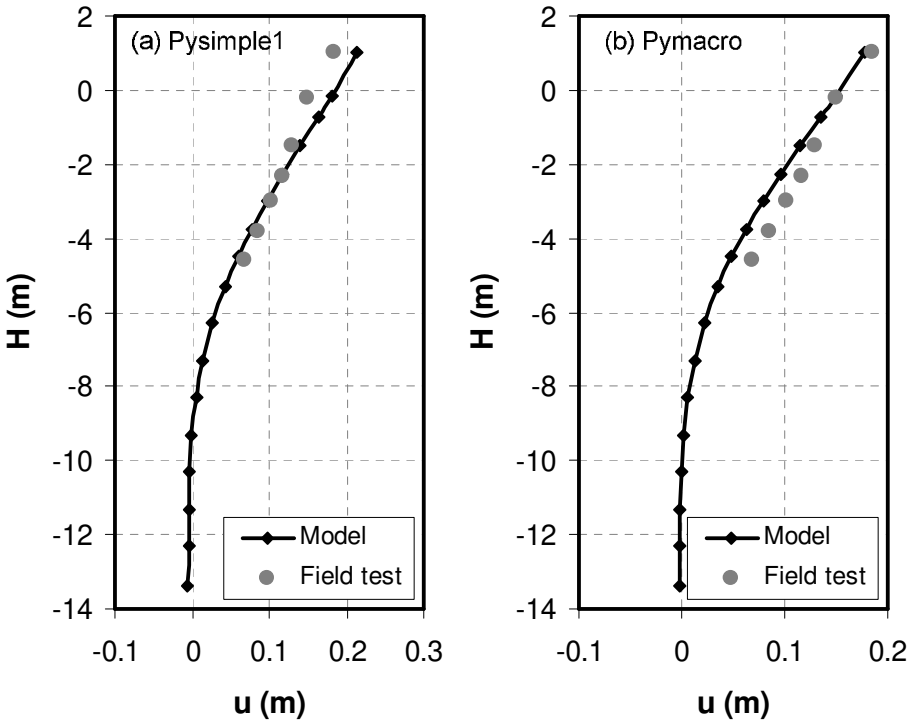

Figure 7.17 Displacement profiles for (a) Pysimple1 and (b) Pymacro

Similar observations can be made for the moment profiles as shown in Figure 7.16 where pysimple1 tends to overpredict the moments by around 50-70%. Good agreements for displacement profile are obtained for both the cases as shown in Figure 7.17.

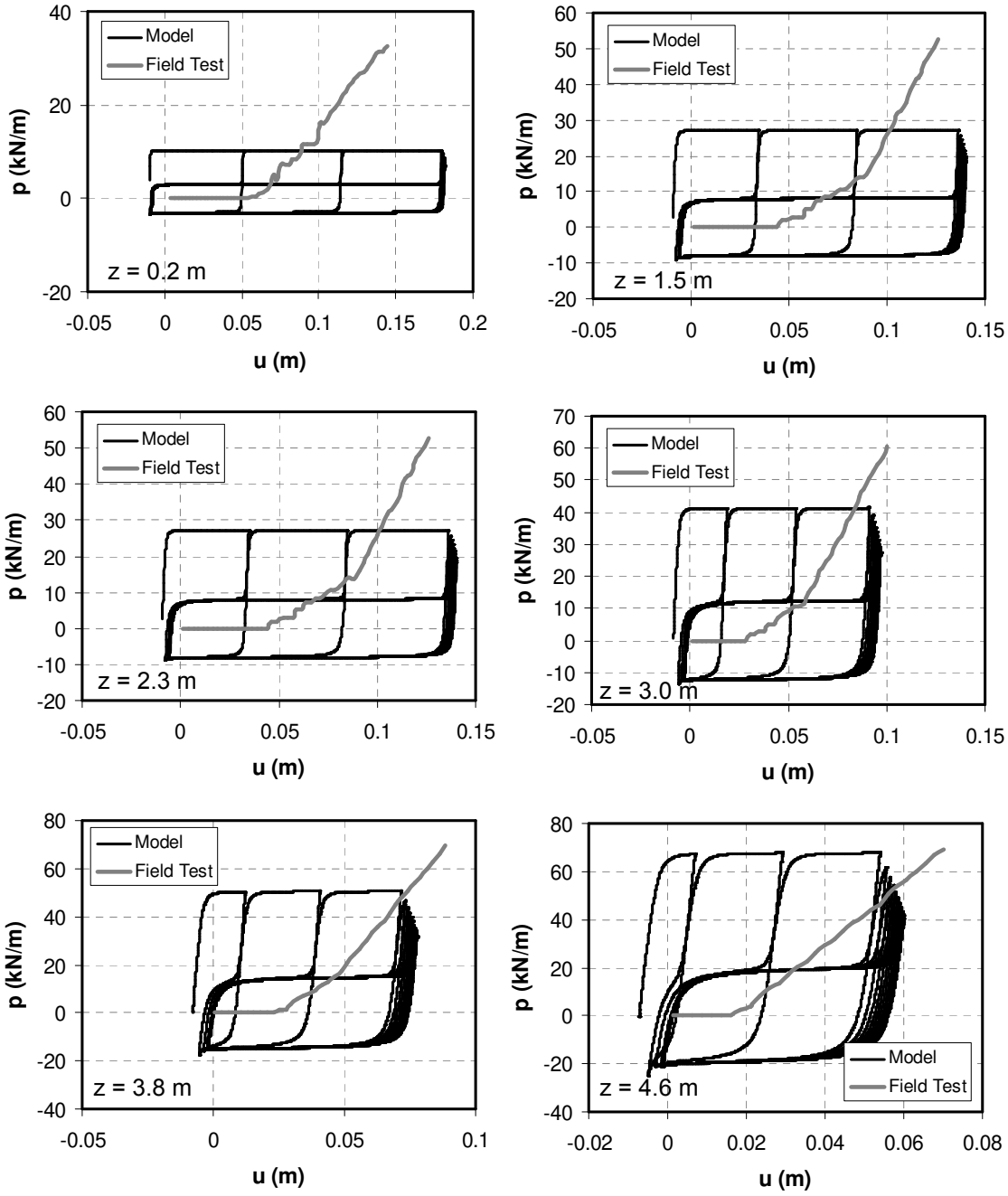

Figure 7.18 p-y response for pysimple1 method

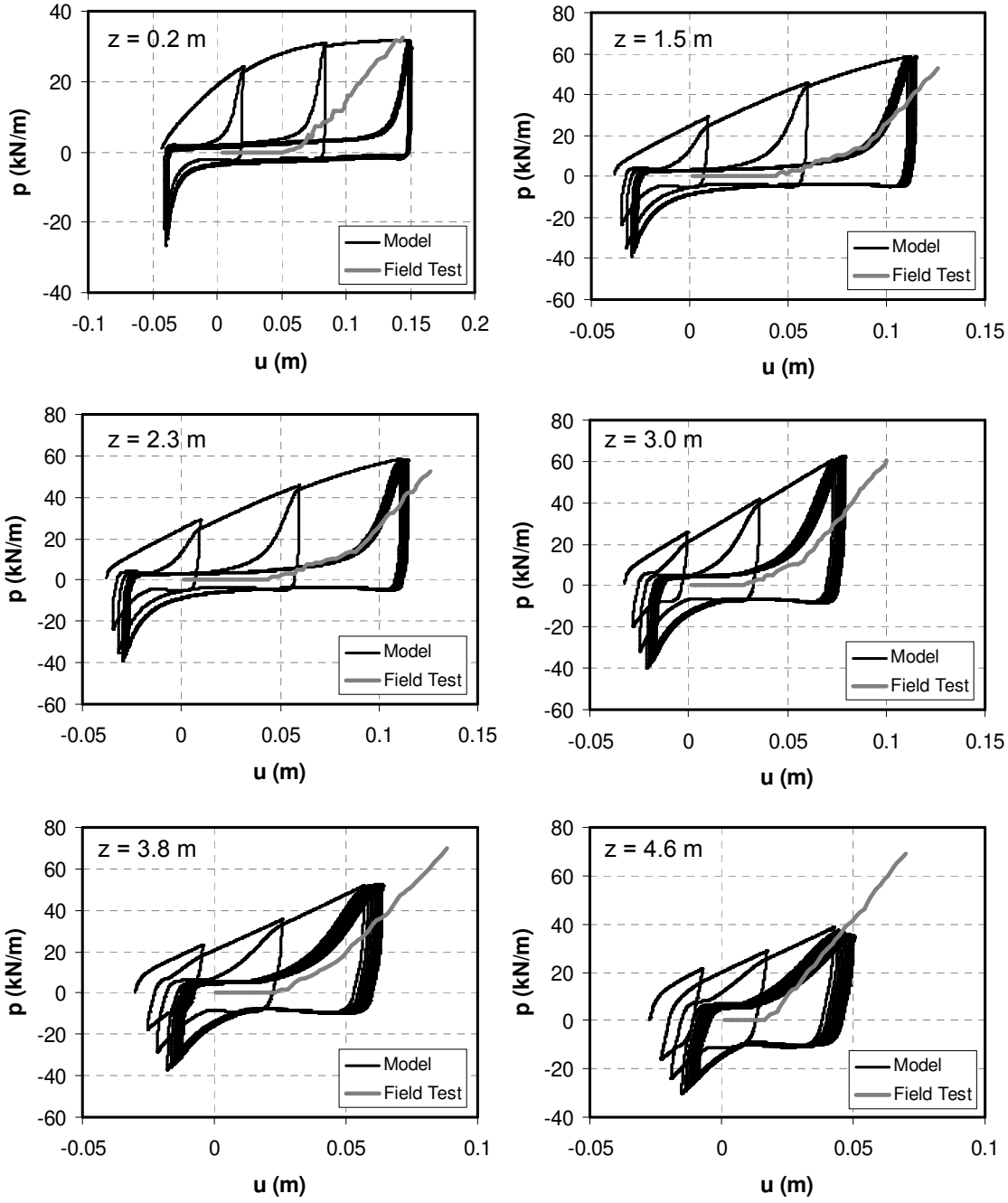

Figure 7.19 p-y response for PYmacro method

Finally, the p-y response for pysimple1 and pymacro are shown in Figure 7.18 and Figure 7.19, respectively.

Comparison with Centrifuge Tests

The centrifuge tests were conducted at National Geotechnical Centrifuge at UC Davis. An acceleration of 30g was used which gives a scaling factor of 30. A mixture of water and methyl cellulose with a viscosity 10 times that of water was used as the pore fluid. Two particular configurations referred to as CSP_2 and CSP_3 are chosen for simulation. The model layouts are shown in Figure 7.20 and Figure 7.21 respectively. CSP_2 consists of 9 m thick layer loose Nevada sand on the top (D_r = 35-40%) underlain by Dense Nevada sand (D_r = 80%) whereas the upper layer in CSP_3 is medium dense Nevada sand (D_r = 55%). Nevada Sand is fine, uniform sand (C_u =1.5, D_{50} = 0.15 mm) and its behavior has been extensively studied in both laboratory and centrifuge tests during the VELACS project (Arulanandan and Scott [99]). Hence the soil properties are reasonably well documented (Popescu and Prevost [78]).

The soil properties are shown in Table 4. Using the soil properties, the macroelement properties are calculated as given in Table 5 for CSP_2 and Table 6 for CSP_3. Both the models are subjected to two events A and B that are scaled versions Kobe 1995 earthquake. Event A has a maximum acceleration of 0.04 g whereas event B has a maximum acceleration of 0.22g.

Table 4 Soil Properties for Centrifuge Tests

Property	Unit	Dr = 35%	Dr = 55%	Dr = 80%
Shear Modulus (Go)	MPa	25	30	40
Bulk Modulus (Ko)	MPa	50	55	100
Power Exponent (n)	--	0.7	0.7	0.7
Friction angle (φ)	Degrees	32	34	38
CS Friction angle (φ_{ss})	Degrees	30	30	30
Liquefaction (χ)	--	0.16	0.14	0.06
Permeability (k)	m/s	$6.6x10^{-5}$	$5.6x10^{-5}$	$4.7x10^{-5}$

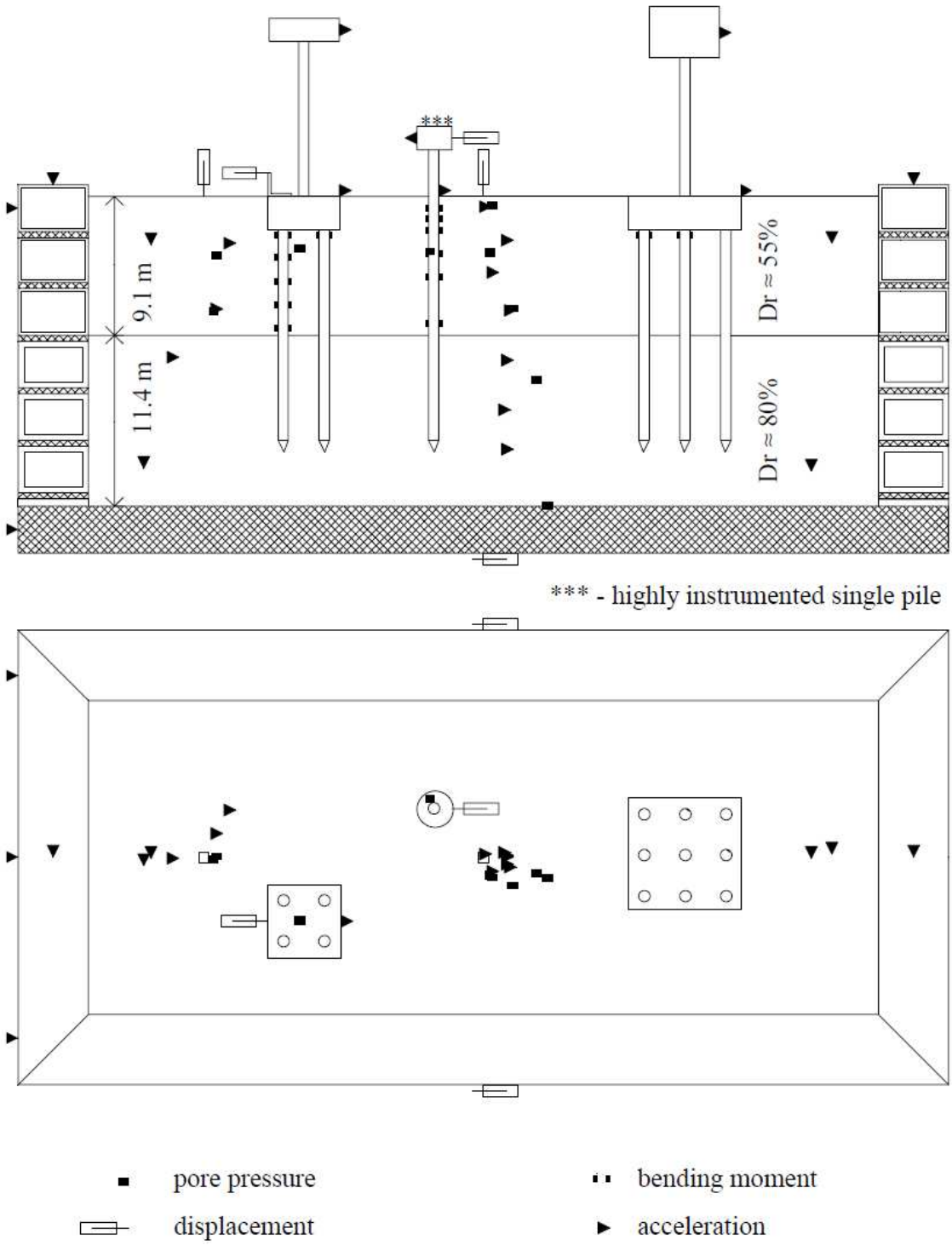

Figure 7.20 Model layout in CSP_2 (Wilson et al. [58])

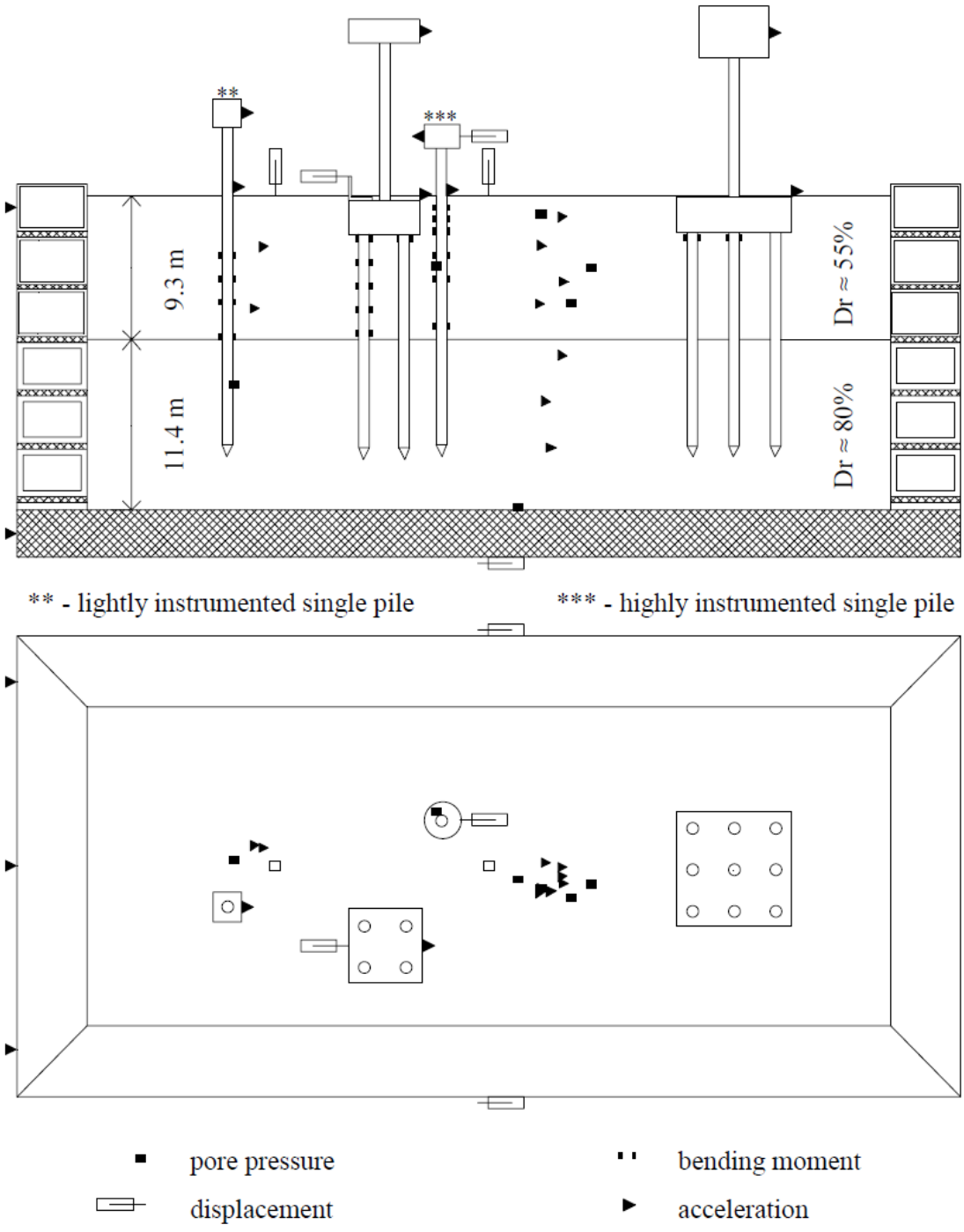

Figure 7.21 Model Layout in CSP_3 (Wilson et al. [58])

For the purpose of comparison, the highly instrumented pile was used for both models. The pile had a Young's modulus (E_p) = 70 GPa and Area moment of Intertia (I) = 0.0061 m^4. The superstructure mass (M_{ss}) was 49140 kg. The input displacement

histories for free-field end of macroelement were obtained by integrating the acceleration time histories recorded in free field in the centrifuge at seven locations and using linear interpolation for the other seven. The excess pore pressure ratio time histories were also obtained from pore pressure transducers in centrifuge experiments themselves. The numerical model is shown in Figure 7.22.

Table 5 Macroelement properties for Model CSP_2

No.	D (m)	K (Pa)	Py (kN/m)	α	m_1	m_2	w_1	B (1/s)	C_r (Pa.s)
1	0.335	1.56E+03	4.41E+06	2.9	13.76	9.75	1.257	0.12	1.38E+05
2	0.67	6.24E+03	1.17E+07	2.9	13.76	9.75	1.257	0.12	2.52E+05
3	0.67	1.25E+04	1.89E+07	2.9	13.76	9.75	1.257	0.12	3.42E+05
4	0.67	1.87E+04	2.51E+07	2.9	13.76	9.75	1.257	0.12	4.08E+05
5	0.67	2.50E+04	3.07E+07	2.9	13.76	9.75	1.257	0.12	4.63E+05
6	1	3.26E+04	3.71E+07	2.9	13.76	9.75	1.257	0.12	5.20E+05
7	1	4.19E+04	4.42E+07	2.9	13.76	9.75	1.257	0.12	5.81E+05
8	1	5.12E+04	5.09E+07	2.9	13.76	9.75	1.257	0.12	6.34E+05
9	1.5	6.28E+04	5.87E+07	2.9	13.76	9.75	1.257	0.12	6.94E+05
10	1.5	7.68E+04	6.75E+07	2.9	13.76	9.75	1.257	0.12	7.57E+05
11	2	9.39E+04	1.26E+08	2.7	18.96	9.75	3.352	0.08	1.13E+06
12	2	1.14E+05	1.44E+08	2.7	18.96	9.75	3.352	0.08	1.23E+06
13	2	1.34E+05	1.61E+08	2.7	18.96	9.75	3.352	0.08	1.32E+06
14	2	1.54E+05	1.78E+08	2.7	18.96	9.75	3.352	0.08	1.41E+06

Table 6 Macroelement properties for Model CSP_3

No.	D (m)	K (Pa)	Py (kN/m)	α	m_1	m_2	w_1	B (1/s)	C_r (Pa.s)
1	0.335	1.66E+03	4.97E+06	2.8	15.25	9.75	1.490	0.10	1.49E+05
2	0.67	6.65E+03	1.31E+07	2.8	15.25	9.75	1.490	0.10	2.73E+05
3	0.67	1.24E+04	2.02E+07	2.8	15.25	9.75	1.490	0.10	3.58E+05
4	0.67	1.90E+04	2.74E+07	2.8	15.25	9.75	1.490	0.10	4.32E+05
5	0.67	2.57E+04	3.38E+07	2.8	15.25	9.75	1.490	0.10	4.93E+05
6	1	3.33E+04	4.05E+07	2.8	15.25	9.75	1.490	0.10	5.52E+05
7	1	4.28E+04	4.83E+07	2.8	15.25	9.75	1.490	0.10	6.16E+05
8	1	5.23E+04	5.56E+07	2.8	15.25	9.75	1.490	0.10	6.73E+05
9	1.5	6.42E+04	6.41E+07	2.8	15.25	9.75	1.490	0.10	7.36E+05
10	1.5	7.84E+04	7.38E+07	2.8	15.25	9.75	1.490	0.10	8.03E+05
11	2	9.56E+04	1.27E+08	2.7	18.96	9.75	3.352	0.08	1.14E+06
12	2	1.16E+05	1.45E+08	2.7	18.96	9.75	3.352	0.08	1.24E+06
13	2	1.36E+05	1.63E+08	2.7	18.96	9.75	3.352	0.08	1.33E+06
14	2	1.56E+05	1.79E+08	2.7	18.96	9.75	3.352	0.08	1.42E+06

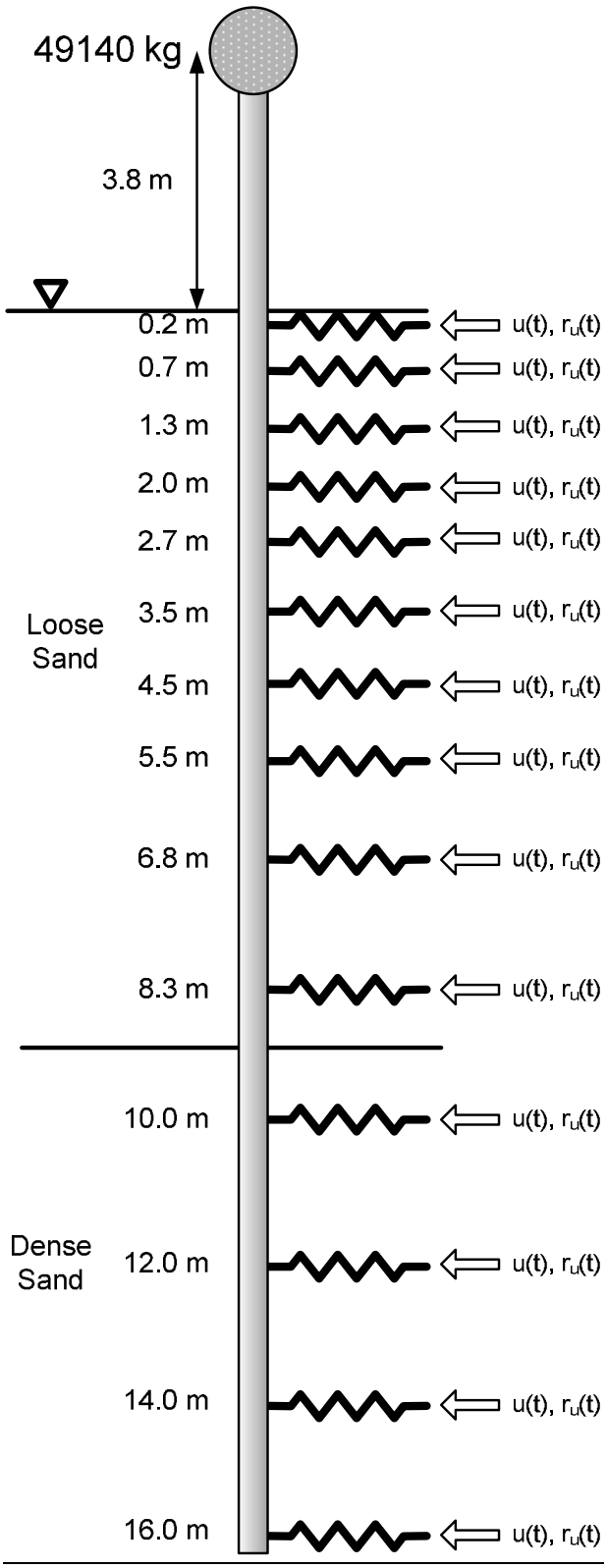

Figure 7.22 Numerical model used for simulating centrifuge tests

Model CSP_2

Figure 7.24 shows the acceleration time histories at the Pile Head, and acceleration and displacement time histories at the Superstructure for both recorded and predicted cases for event A whereas Figure 7.25 shows the same for event B. It can be seen that all the time histories are in good agreement with each other for both the events. The time histories predicted by numerical model were low pass filtered using a Butterworth filter of 4^{th} order and cutoff frequency 25.0 Hz to filter out any high frequency noise. Figure 7.23 (a) and (b) show the observed and predicted maximum moment profiles for events A and B, respectively. The bending moments are predicted quite well within 25% accuracy. Finally Figure 7.26 shows the p-y response for top six macroelements for event A and Figure 7.27 for event B. While event A doesn't mobilize the soil resistance lower than 2.0 m and the soil response below that is almost linear, significant non-linearity can be seen all the way up to 3.5 m for event B.

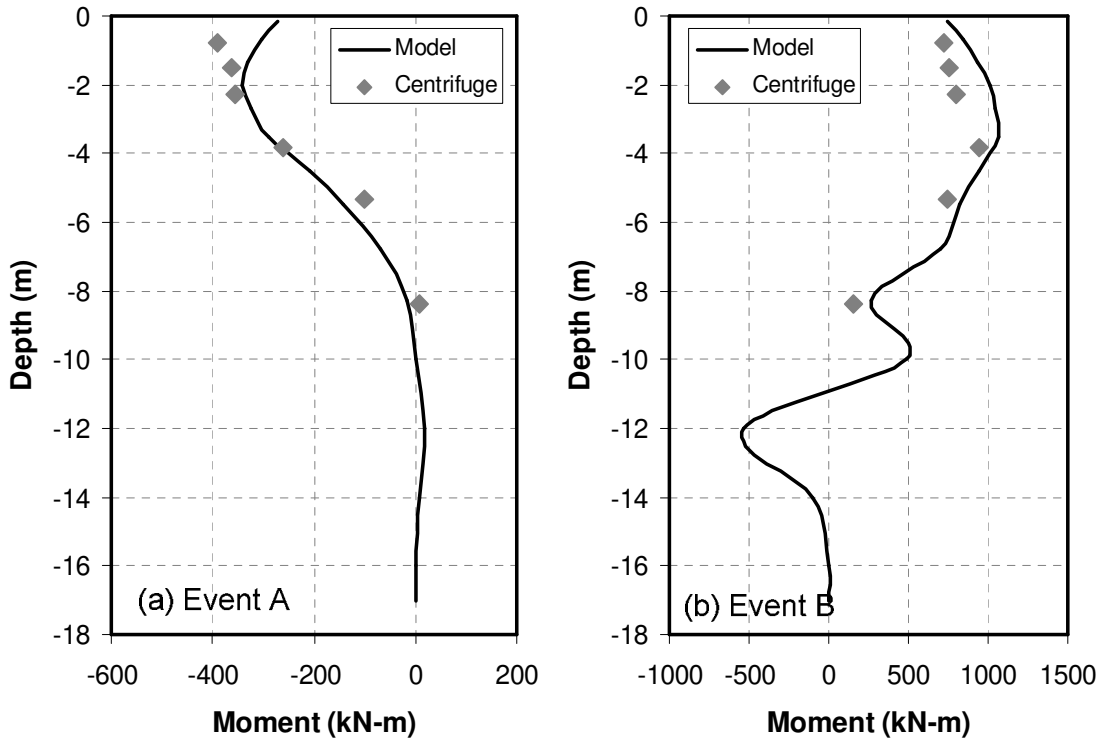

Figure 7.23 Bending Moment profiles for soil profile CSP_2 (a) Event A and (b) Event B

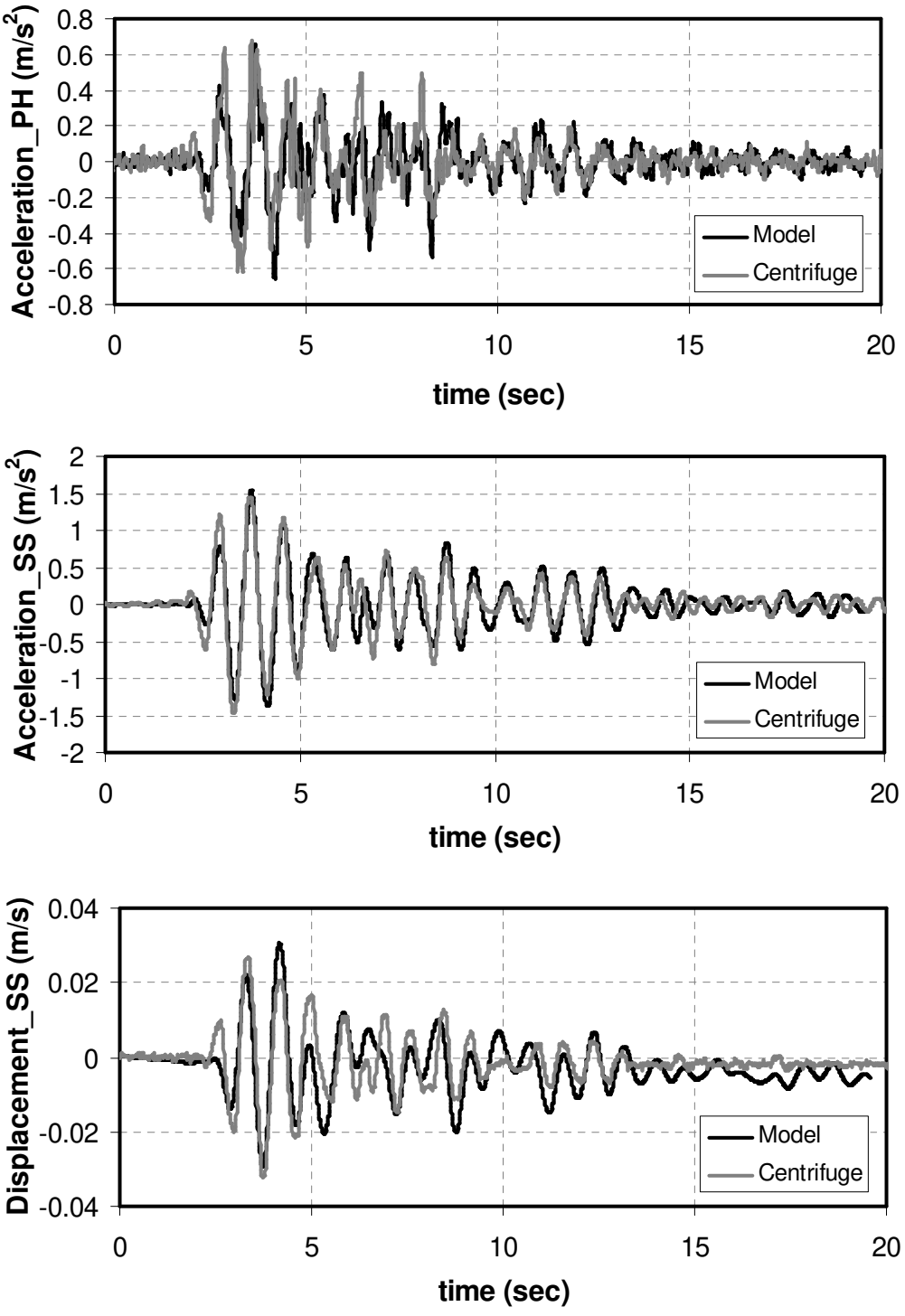

Figure 7.24 Observed and predicted time histories for CSP_2 event A

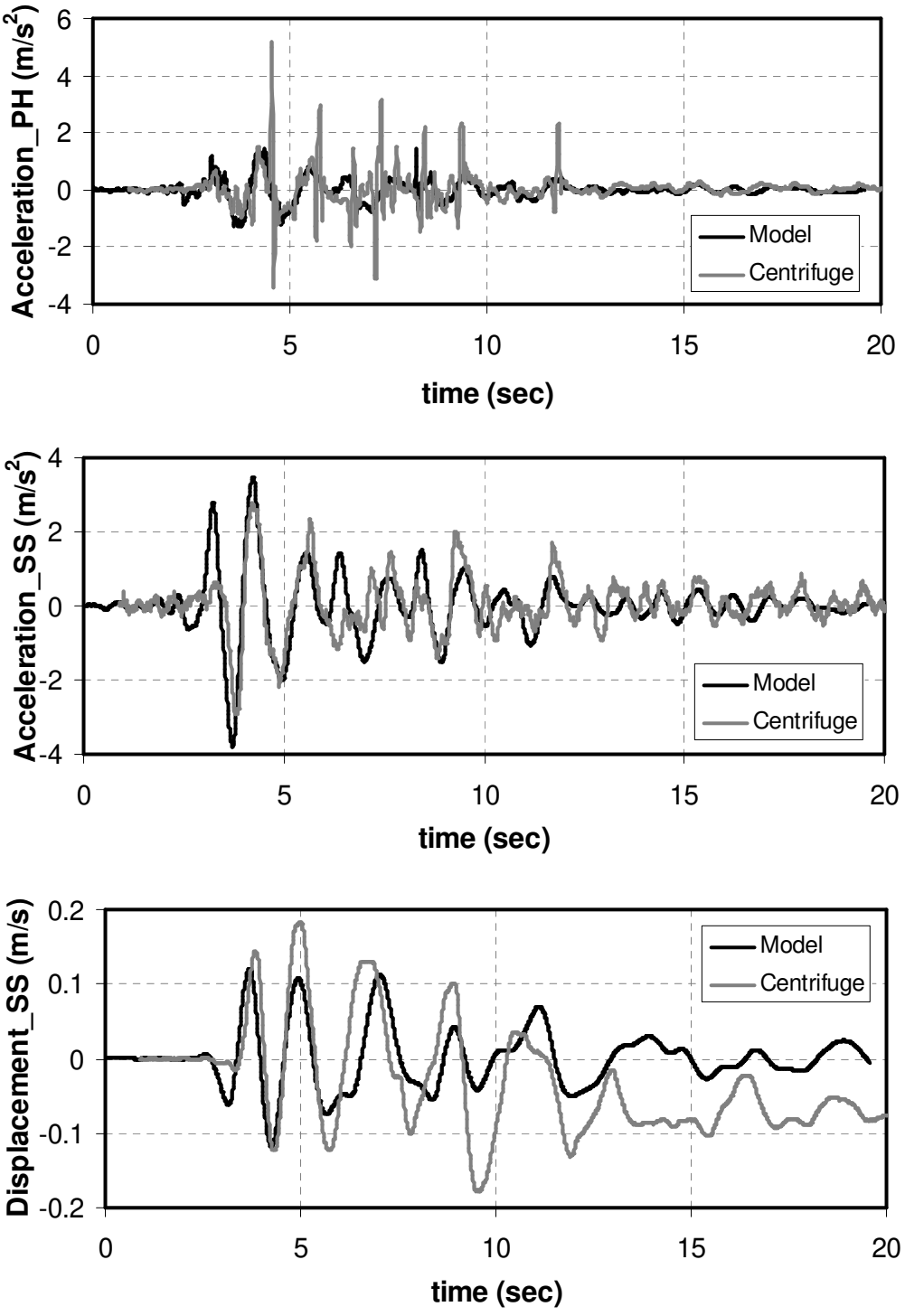

Figure 7.25 Observed and predicted time histories for CSP_2 event B

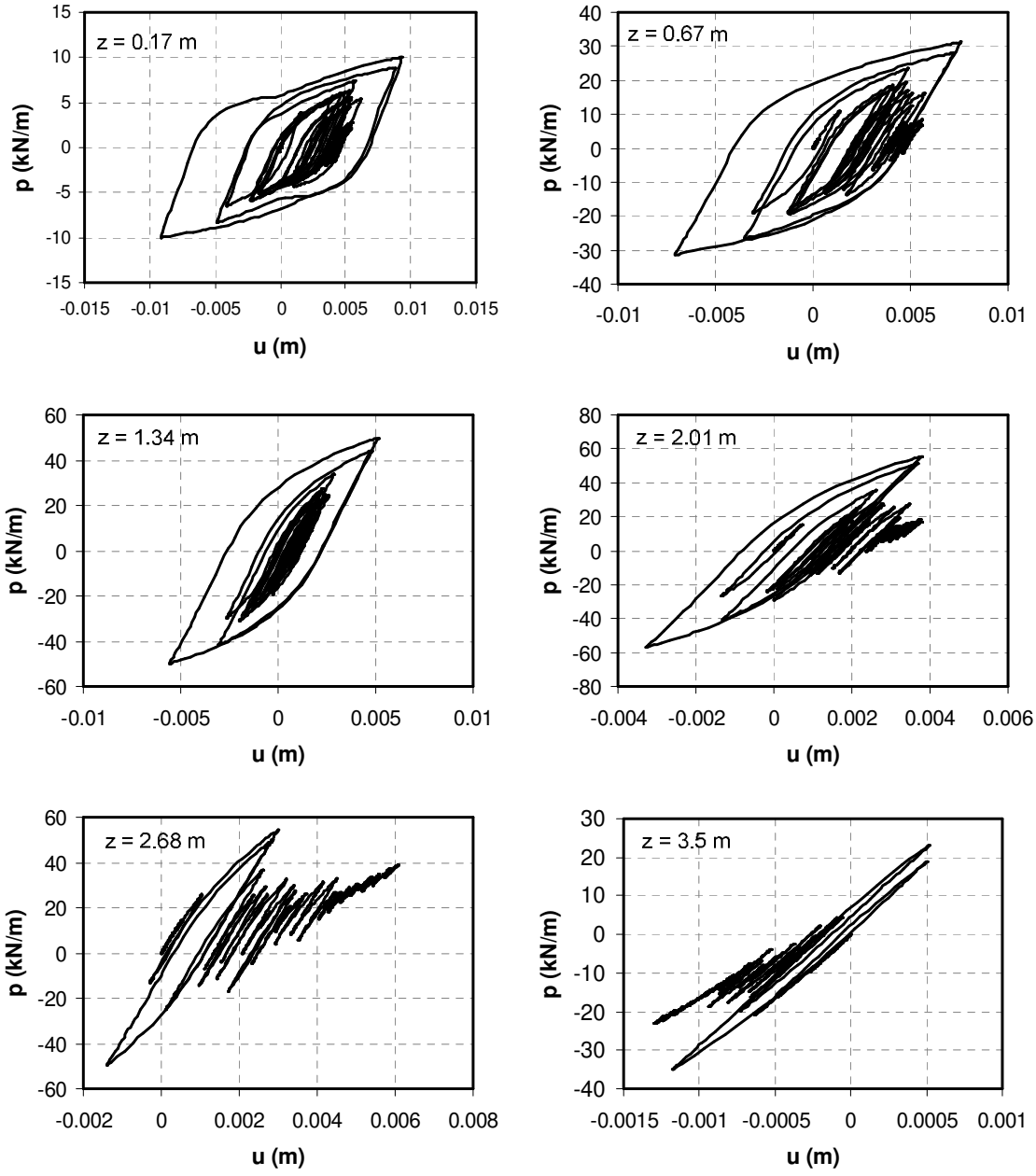

Figure 7.26 p-y response for top six macroelements for profile CSP_2 event A

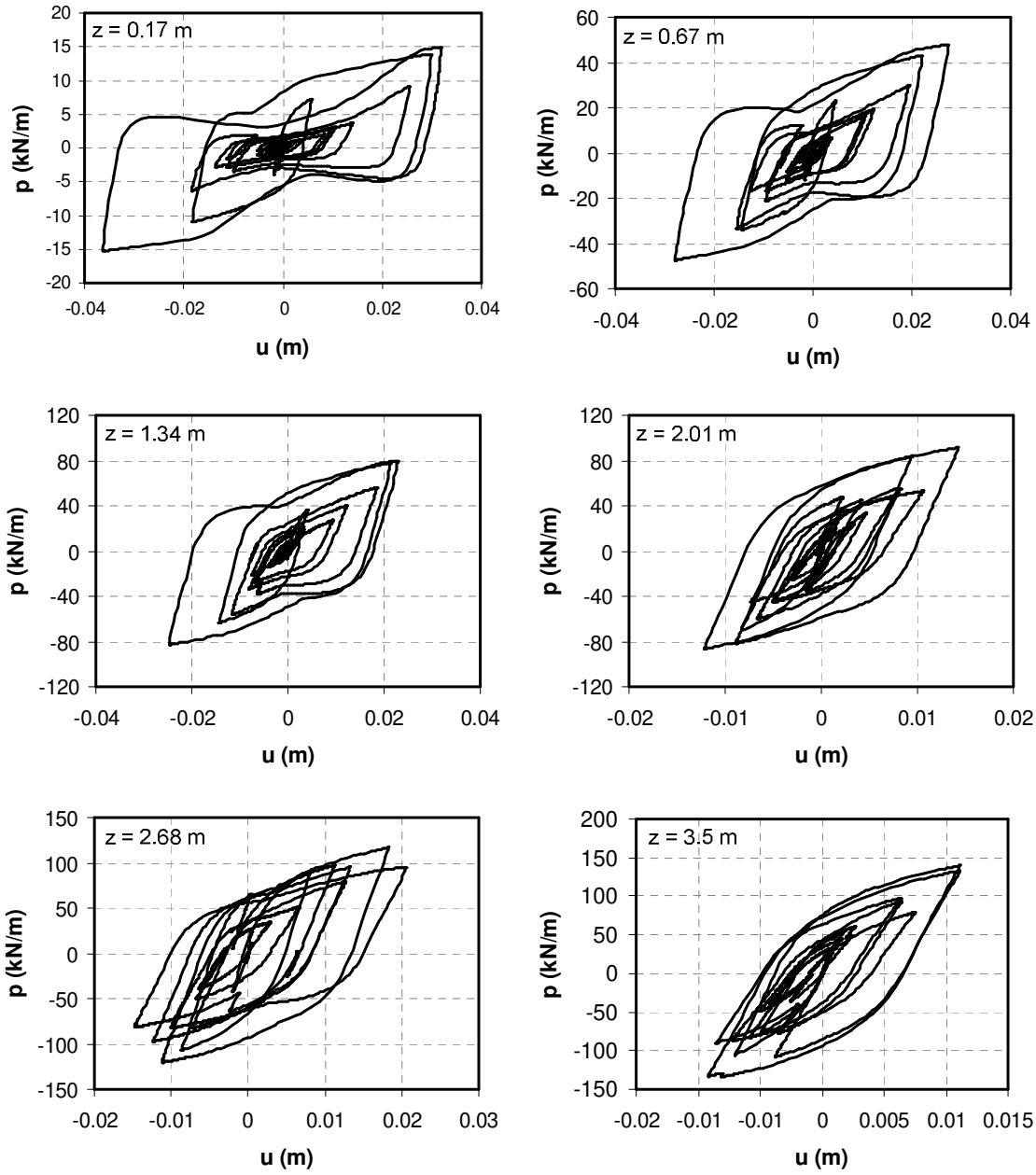

Figure 7.27 p-y response for top six macroelements for profile CSP_2 event B

Model CSP_3

Figure 7.29 shows the acceleration time histories at Pile Head, and acceleration and displacement time histories at the Superstructure for both recorded and predicted cases for event A whereas Figure 7.30 shows the same for event B. The time histories are in good agreement for event A, but for event B the numerical model predicts lower peak

accelerations (2.5 m/s^2 predicted vs. 4.0 m/s^2 observed at pile head and 5.0 m/s^2 predicted vs. 8.0 m/s^2 observed at superstructure). Similar trend is observed in bending moments in top 2 m for both event A and B as shown in Figure 7.28 (a) and (b), respectively. The bending moments are predicted quite well below 2 m but are around 25% lower for top 2 m. The reason for mismatch can be seen from Figure 7.31 that shows the p-y response for top six macroelements for event A and Figure 7.32 that shows the same for event B. When comparing the response with back calculated p-y curves presented in Wilson [58], as shown in Figure 7.33 and Figure 7.34, it can be seen that the back calculated p-y curves at 1.2 m depth show a very stiff response (even stiffer than the response for drained conditions). This could be due to excessive drag force which arises due to higher viscosity of pore fluid and problems with scaling. The stiffer response of soil in top 1.2 m compared to actual response if there were no scaling issues would result in higher moments in top 2 m and also higher accelerations.

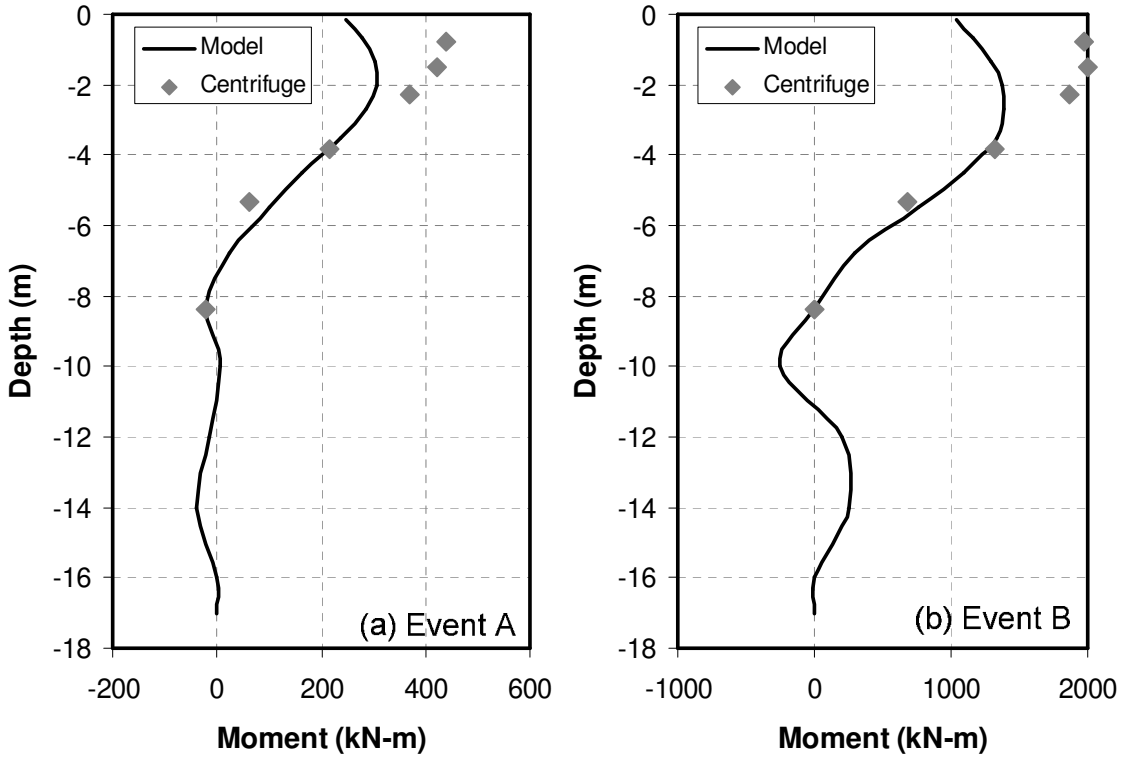

Figure 7.28 Bending Moment profiles for soil profile CSP_3 (a) Event A and (b) Event B

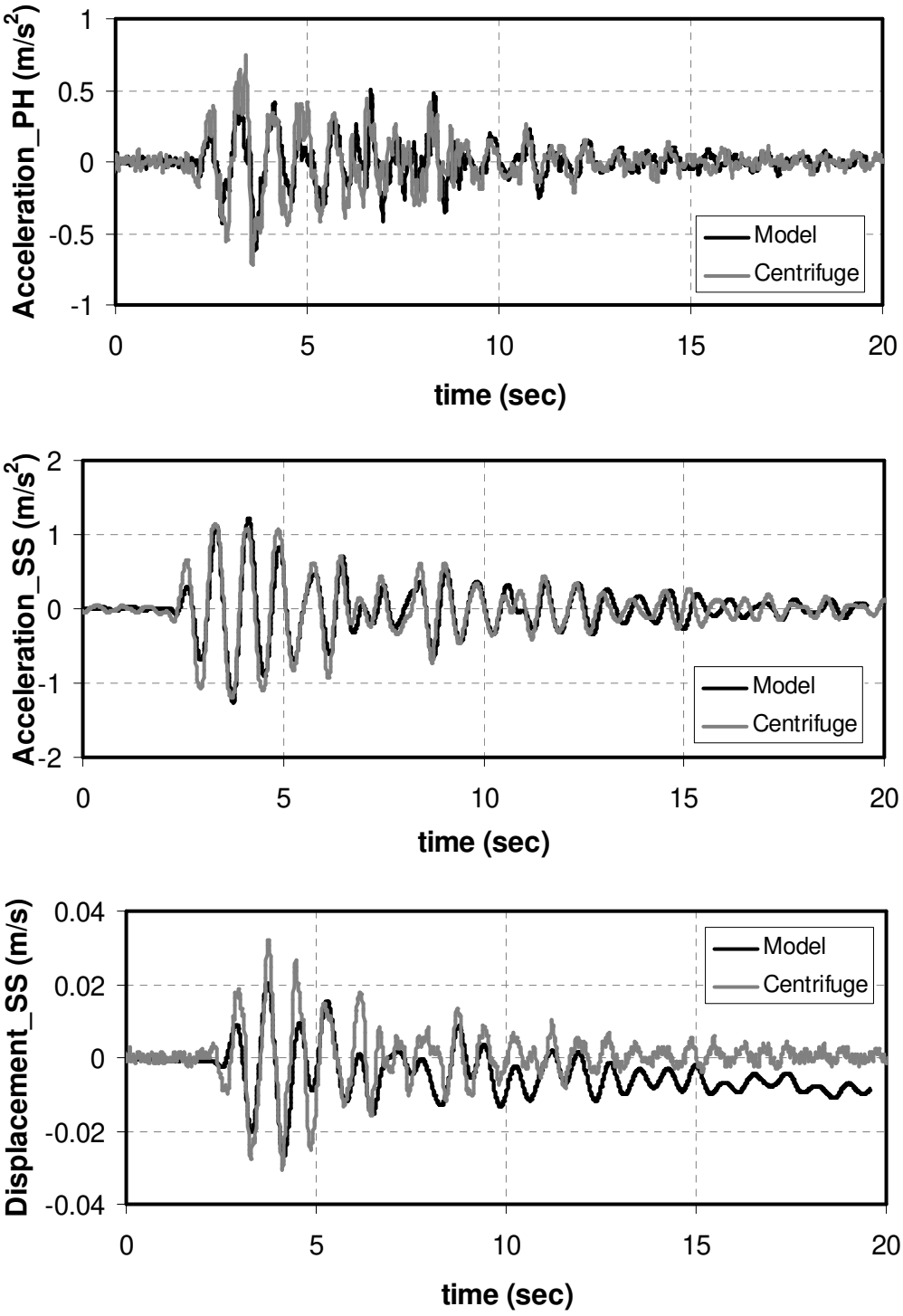

Figure 7.29 Observed and predicted time histories for CSP_3 event A

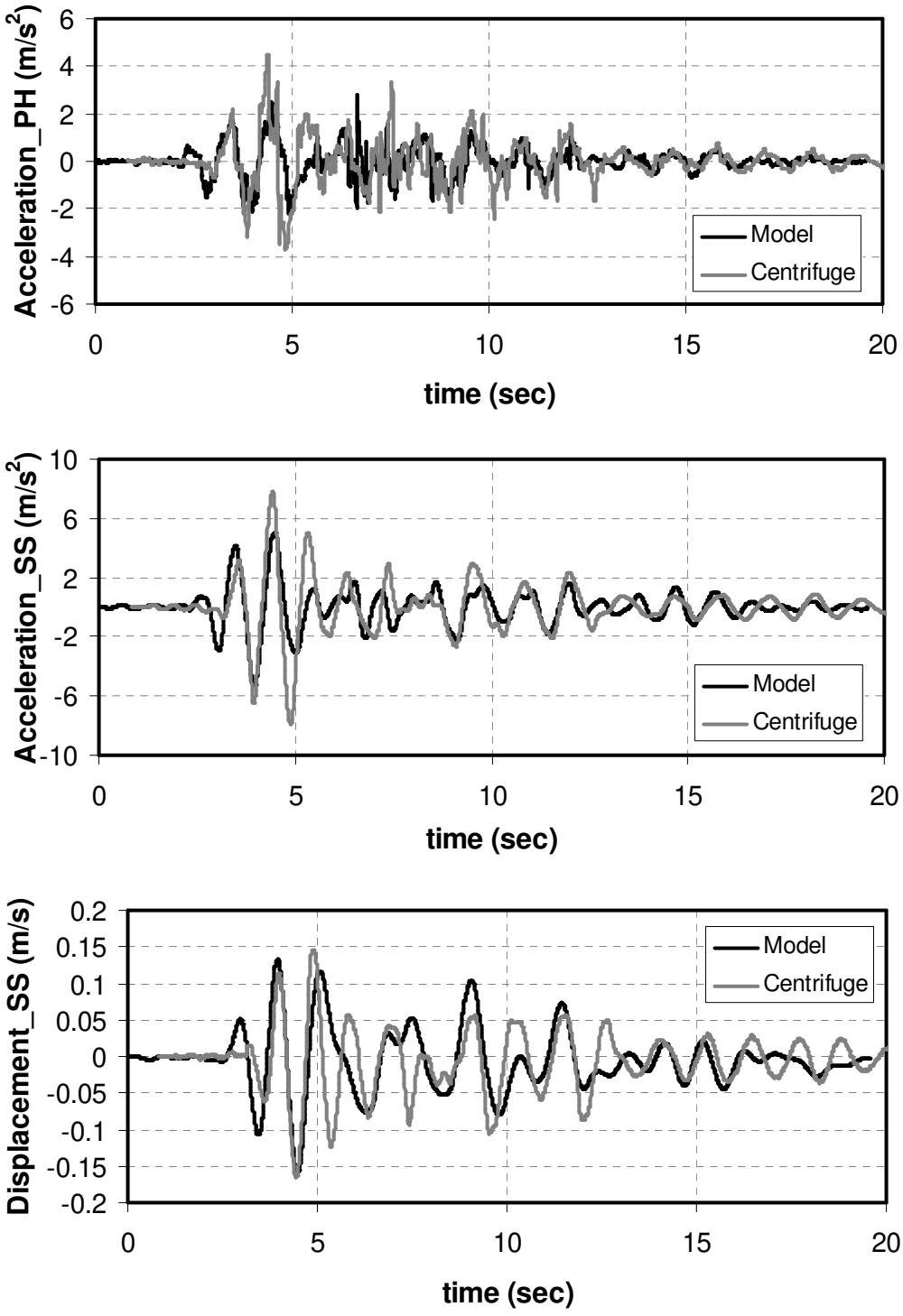

Figure 7.30 Observed and predicted time histories for CSP_3 event B

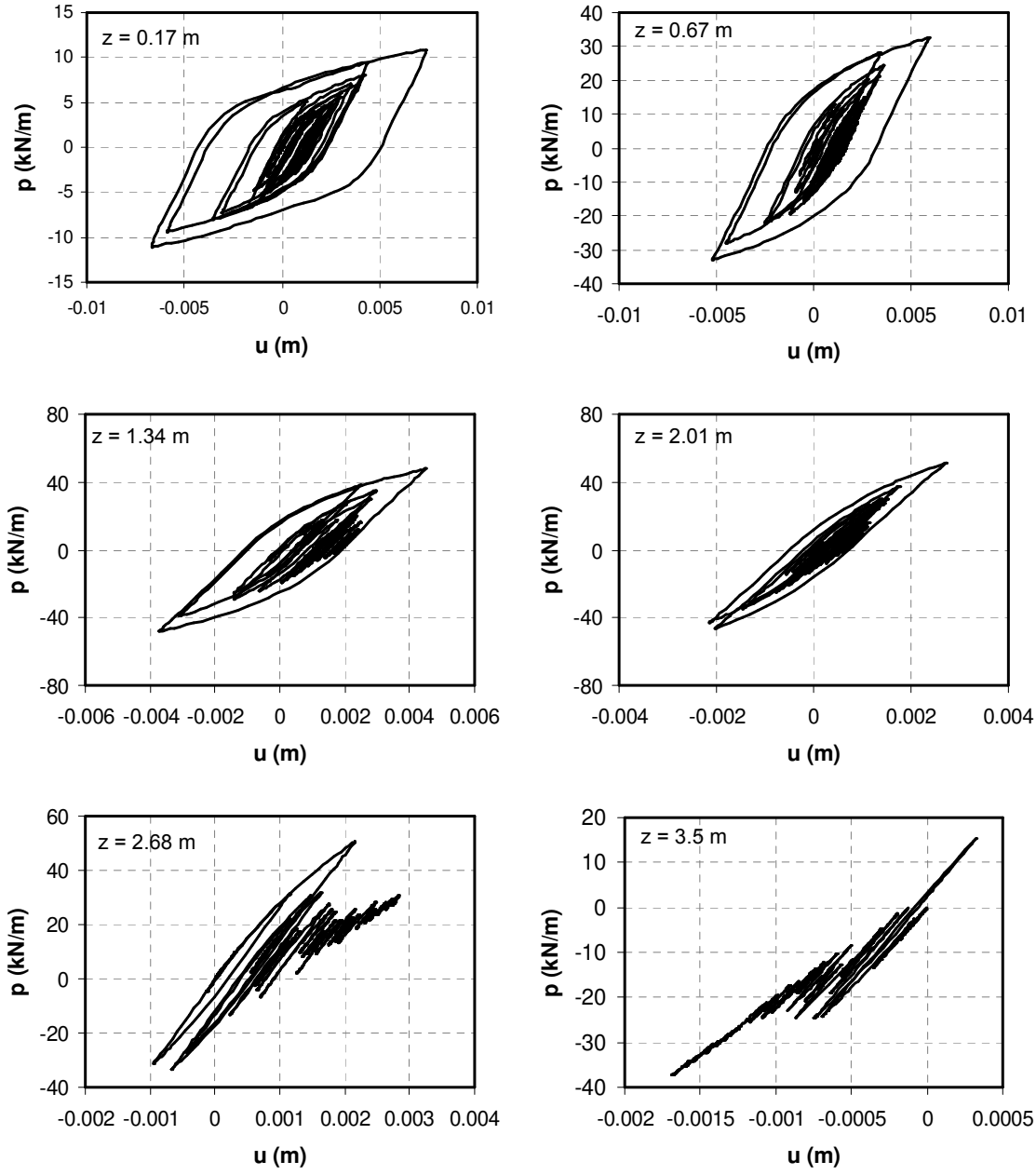

Figure 7.31 p-y response for top six macroelements for profile CSP_3 event A

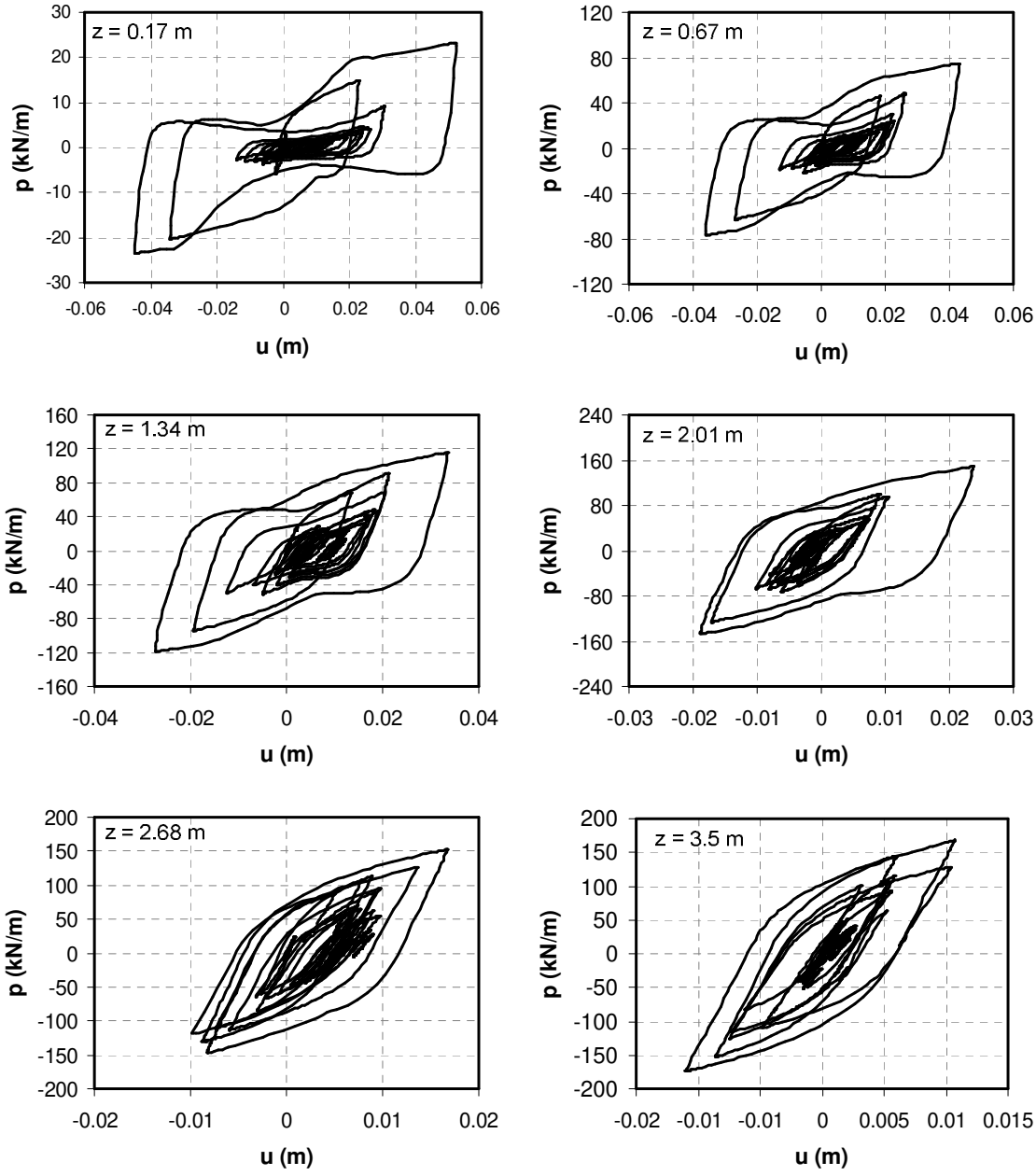

Figure 7.32 p-y response for top six macroelements for profile CSP_3 event B

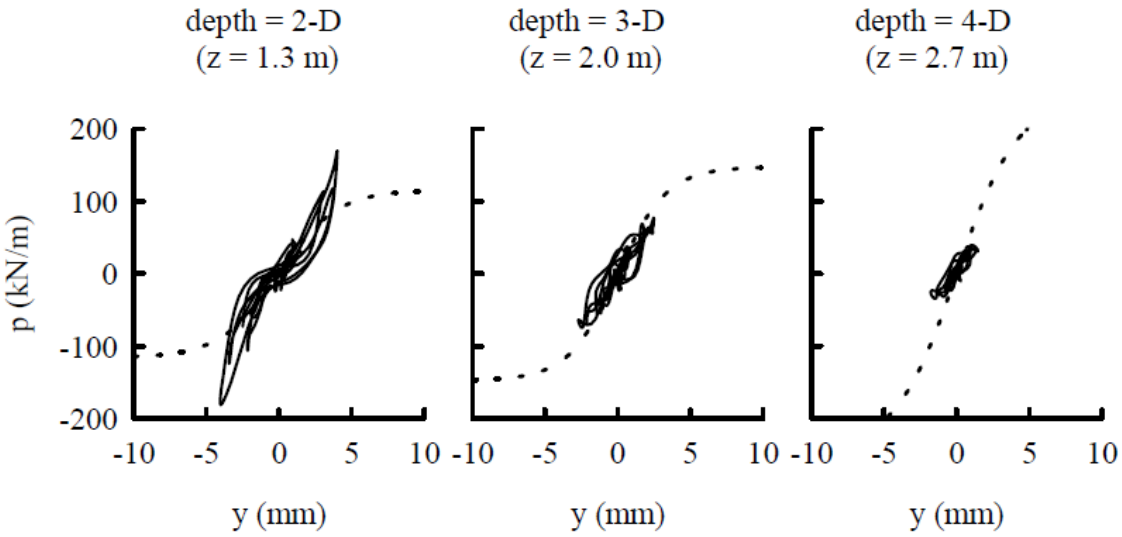

Figure 7.33 Back calculated p-y curves from CSP3_A (Wilson [58])

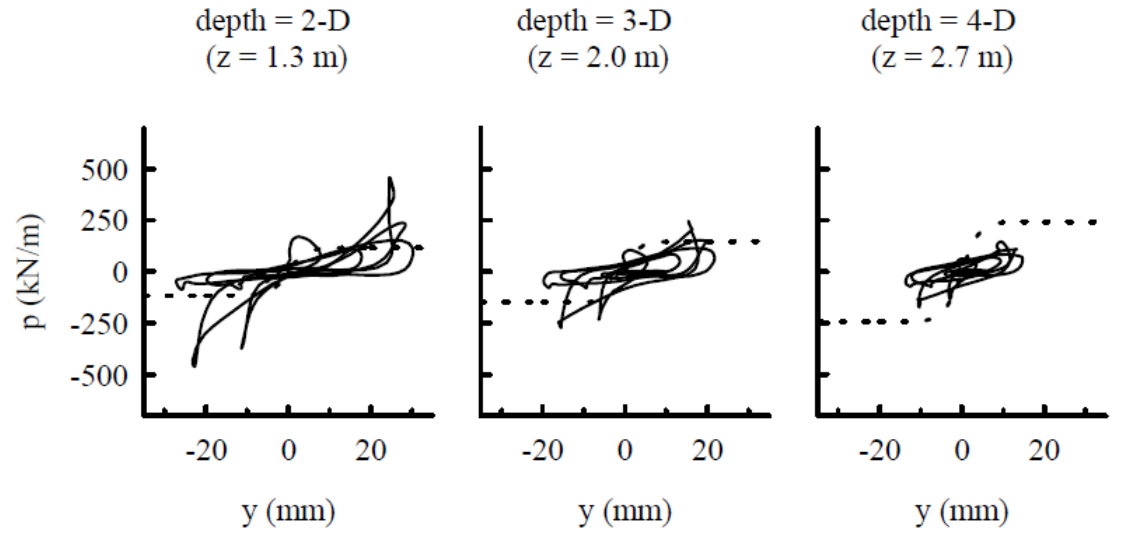

Figure 7.34 Back calculated p-y curves from CSP3_B (Wilson [58])

CHAPTER 8

MACROLEMENT FOR BIAXIAL LOADING

Introduction

Pile foundations are used quite extensively to support variety of structures especially those built on loose/soft soils. Other than vertical loads, pile foundations are often subjected to lateral loads during seismic events. Soil-structure-interaction plays an important role in evaluating the response of pile foundations to lateral loads (Mylonakis and Gazetas [100]). Various methods for analyzing seismic soil-structure interaction include finite-element or finite-difference methods and dynamic beam on non-linear Winkler foundation (BNWF) method. BNWF method, also referred to as 'p-y' approach, assumes that each layer of soil responds independently of adjacent layers of soil and hence can be replaced by a discrete spring. Though it ignores shear transfer between adjacent soil layers, it is reasonably accurate for flexible piles and being simpler and computationally less expensive than FEM, it has found extensive use in analyses of both static and dynamic problems. Backbone curves for monotonic loading have been recommended by Matlock [15], Reese et al. [16], API [17]. For cyclic and transient loading macroelements have been proposed by El Naggar and Novak [29], Boulanger et al. [47], Badoni and Makris [85] and Rha and Taciroglu [46].

In current practice, the effects of axial and lateral loads are analyzed independently. Recently, attempts have been made to emphasize the importance of coupling between vertical and lateral loading (Karthigeyan et al. [101], Rha and Taciroglu [46]). However, the coupling between two perpendicular directions in lateral loading has still been ignored so far. The authors are not aware of any study to date that documents the response of piles to bidirectional lateral loading even though seismic loading is essentially bidirectional in nature.

The objective of this research is to develop and calibrate a macroelement model that can capture the soil resistance exerted on the pile during bidirectional loading. The macroelement is developed by modifying and extending the Bouc-Wen (Bouc [83]; Wen [84]) model based on physical mechanism of soil resistance. The ability of such models in successfully predicting soil-pile interaction has been demonstrated before by Badoni and Makris [85], Gerolymos & Gazetas [49] and Varun & Assimaki [102]. The macroelement is then calibrated using 3D finite element analyses due to lack of any experimental data. Finally, the importance of coupling is demonstrated by comparing the predictions from uncoupled and coupled model for transient motions from three different earthquakes.

Uniaxial Hysteresis Model

For a simple hysteresis model based on Bouc-Wen model, the restoring force can be written in the following form with an elastic and a plastic component as

$$p = \alpha k u + (1-\alpha)\, p_y \zeta \tag{8.1}$$

where p_y is the yield strength, k is the initial stiffness, α is the post yield stiffness to initial stiffness ratio and ζ is the hysteretic parameter governed by the following differential equation

$$d\zeta = \left(1 - |\zeta|^n \left(b + g\,\mathrm{sgn}\left(du.\zeta\right)\right)\right)\frac{du}{u_y} \tag{8.2}$$

where $u_y = p_y / k$ is the yield displacement, (b, g) are parameters controlling unloading-reloading stiffness such that $g = 1 - b$ and n is a parameter controlling sharpness of hysteresis before yielding (higher values of n correspond to a bilinear backbone curve). For the purpose of modeling pile response in soils, the post yield stiffness is zero, hence $\alpha = 0$. Also, the function $|\zeta|^n$ can be replaced with any function f_ζ or $f(\zeta)$ as long

as it is a monotonically increasing function of ζ and satisfies $f(0)=0$ and $f(1)=1$. In that case equation above can be written as

$$d\zeta = \left(1 - f_\zeta\left(b + g\,\mathrm{sgn}\left(du.\zeta\right)\right)\right)\frac{du}{u_y} = K\frac{du}{u_y} \tag{8.3}$$

where K is the normalized tangent stiffness as a function of ζ.

Biaxial Hysteresis Model

Physical Meaning of Formulation

The uniaxial model is extended to biaxial case by means of the actual physical mechanisms involved. When the pile moves forward, passive resistance is mobilized in front of the pile and a small volume of soil is pushed into non-linear (plastic) range. As displacement increases, the soil resistance increases but volume of soil in front of pile that is in plastic state also increases, thereby causing the stiffness (incremental resistance *dp* for a given incremental displacement *du*) to decrease.

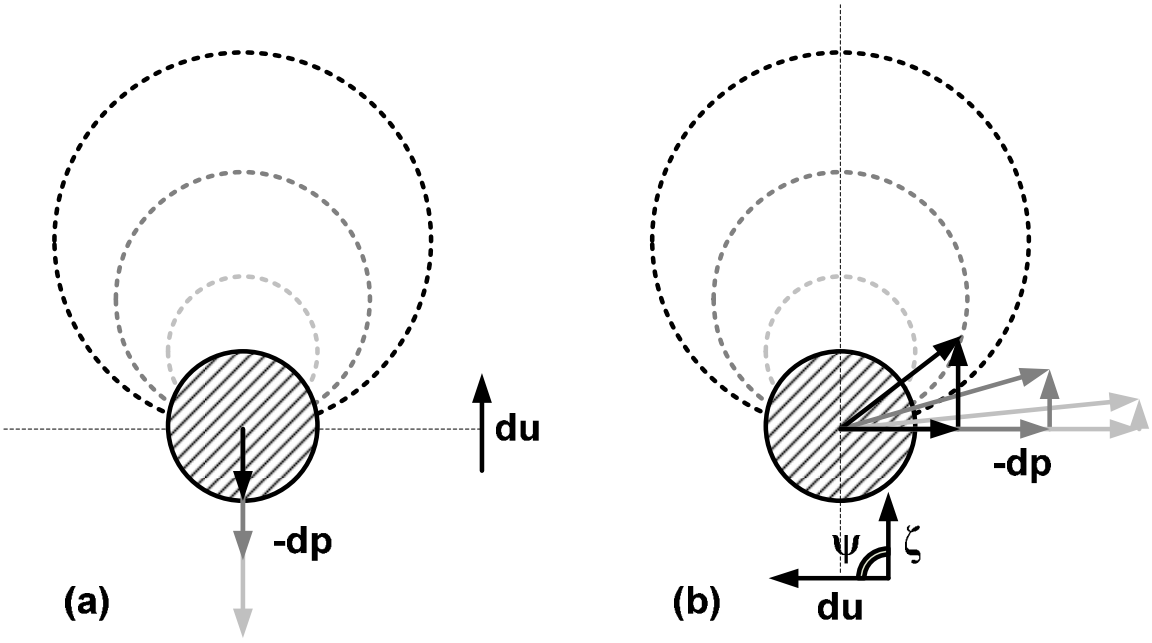

Figure 8.1 Restoring force as a function of degree of non-linearity for (a) incremental displacement along same direction (b) incremental displacement perpendicular to zeta

Figure 8.1 shows the restoring force $p(\zeta)$ as a function of degree of non-linearity (ζ) for the case of uniaxial loading. For biaxial case, after loading the pile uniaxially to a certain degree of non-linearity, it is loaded in a different direction such that incremental displacement $\overrightarrow{du}$ makes an angle ψ with hysteretic vector $\vec{\zeta}$. Due to the change in loading direction, there is lesser volume of plastic soil in the front half of the pile and hence the tangent stiffness is higher than the case if the pile was loaded uniaxially in the same direction. The tangent stiffness is expected to increase as a function of the angle ψ with the stiffness being minimum at $\psi = 0$ and maximum at $\psi = \pi$. Also, since the stress state in soil in front of the pile is not symmetric anymore, the incremental resistance dp will not be in the same direction as incremental displacement du and will make an angle with the incremental displacement. The angle is expected to be a function of degree of asymmetry in stress state in soil in front of the pile as shown in Figure 8.2. It is zero for $\psi = 0, \pi$ but will be maximum for $\psi = \pi/2$.

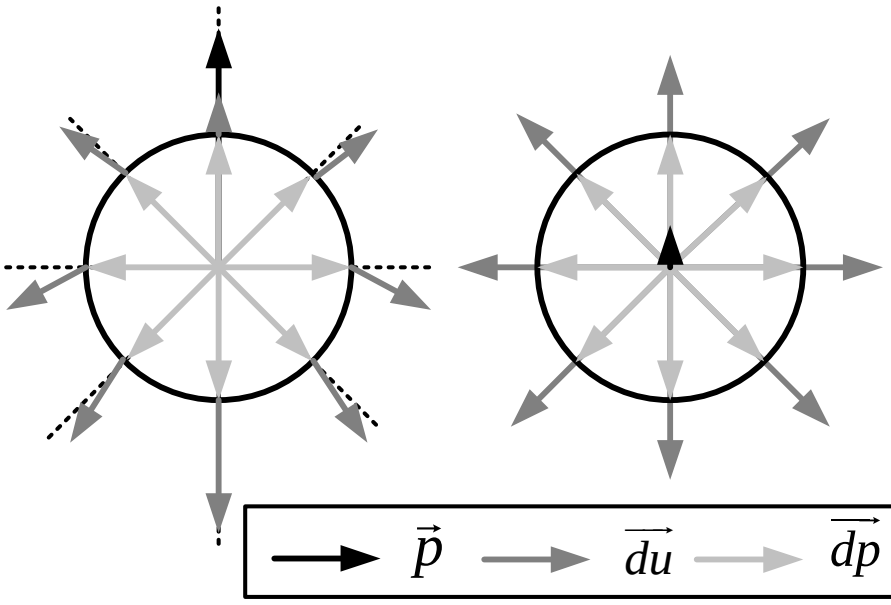

Figure 8.2 Incremental reaction force (magnitude and direction) as a function of incremental displacement for (a) high degree of non-linearity (b) very low non-linearity

Formulation for Biaxial Model

In case of 2D loading, the resultant force p, hysteretic parameter ζ and displacement du, all have two components and can be written as vectors $\vec{a} = a_1\hat{i} + a_2\hat{j}$ where $a = |a| = \sqrt{a_1^2 + a_2^2}$ is the magnitude and $\tan\theta = \frac{a_2}{a_1}$, θ being the angle made by $\vec{a}$ with axis-1. While the elastic part of the restoring force can be calculated easily by using superposition principle, the equation for plastic part of restoring force can be written as

$$\vec{p} = p_y\vec{\zeta} \tag{8.4}$$

Where the Hysteresis parameter $\overrightarrow{d\zeta}$ is calculated in a similar fashion as

$$\overrightarrow{d\zeta} = \overline{\overline{K}}_\theta \frac{\overrightarrow{du}}{u_y} \tag{8.5}$$

$\overline{\overline{K}}_\theta$ is the tangent stiffness tensor along any set of axes that make an angle θ_{du} with the principal axes. The principal axes for any load increment are the set of axes where axis-1 is aligned with incremental displacement vector $\overrightarrow{du}$. The tangent stiffness tensor along any axes $\overline{\overline{K}}_\theta$ is obtained using the transformation tensor $\overline{\overline{\theta}}_{du}$ and tangent stiffness tensor along principal axes $\overline{\overline{K}}$ as

$$\overline{\overline{K}}_\theta = \overline{\overline{\theta}}_{du}^{T}\,\overline{\overline{K}}\,\overline{\overline{\theta}}_{du} \tag{8.6}$$

where

$$\overline{\overline{\theta}}_{du} = \begin{bmatrix} \cos\theta_{du} & \sin\theta_{du} \\ -\sin\theta_{du} & \cos\theta_{du} \end{bmatrix} = \frac{1}{du}\begin{bmatrix} du_1 & du_2 \\ -du_2 & du_1 \end{bmatrix} \tag{8.7}$$

$$\overline{\overline{K}} = \begin{bmatrix} k_{11} & k_{12} \\ k_{21} & k_{22} \end{bmatrix} \tag{8.8}$$

Here k_{ii} is the diagonal stiffness term and k_{ij} is the cross-stiffness term. For the case of an isotropic medium, $k_{11} = k_{22} = k_{ii}$ and $k_{12} = k_{21} = k_{ij}$. The tangent stiffness tensor can thus be written as

$$\overline{\overline{K}}_{\theta} = \begin{bmatrix} k_{ii} - k_{ij}\sin(2\theta_{du}) & k_{ij}\cos(2\theta_{du}) \\ k_{ij}\cos(2\theta_{du}) & k_{ii} + k_{ij}\sin(2\theta_{du}) \end{bmatrix} \tag{8.9}$$

As discussed in the section above, the formulation for stiffness terms is based on following criteria

(a) When du acts along the same line as ζ, the 2D model should reduce to 1D model, i.e.,

$k_{ii} = \left(1 - f_{\zeta}\left(b+g\right)\right)$ for $\psi = 0$ and $k_{ii} = \left(1 - f_{\zeta}\left(b-g\right)\right)$ for $\psi = \pi$

$k_{ij} = 0$ for $\psi = 0, \pi$

(b) When $\zeta = 0$, the system has no memory and the 2D model is the same as 1D model for the very next load increment, i.e., $k_{ij} = 0$.

For the diagonal stiffness term, the normalized dot product is used to replace the sign function in 1D model so that it still has the same value of 1 and -1 for the extreme cases of $\psi = 0$ and $\psi = \pi$, respectively but provides a smooth interpolation in between.

$$k_{ii} = \left(1 - f_{\zeta}\left(b + g\cos\psi\right)\right) \tag{8.10}$$

$$\cos\psi = \frac{du \bullet \zeta}{du\ \zeta} = \frac{du_1\zeta_1 + du_2\zeta_2}{du\ \zeta} \tag{8.11}$$

For the cross-stiffness term, the following form is proposed which satisfies $k_{ij} = 0$ when either $\zeta = 0$ or $\sin\psi = 0$.

$$k_{ij} = cf_{\zeta}\sin\psi \tag{8.12}$$

$$\sin\psi = \frac{\left|\overrightarrow{du} \times \vec{\zeta}\right|}{du\ \zeta} = \frac{du_1\zeta_2 - du_2\zeta_1}{du\ \zeta} \tag{8.13}$$

Using

$$\overrightarrow{du} = \begin{bmatrix} du_1 \\ du_2 \end{bmatrix} = \begin{bmatrix} \cos\theta_{du} \\ \sin\theta_{du} \end{bmatrix} du \tag{8.14}$$

We get

$$\overrightarrow{d\zeta} = \begin{bmatrix} d\zeta_1 \\ d\zeta_2 \end{bmatrix} = \begin{bmatrix} \left(k_{ii} - k_{ij}\sin(2\theta_{du})\right)\cos\theta_{du} + k_{ij}\cos(2\theta_{du})\sin\theta_{du} \\ k_{ij}\cos(2\theta_{du})\cos\theta_{du} + \left(k_{ii} + k_{ij}\sin(2\theta_{du})\right)\sin\theta_{du} \end{bmatrix} \frac{du}{u_y} \tag{8.15}$$

$$\overrightarrow{d\zeta} = \begin{bmatrix} d\zeta_1 \\ d\zeta_2 \end{bmatrix} = \begin{bmatrix} k_{ii}\cos\theta_{du} - k_{ij}\sin\theta_{du} \\ k_{ii}\sin\theta_{du} + k_{ij}\cos\theta_{du} \end{bmatrix} \frac{du}{u_y} \tag{8.16}$$

The magnitude of increment in hysteresis parameter is calculated as

$$d\zeta = |d\zeta| = \sqrt{d\zeta_1^2 + d\zeta_2^2} = \sqrt{k_{ii}^2 + k_{ij}^2}\,\frac{du}{u_y} = K\frac{du}{u_y} \tag{8.17}$$

Range for Parameter c

The range for parameter c in the cross-stiffness term can be determined using the following criteria

CRITERIA 1: The maximum load cannot exceed p_y or $\zeta \le 1$. This condition translates to

$$\left.\frac{d|\zeta|}{du}\right|_{\zeta=1} \le 0 \tag{8.18}$$

$$\frac{d|\zeta|}{du} = \frac{\zeta_1\frac{d\zeta_1}{du} + \zeta_2\frac{d\zeta_2}{du}}{|\zeta|} = \cos\theta_\zeta\frac{d\zeta_1}{du} + \sin\theta_\zeta\frac{d\zeta_2}{du} \tag{8.19}$$

$$\Rightarrow k_{ii}\cos\left(\theta_{du} - \theta_\zeta\right) - k_{ij}\sin\left(\theta_{du} - \theta_\zeta\right) = k_{ii}\cos(\psi) - k_{ij}\sin(\psi) \le 0 \tag{8.20}$$

$$\Rightarrow \cos\psi - f_\zeta\left(b\cos\psi + g\cos^2\psi + c\sin^2\psi\right) = -c/g + \cos\psi - (1-c/g)\cos^2\psi \le 0 \tag{8.21}$$

Case 1: If $c \ge g$, then maxima occurs at $\cos\psi = 1$ and is equal to 0. Thus, the inequality is satisfied for all values of ψ if $c \ge g$.

Case 2: If $c < g$, then maxima occurs at $\cos\psi = -1 \le \dfrac{1}{2(1-c/g)} \le 1$.

If $g/2 \le c < g$, maxima occurs at $\cos\psi = 1$ again and the inequality is satisfied for all values of ψ.

If $0 \le c < g/2$, the maximum value is $\frac{1}{4(1-c/g)} - c/g > 0$ for $c < g/2$. Hence, the inequality is not satisfied for all values of ψ.

Thus, $c \ge g/2$ for $\frac{d|\zeta|}{du} \le 0$, when $\zeta = 1$.

CRITERIA 2: As the magnitude of non-linearity in soil increases, the stiffness should decrease, i.e., for any given ψ, $\frac{dK}{d\zeta} \le 0$

For 1D case

$$\frac{dK}{d\zeta} = -f'_\zeta (b + g\cos\psi) \le 0 \qquad (8.22)$$

Since $f'_\zeta > 0$, the above inequality is satisfied for all values of ψ if $b \ge g$, i.e., $g \le 1/2$.

For 2D case

$$\frac{dK}{d\zeta} = \frac{1}{K}\left(k_{ii}\frac{dk_{ii}}{d\zeta} + k_{ij}\frac{dk_{ij}}{d\zeta} \right) = \frac{f'_\zeta}{K}\left(-\left(b + g\cos\psi\right) + f_\zeta \left(\left(b + g\cos\psi\right)^2 + c^2\sin^2\psi \right) \right) \qquad (8.23)$$

$$\Rightarrow -\left(b + g\cos\psi\right) + f_\zeta \left(2b\left(b + g\cos\psi\right) + g^2\cos^2\psi - b^2 + c^2\sin^2\psi \right) \le 0 \qquad (8.24)$$

$$\Rightarrow \left(2(1-g)\, f_\zeta - 1\right)\left(1 - g + g\cos\psi\right) + f_\zeta \left(c^2 + (1-g)^2 + (g^2 - c^2)\cos^2\psi \right) \le 0 \qquad (8.25)$$

If $c \le g$, then maxima occurs at $\cos\psi = -1$ and is equal to $-(b-g)\left(1 - f_\zeta (b-g)\right)$. Since, $b \ge g$ and $f_\zeta (b-g) \le 1$, the inequality is satisfied for all values of ψ if $c \le g$.

Thus, $c \le g$ and $g \le 1/2$ for $\frac{dK}{d\zeta} \le 0$.

Combining together both the conditions, we get

$c \in [g/2, g]$ where $g \in [0, 1/2]$

Extension to asymmetric and orthotropic cases

The model described above assumes isotropic conditions in horizontal plane, i.e., homogenous soil and same boundary condition. However, this may not always be the case, e.g., piles in pile groups and piles on sloping ground. The proposed model can easily be extended to these conditions as follows.

Piles in pile groups: The ultimate resistance and initial stiffness of piles in groups is a function of pile spacing as shown in Figure 8.3. For case of medium to high non-linearity, the influence of piles other than the adjacent ones can be neglected and the problem can be reduced to an orthotropic system. The orthotropic system can be converted to an isotropic system using coordinate transformation (Park et al. [103]) as

$$u_2' = \frac{u_{y1}}{u_{y2}} u_2 \text{ and } p_2' = \frac{K_1 u_{y1}}{K_2 u_{y2}} p_2 \tag{8.26}$$

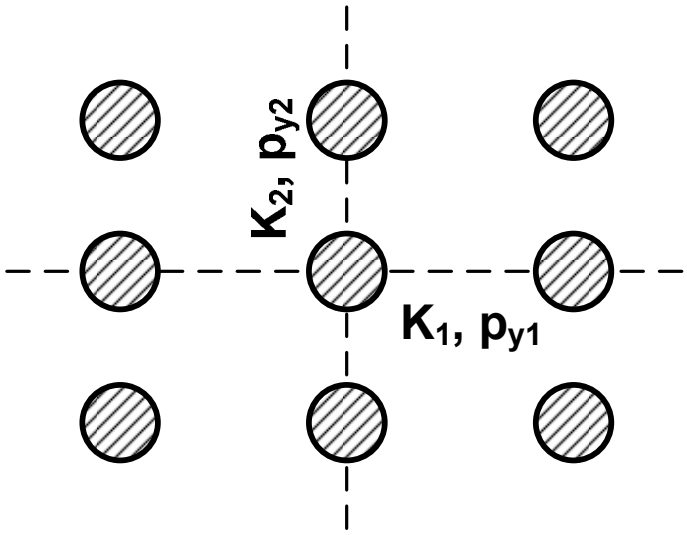

Figure 8.3 Ultimate resistance and initial stiffness for pile in pile group

Piles in sloping ground: The system is symmetric in direction perpendicular to sloping ground whereas it is asymmetric in the sloping direction. However, by choosing the axes carefully, it can be reduced to two identical asymmetric systems as shown in Figure 8.4.

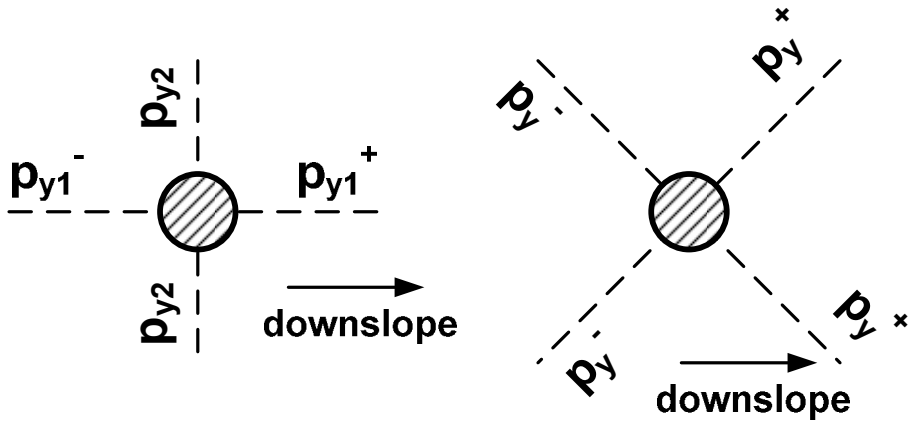

Figure 8.4 Asymmetry in ultimate resistance for pile in sloping ground

Using the approach by Wang and Wen [104], the asymmetry can then be accounted for as

$$p_y = \left(1 + sign(\zeta)\right) p_y^+ + \left(1 - sign(\zeta)\right) p_y^- \tag{8.27}$$

Where p_y^+ and p_y^- are the ultimate strength along positive and negative axis, respectively.

Comparison with 3D FEM Analyses

Since, limited results are available for bidirectional lateral loading of piles; the model is calibrated and verified by means of comparison with 3D FEM analyses.

Numerical Framework

Numerical simulations are performed using the finite element computer code DYNAFLOW (Prevost [70]). Since the loading and geometry no longer have an axis of symmetry, a full model is used instead of a half model as used in previous analyses.

Table 8.1 Material parameters for the soil model

Property	Symbol	Range
Elastic Parameters		
Shear Modulus	G_s	2 MPa
Bulk Modulus	K_s	4 MPa
Power Exponent	n	0.5
Yield Parameters		
Peak Friction Angle	φ	32°
Max. shear strain	γ_{max}	0.08

A detailed description of the model is provided in chapter 3 itself. The soil parameters used are provided in Table 8.1.

Calibration

Figure 8.5 shows the pile response in terms of soil resistance per unit length vs. displacement (p-y) curves as a function of cyclic displacement amplitude for a pile with diameter B = 1m and soil at depth D = 2 m..

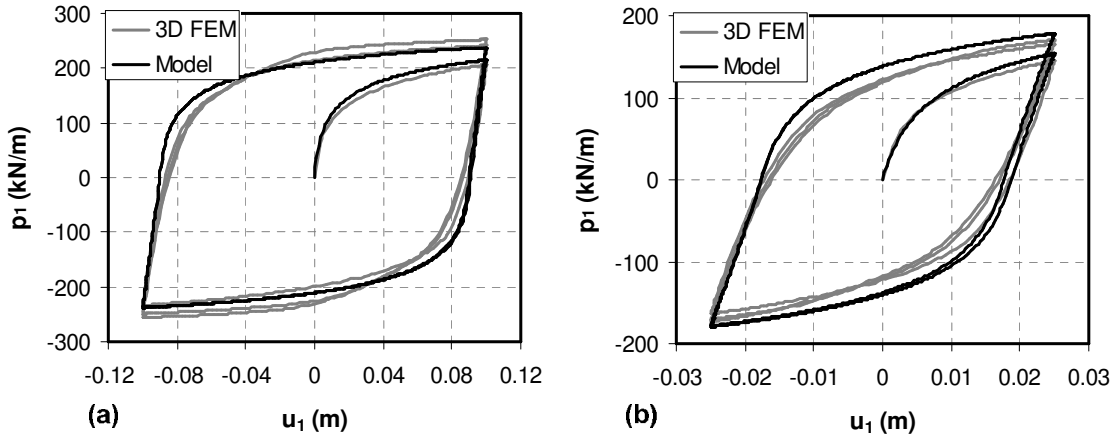

Figure 8.5 Comparison of pile response to uniaxial cyclic loading from FEM and proposed model for displacement amplitude (a) u_1=0.1 m (b) u_1=0.025 m

Varun & Assimaki [102] calibrated a uniaxial hysteresis model based on FEM simulations where the model parameters are related to soil parameters as following

(a) The initial stiffness of model

$$K = 1.25E_s \tag{8.28}$$

Where E_s is the Young's modulus of soil

(b) Yield strength or ultimate soil resistance per unit length

$$p_y = \left(3.25K_p + 0.3K_p^2\right)B\sigma_v' \tag{8.29}$$

Where $K_p = \tan^2\left(45 + \varphi/2\right)$ is the coefficient of passive earth pressure and φ is the friction angle for soil.

(c) Backbone curve

A backbone function of $f_\zeta = \tanh\left(n|\zeta|\right)/\tanh\left(n\right)$ is used instead of $f_\zeta = |\zeta|^n$. A value of n=2.7 for dense sands (γ_{max}=0.04), 2.8 for medium-dense (γ_{max}=0.06) and 2.9 for loose sands (γ_{max}=0.08) is recommended.

(d) Unloading-Reloading stiffness parameters

b = 0.6 and g = 0.4

(e) Cross-stiffness parameter

The pile is loaded uniaxially in x_1- direction upto displacement levels of 0.025, 0.05 and 0.1 m followed by loading in x_2-direction upto 0.1 m. The cross-stiffness parameter c is calibrated by matching the unloading (force relaxation) curves in x_1-direction as displacement in x_2-direction increases (Figure 8.6). A value of $c = 0.25$ is used based on the best fit.

Comparison with cyclic loading

The results from FEM analyses are next compared with the predictions from the model. In order to evaluate the coupling in both directions, two types of loading patterns are used as shown in Figure 8.7.

<u>0 shaped loading</u>

In case of 0-shaped loading, when the displacement in one direction is maximum, it is minimum in the other direction and vice-versa. Thus, when loading is taking place along one direction, unloading takes place along the other direction. Results are presented for amplitude of displacement along x_1 being 0.025 m (lesser degree of non-linearity) in Figure 8.9(a)-(c) and 0.1 m (high degree of non-linearity) in Figure 8.8(a)-(c).

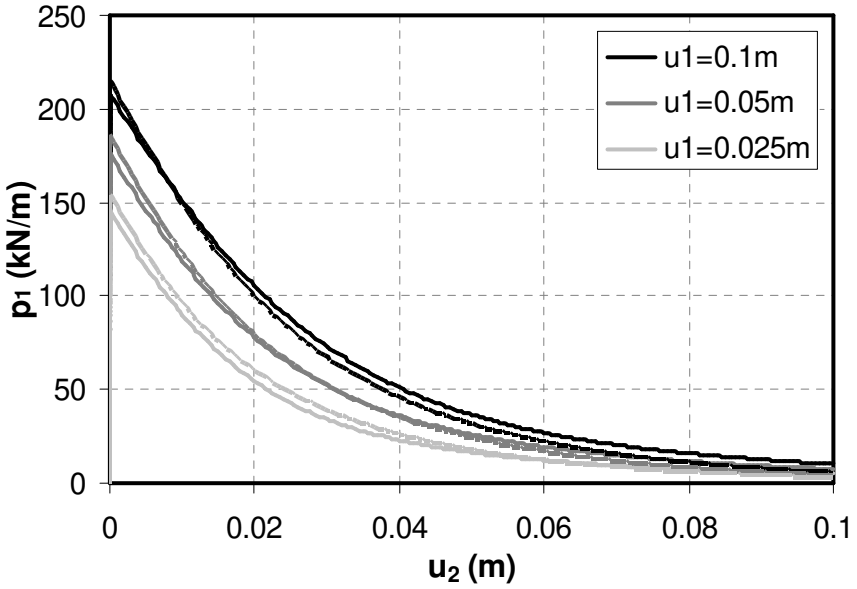

Figure 8.6 Unloading curves along x_1 direction for calibration of 'c' parameter

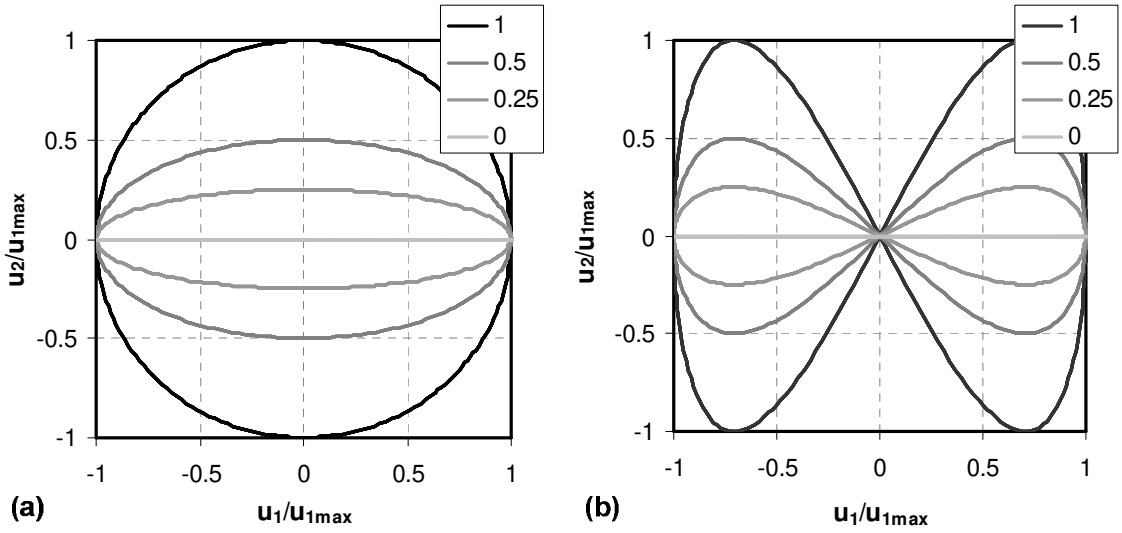

Figure 8.7 Cyclic Displacement Loading patterns (a) 0-shaped (b) 8-shaped

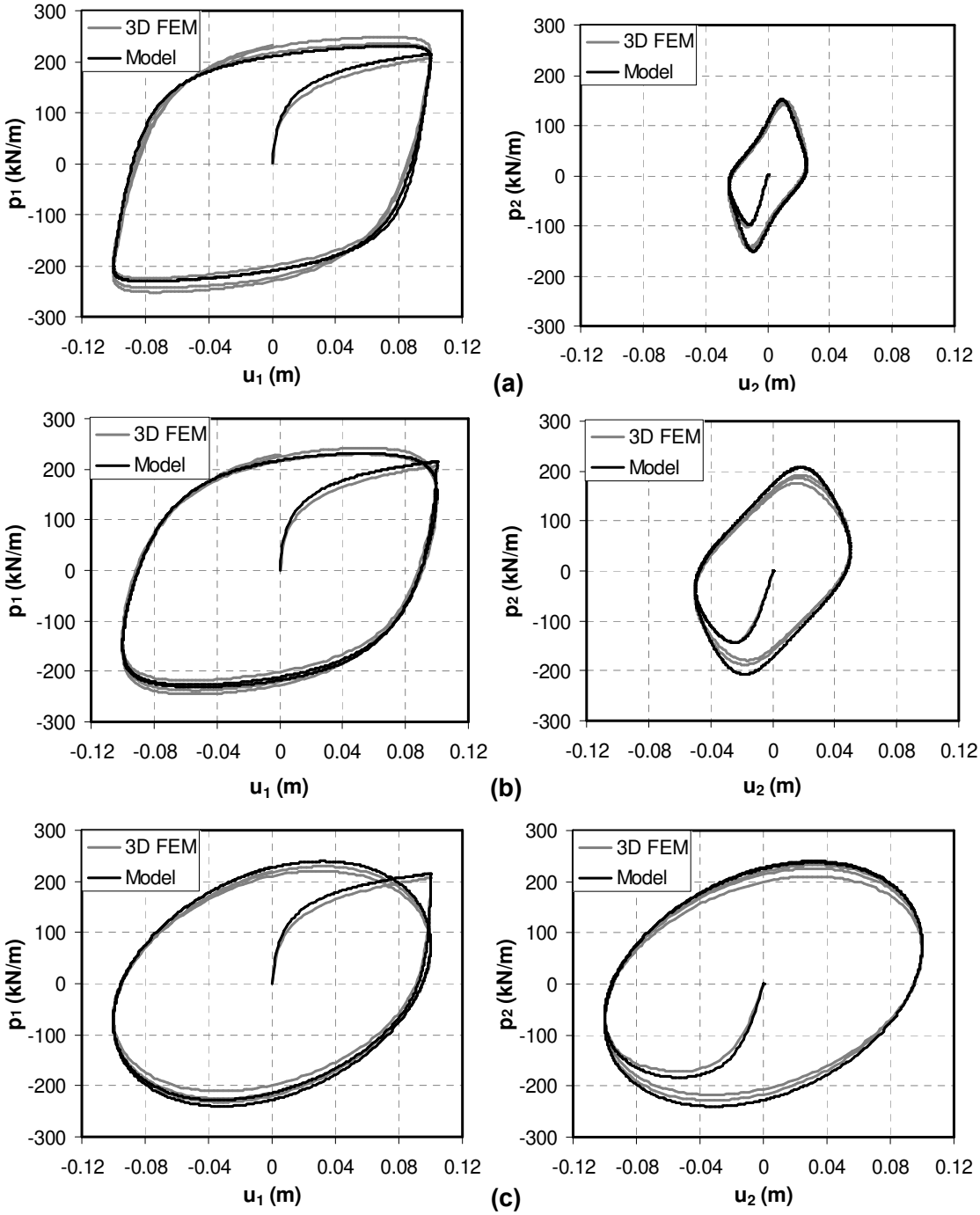

Figure 8.8 Comparison between FEM and proposed model results for pile response to 0-shaped biaxial cyclic loading with displacement amplitude u_1= 0.1 m and for displacement amplitude ratio (a) 0.25 (b) 0.5 and (c) 1.0

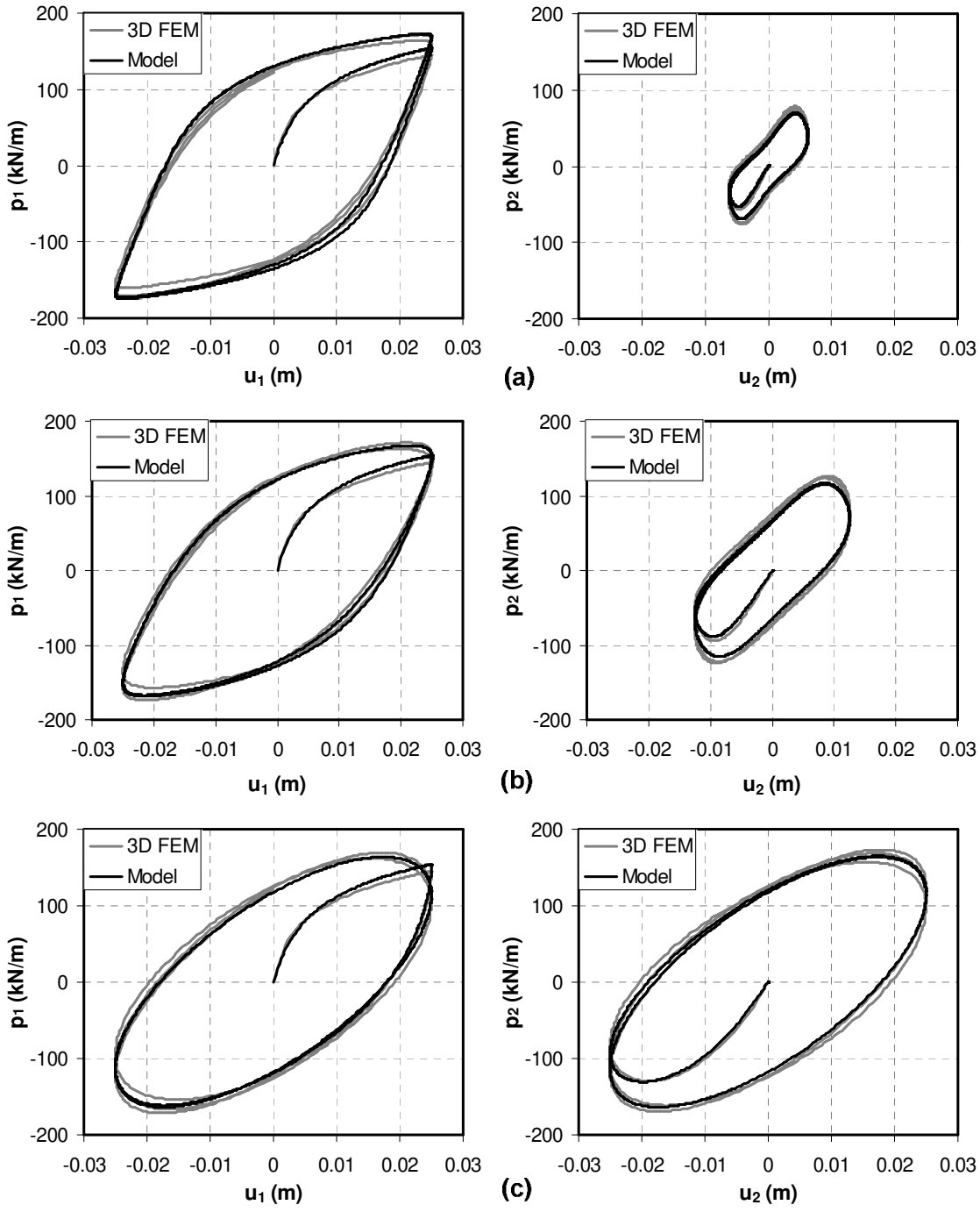

Figure 8.9 Comparison between FEM and proposed model results for pile response to 0-shaped biaxial cyclic loading with displacement amplitude u_1= 0.025 m and for displacement amplitude ratio (a) 0.25 (b) 0.5 and (c) 1.0

In both cases, the effect of severity of loading in the other direction is examined for the ratio of amplitudes of displacement u_2/u_1 varying from 0.25 to 1.0.

The results show that as displacement amplitude ratio increases, the response along x_1 shows rounding of corners near the unloading time instant. The rounding of corners implies a decrease in the energy dissipated due to hysteresis; however, the overall response along x_1 starts deviating from uncoupled response only for displacement amplitude ratio higher than 0.5. On the other hand, the response along x_2 direction is remarkably different with the differences between coupled and uncoupled response being more significant for lower values of displacement amplitude ratio. The peak resistance is reached at around 33% of peak displacement and negative stiffness values are observed thereafter. As expected, the effect of coupling in both directions is more pronounced for higher displacement amplitude, i.e., higher degree of non-linearity. The response in all cases is captured quite well by the proposed model.

8 shaped loading

In case of 8-shaped loading, the displacement along x_2 reaches maximum before it does so for x_1. Thus both during loading and unloading along x_1, a complete reload-unload cycle takes place along x_2 direction. The results for displacement amplitude u_1 = 0.025 m are shown in Figure 8.11(a)-(c) whereas for u_1 = 0.1 m are shown in Figure 8.10(a)-(c). Similar to the observations in 0-shaped loading, the effect of coupling on response in x_1 direction becomes significant only for displacement amplitude ratio higher than 0.5. The response shows rounded corners, strain hardening kind of behavior during loading in x_2 direction and negative stiffness during unloading in x_2 direction. For x_2 direction, asymmetry is observed due to unloading and reloading phases in x_1 direction with the asymmetry being more pronounced for lower values of displacement amplitude ratio. The proposed model again is able to capture the response very well.

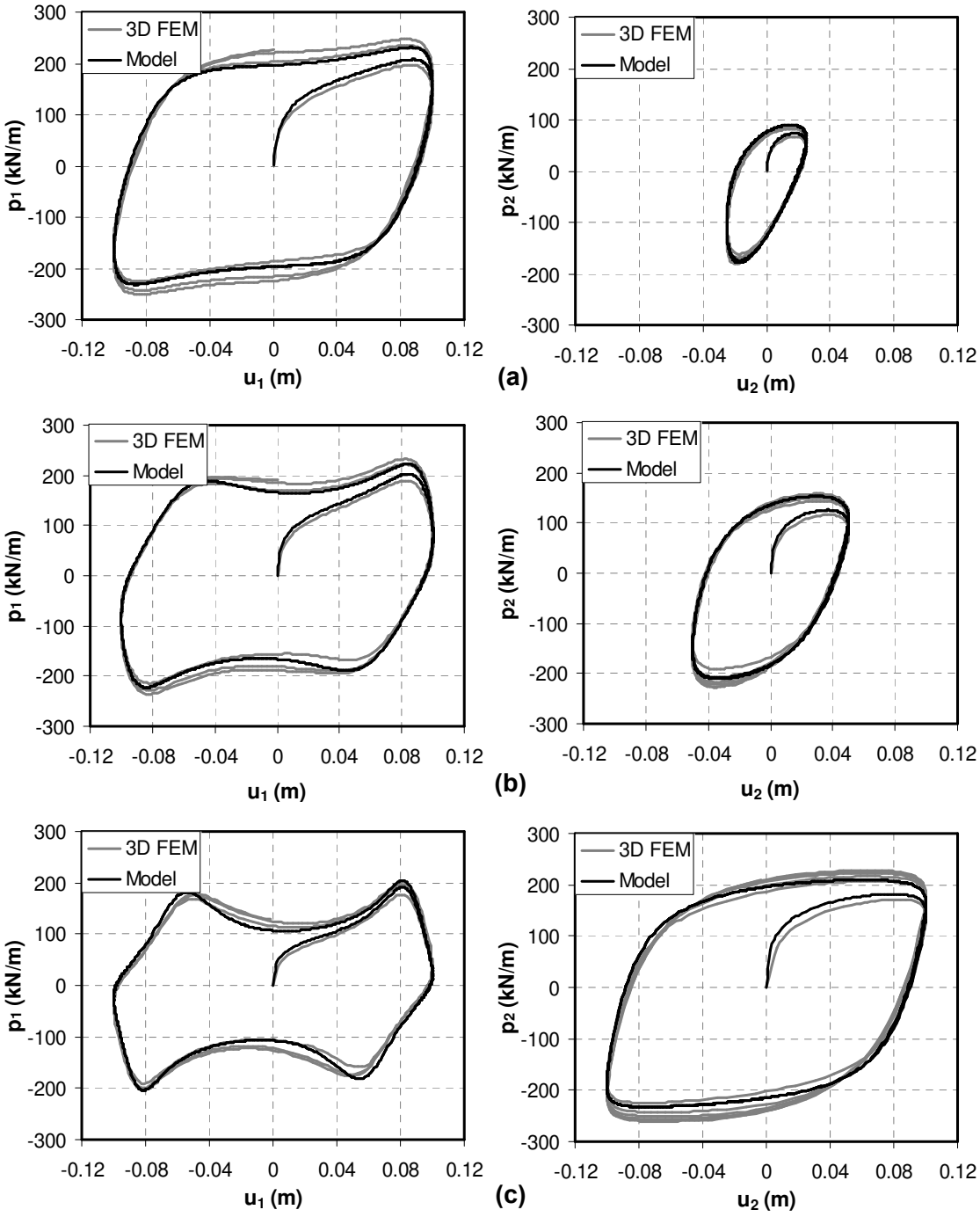

Figure 8.10 Comparison between FEM and proposed model results for pile response to 8-shaped biaxial cyclic loading with displacement amplitude u_1= 0.1 m and for displacement amplitude ratio (a) 0.25 (b) 0.5 and (c) 1.0

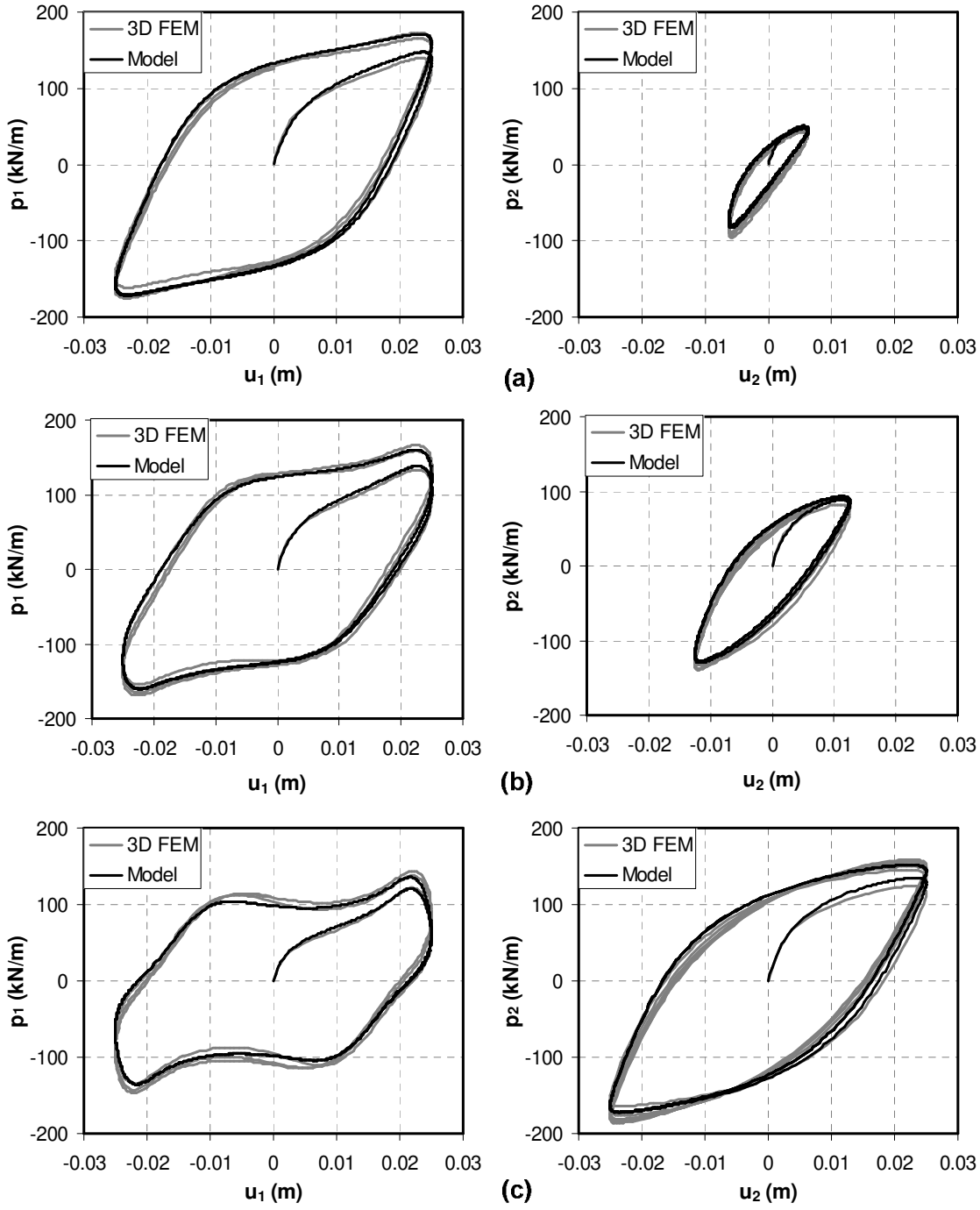

Figure 8.11 Comparison between FEM and proposed model results for pile response to 8-shaped biaxial cyclic loading with displacement amplitude u_1= 0.025 m and for displacement amplitude ratio (a) 0.25 (b) 0.5 and (c) 1.0

Comparison with transient loading

This section presents the response of pile to biaxial transient loading using earthquake time histories from 1999 Kocaeli earthquake, 1989 Loma Prieta earthquake and 1995 Kobe earthquake (PEER database). The displacement are band pass filtered 0.1-40 Hz and baseline corrected.

1999 Kocaeli earthquake

The ground motions for 1999 Kocaeli earthquake M_w 7.4 were recorded at Arcelik (ARC) station at a distance of 17 km from fault rupture. The displacement time histories in both directions are shown in Figure 8.12 with peak displacement of 13.6 cm and 35.6 cm. The horizontal displacement pattern is shown in Figure 8.13. The comparison of response time histories predicted using 3D FEM, uniaxial and biaxial model are shown in Figure 8.14(a)-(b) whereas Figure 8.15(a)-(b) shows the pile response in p-y domain for biaxial and uniaxial model, respectively.

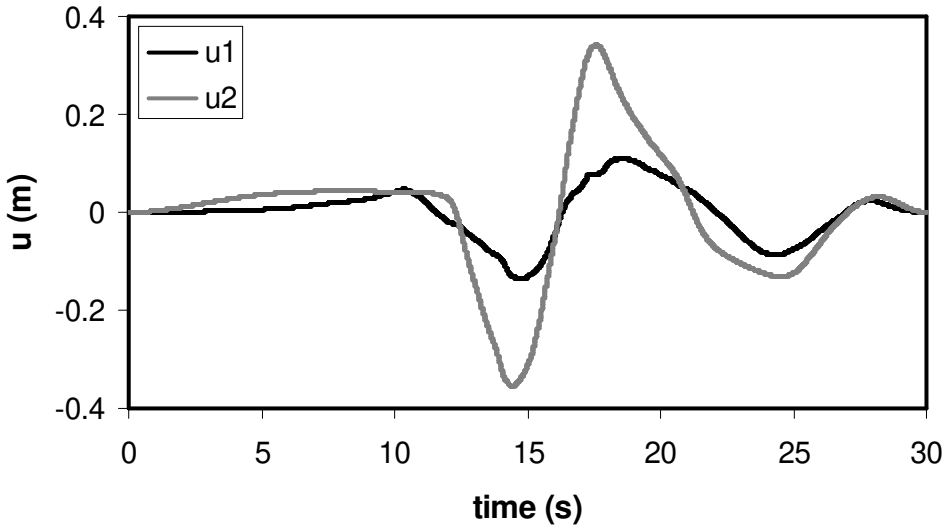

Figure 8.12 Displacement time histories in x_1 and x_2 direction for Kocaeli earthquake

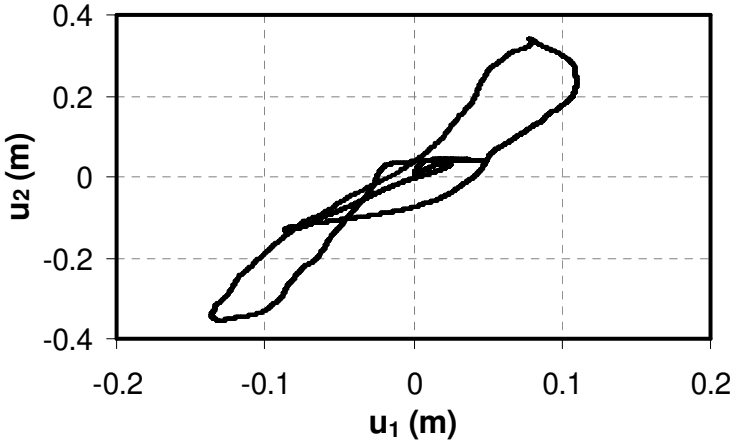

Figure 8.13 Displacement pattern in horizontal plane for Kocaeli earthquake loading

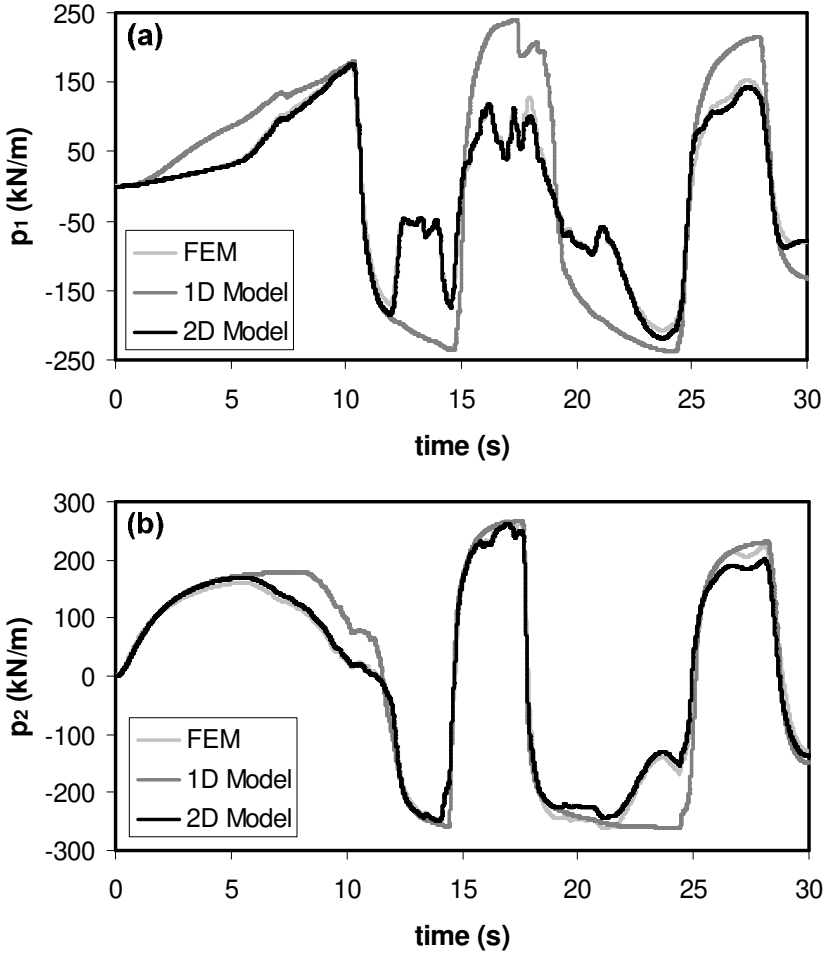

Figure 8.14 Comparison between results obtained using FEM, uniaxial and biaxial model for pile response to Kocaeli eathquake transient loading in (a) x_1 direction and (b) x_2 direction

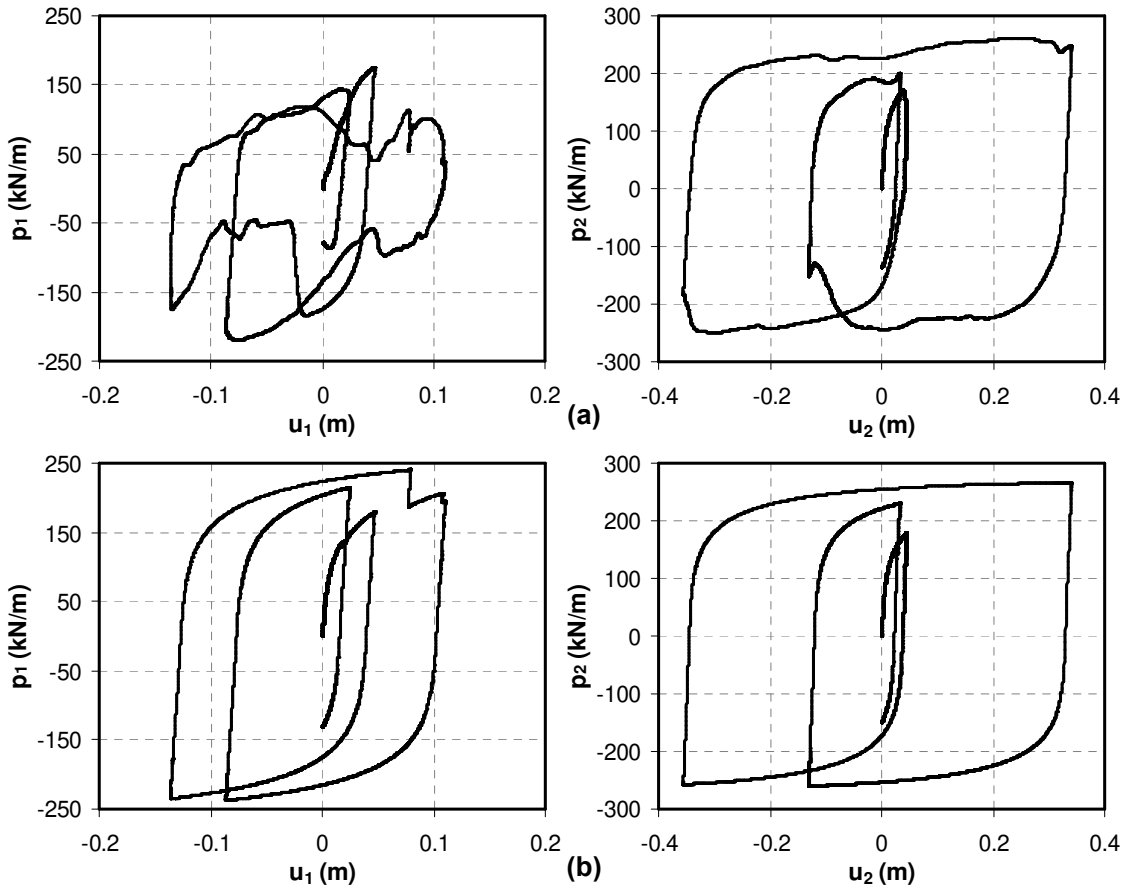

Figure 8.15 Comparison of pile response to Kocaeli earthquake loading for (a) biaxial model and (b) uniaxial model

1989 Loma Prieta earthquake

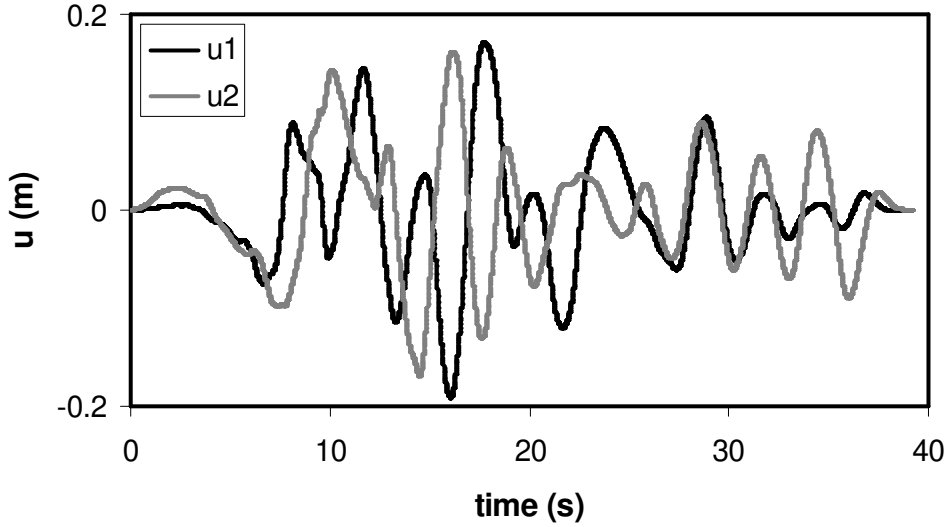

Figure 8.16 Displacement time histories in x_1 and x_2 direction for Loma Prieta earthquake

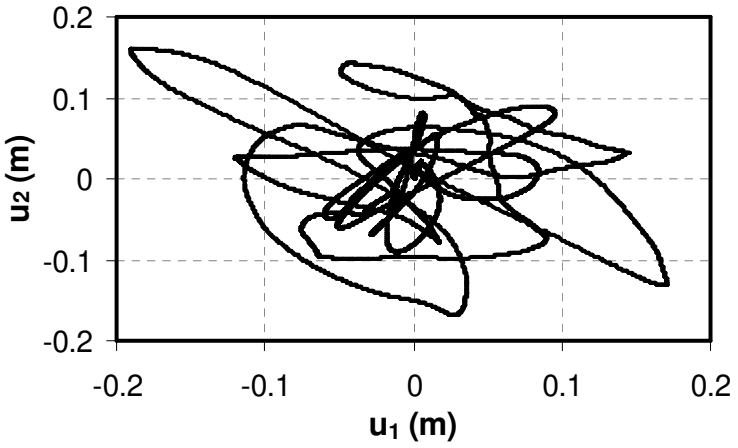

Figure 8.17 Displacement pattern in horizontal plane for Loma Prieta earthquake loading

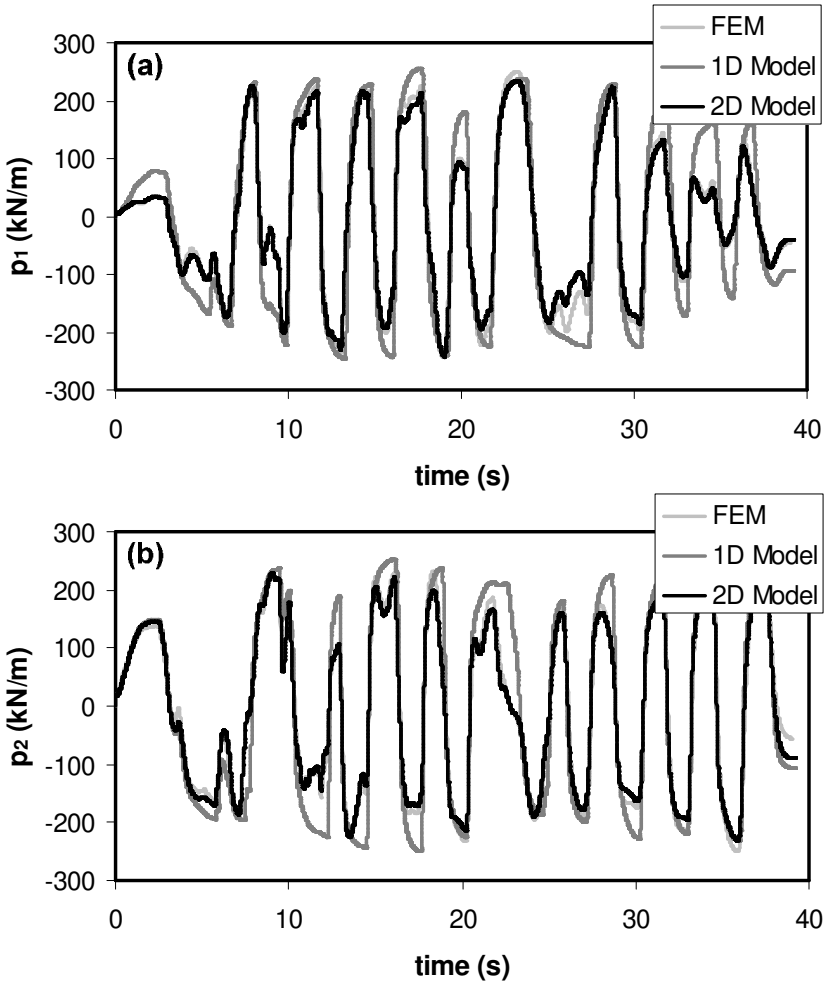

Figure 8.18 Comparison between results obtained using FEM, uniaxial and biaxial model for pile response to Loma Prieta earthquake transient loading in (a) x_1 direction and (b) x_2 direction

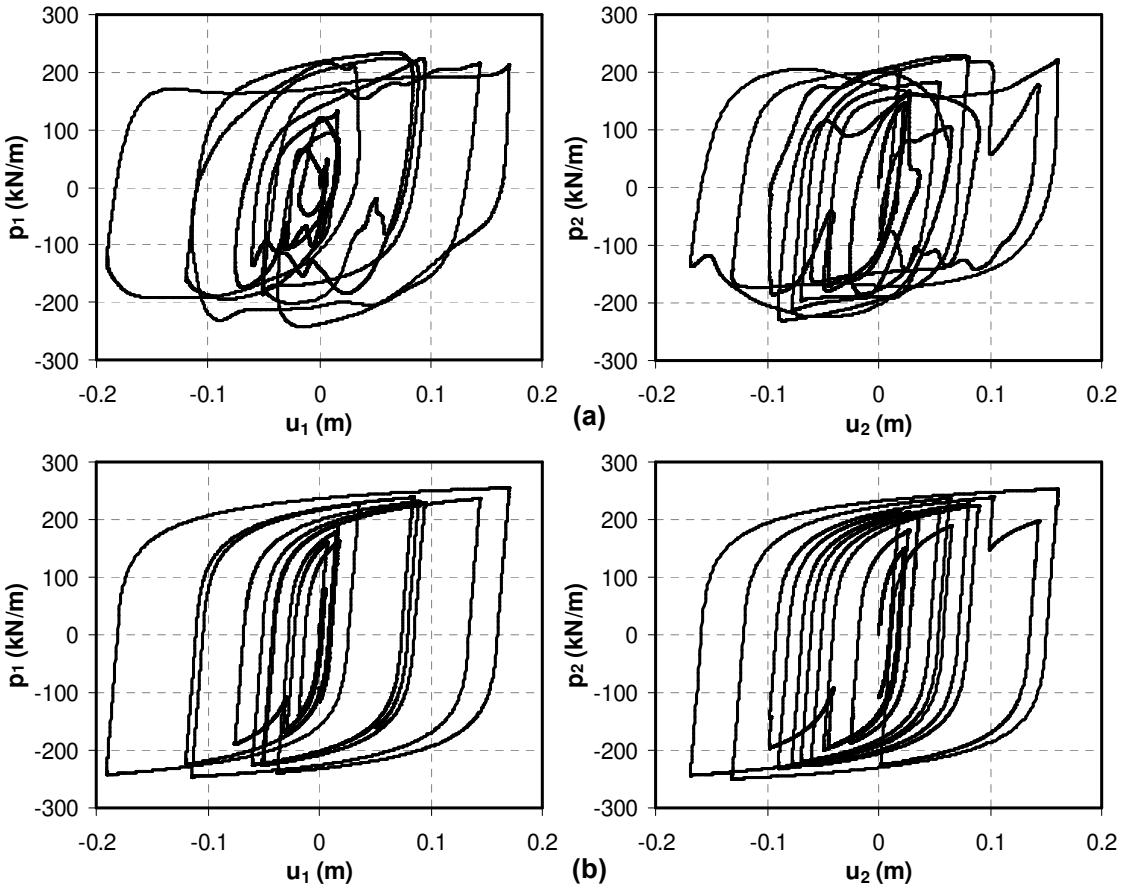

Figure 8.19 Comparison of pile response to Loma Prieta earthquake loading for (a) biaxial model and (b) uniaxial model

The ground motions for 1989 Loma Prieta earthquake M_w 6.9 were recorded at Sunnyvale-Colton Ave. (SVL) station at a distance of 28.8 km from fault rupture. The displacement time histories in both directions are shown in Figure 8.16 with peak displacement of 19.1 cm and 16.9 cm. The horizontal displacement pattern is shown in Figure 8.17. The comparison of response time histories predicted using 3D FEM, uniaxial and biaxial model are shown in Figure 8.18(a)-(b) whereas Figure 8.19(a)-(b) shows the pile response in p-y domain for biaxial and uniaxial model, respectively.

1995 Kobe earthquake

The ground motions for 1995 Kobe earthquake M_w 6.9 were recorded at OSAJ station at a distance of 8.5 km from fault rupture. The displacement time histories in both

directions are shown in Figure 8.20 with peak displacement of 9.3 cm and 8.0 cm. The horizontal displacement pattern is shown in Figure 8.21. The comparison of response time histories predicted using 3D FEM, uniaxial and biaxial model are shown in Figure 8.22(a)-(b) whereas Figure 8.23(a)-(b) shows the pile response in p-y domain for biaxial and uniaxial model, respectively.

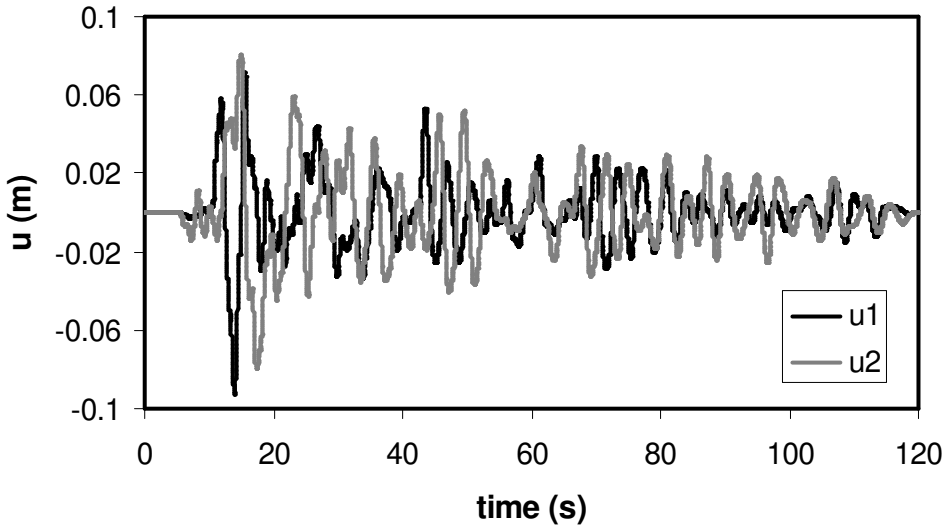

Figure 8.20 Displacement time histories in x_1 and x_2 direction for Kobe earthquake

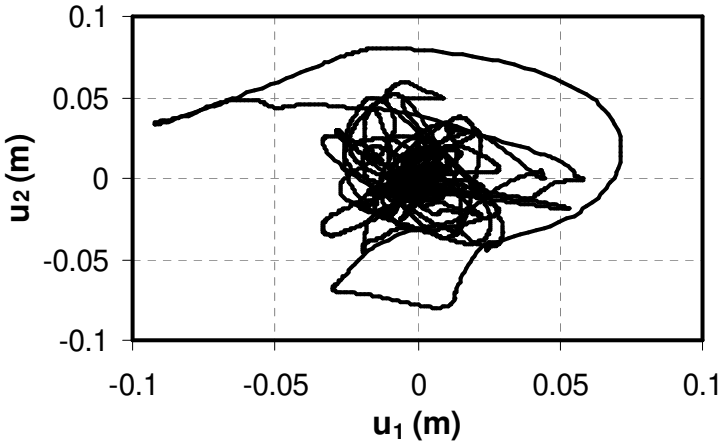

Figure 8.21 Displacement pattern in horizontal plane for Kobe earthquake loading

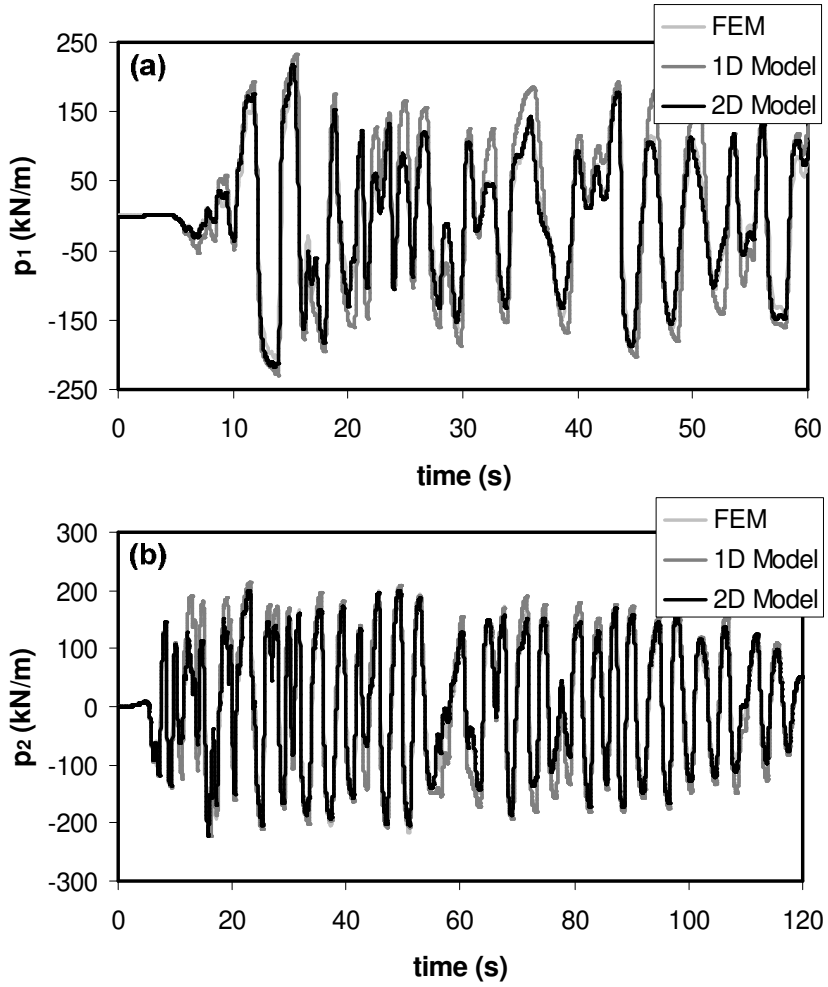

Figure 8.22 Comparison between results obtained using FEM, uniaxial and biaxial model for pile response to Kobe earthquake transient loading in (a) x_1 direction and (b) x_2 direction

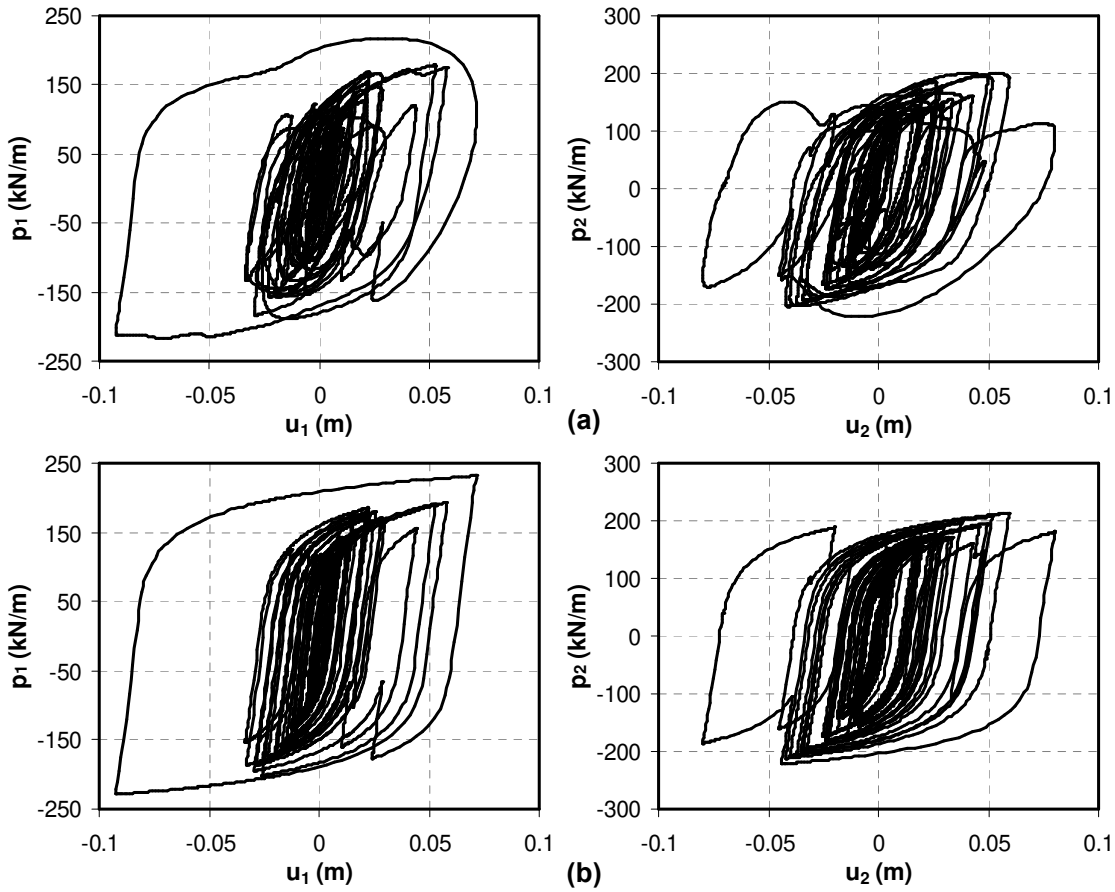

Figure 8.23 Comparison of pile response to Kobe earthquake loading for (a) biaxial model and (b) uniaxial model

Observations

In order to compare the difference between pile response predicted by uniaxial (p_{uni}) and biaxial (p_{bi}) models, the misfit between soil resistance time histories is calculated as

$$\varepsilon = \sqrt{\sum_{i=1}^{n} \left(p_{bi} - p_{uni} \right)^2 \Big/ \sum_{i=1}^{n} \left(p_{bi} \right)^2} \qquad (8.30)$$

The results for both directions and all three earthquakes are presented in Table 8.2. Comparing the pile response obtained using transient loading histories from the above mentioned three earthquakes, the following observations can be made

(a) The proposed biaxial model is able to capture the response obtained from 3D FEM to a high degree of accuracy for all three cases.

(b) Using two uncoupled uniaxial models in both directions tends to overestimate the soil strength and always predicts stiffer response compared to actual case. It also fails to capture rounding of corners near unloading, negative stiffness and apparent strain hardening behavior observed in coupled response.

(c) The difference between coupled and uncoupled response is more pronounced as the degree of soil non-linearity increases. This can be seen from lower difference for Kobe and Loma Prieta earthquakes but significant difference for Kocaeli earthquake (Table 8.2).

Table 8.2 Misfit between time histories predicted by uniaxial (1D) and biaxial (2D) models

Earthquake	u_1(cm)	u_2(cm)	ε_1	ε_2	ε_{tot}
1999 Kocaeli	13.6	35.6	0.754	0.273	0.307
1989 Loma Prieta	19.1	16.9	0.468	0.400	0.302
1995 Kobe	9.3	8.0	0.435	0.303	0.259

Conclusions

A generalized hysteresis model was presented to capture pile response to biaxial loading in horizontal direction. The model was calibrated using 3D FEM simulations and was found to simulate the response to both cyclic and transient loading with high degree of accuracy. The effect of coupling in both directions was compared as a function of soil non-linearity mobilized during the loading and it was observed that neglecting the coupling can lead to overestimation of soil resistance by upto 43% for displacements as low as 10% of pile diameter.

CHAPTER 9

CONCLUSIONS AND FUTURE WORK

Conclusions

In this thesis, we presented a detailed parametric investigation of the dynamic response of single piles in liquefiable soils using 3D FEM simulations. The numerical results compared very well with a series of important observations made in centrifuge tests, and offered additional insight in mechanisms manifesting due to soil-structure interaction in liquefiable sites such as:

(a) Residual drag resistance of 10 kPa in liquefied sand at low displacements.

(b) Excess pore pressure generation in near field caused by cyclic structural loading at low displacement values.

(c) Dilative soil response at higher displacements with loose sands (D_r = 35%) retaining only 10% of their original strength after liquefaction but medium dense sands (D_r = 55%) retaining upto 30% of original strength.

(d) The gradual change from fully drained to fully undrained behavior with decreasing permeability or increasing loading rate.

(e) The effect of soil non-linearity on radiation damping

Based on the numerical results, we then proposed a generic macroelement that can be used to simulate the observed pile response parameterized as a function of the soil properties that were identified from the parametric investigation. The mechanical model comprises a nonlinear Winkler-type model that accounts for soil resistance acting along the circumference of the pile, and a coupled viscous damper that simulates changes in radiation damping with increasing material non-linearity. A semi-empirical approach that accounts for the effects of soil-structure interaction on pore pressure generation in the vicinity of pile is used to detect the onset of liquefaction. The calibration of these

parameters is performed using 3D FEM simulations. The macroelement parameters are related to soil properties as

(a) Stiffness Modulus (K)

$$K = 1.25E_s \tag{9.1}$$

(b) Ultimate resistance (p_y)

$$p_y = \left(3.25K_p + 0.3K_p^2\right) B\sigma_v' \tag{9.2}$$

(c) Backbone curve parameter (α)

$$\alpha = \begin{cases} 2.7 & Dense \\ 2.8 & Medium \\ 2.9 & Loose \end{cases} \tag{9.3}$$

(d) Slope of phase-transformation line (m_2)

$$m_2 = 3.25\tan^2\left(45^\circ + \varphi_{ss}/2\right) \tag{9.4}$$

(e) Shear work correlation parameter

$$w_1 = \frac{n^{(1-n)}(1-2\nu)^{2n}(1-\nu)^{2(1-n)}}{\chi} \tag{9.5}$$

(f) Drainage parameter (β)

$$\beta = 550\frac{2(1+\nu)}{3(1-2\nu)}\frac{k}{B} \tag{9.6}$$

The calibration of macroelement was verified by comparison of the response with 3D FEM simulations. The validation and benchmarking was performed next by comparison with field data from blast induced liquefaction tests, and seismic soil structure interaction data from centrifuge test. The macroelement was shown to perform well in both situations, namely when:

(a) direct loading is applied to the structure and structural loading is the primary source of excess pore pressure generation (field tests) and

(b) both loading and excess pore pressure comes primarily from far-field initially followed by inertial loading from the superstructure (centrifuge tests).

The model for drained loading was then extended to capture the pile response to biaxial loading in the horizontal direction. The biaxial Bouc-Wen model was calibrated using 3D FEM simulations and was found to simulate the response to both cyclic and transient loading with high degree of accuracy. The effect of coupling in both directions was compared as a function of soil non-linearity mobilized during the loading and it is observed that neglecting the coupling can lead to overestimation of soil resistance by upto 44% for displacements as low as 10% of pile diameter. It also fails to capture rounding of corners near unloading, negative stiffness and apparent strain hardening behavior observed in coupled response. The difference between coupled and uncoupled response is more pronounced as the degree of soil non-linearity increases.

Future Work

(a) The macroelement developed in this study is meant for vertical piles. However, many old waterfront structures still use battered piles along with vertical piles. FEM simulations can be used to compare the difference in p-y response vertical and battered piles and then extend the macroelement to capture the response of battered piles as well.

(b) Since most waterfront structures have pile spacing greater than 4 pile diameters, the pile-soil-pile interaction factors can be ignored. However, the macroelement parameters such as phase transition slope and liquefaction resistance can be expressed as functions of normalized pile spacing (S/B) for $S/B < 4$.

(c) The same approach used to develop macroelement for sand can be extended to account for cyclic softening of clays. The multi-directional element can also be extended to clays.

APPENDIX A

MATLAB SCRIPTS

Script for Unidirectional Macroelement

```
clear all
clc
%****** Define Loading******
        dt = 0.05;
        t = 0:dt:62.5;
        u = 0.02*sin(2*pi*0.1*t);
        ru = 0.0*t;
        Sff = 1-ru;
        tol = 0.0005;
%****** Define model parameters******
        n = 0.5;
        B = 1.0;
        beta = 0.0;
        si = 19500;
        Y_m = 51400000;
        a = 2.9;
% m1(phi), m2(phip), w1
        prm = [16.5,9.75,1.33];
%******Backbone curve*******
        k = Y_m*1.25*(si/100000)^n;
        py = si*B*prm(1);
        uy = py/k;
%******Hysteresis loop******
        b = 0.6;
        g = 0.4;
% ******Start calculations******
        zeta(1) = 0.0;
        p(1)= 0;
        w(1) = 0;
        S(1)= 1.0;
        S0(1) = 1.0;
        for i=2:length(u)
                du = u(i)-u(i-1);
                tzeta = zeta(i-1);
                f = 1;
                while abs(f)>tol
                        f = tzeta-zeta(i-1)-(1-tanh(a*abs(tzeta))/tanh(a)*(b+g…
                        *sign(du*tzeta)))*du/uy;
```

```
                fd = 1+(sech(a*abs(tzeta)))^2/tanh(a)*…
                (b+g*sign(du*tzeta))*du/uy*a*sign(tzeta);
                tzeta = tzeta - f/fd;
        end
        zeta(i) = tzeta;
         p(i) = py*zeta(i)*S(i-1);
        dw = 0;
        if abs(zeta(i))<=0.67*prm(2)/prm(1)
                dw =  abs(p(i)*(du - (p(i)-p(i-1))/(k*(S(i-1))^n))/py/uy);
        end
        w(i) = w(i-1) + dw;
        dSb = 1.4*S0(i-1)*(-1*log(S0(i-1)-0.005))^(0.4/1.4)*dw/prm(3);
        dSd = beta*S(i-1)^n*dt/(1+beta*S(i-1)^n*dt)*(Sff(i)-S(i-1));
        S0(i) = S0(i-1) - dSb + dSd;
        if (abs(zeta(i))<0.67*prm(2)/prm(1))
                S(i) = S0(i);
        else
                c = 1/(1.1+0.4*S0(i));
                alp = 1/3*prm(2)/prm(1)*c;
                S2 = S0(i)*(1-alp);
                r3 = 0.67*prm(2)*S0(i);
                S(i) = S0(i)*((1-alp-2*alp*abs(c*zeta(i)))+((1-alp-…
                2*alp*abs(c*zeta(i)))^2-(1-c^2*zeta(i)^2)*(1-2*alp-…
                4*alp^2))^0.5)/(1-c^2*zeta(i)^2);
        end
end
```

Script for Biaxial Macroelement

```
clear all
clc
% ******Define Loading******
dt = 0.05;
t = 0:dt:30;
ux = 0.10*sin(2*pi*0.1*t);
uz = 0.1*cos(2*pi*0.1*t);
uz(1:2.5/dt)=0;
%******Combine both displacements******
u = [ux; uz];
% ******Define model parameters******
n = 0.5;
si = 19500;
Y_m = 51400000;
% m1(phi)
prm = 13.85;
```

```
        tol = 0.0005;
%******Backbone curve*******
        k = Y_m*1.25*(si/100000)^n;
        py = si*prm(1);
        uy = py/k;
        a = 2.9;
%******Hysteresis loop******
        b = 0.6;
        g = 0.4;
        c = 0.25;
%****** Start calculations******
        zeta(:,1) = [1e-6; 1e-6];
        for i=2:length(u)
                du = u(:,i)-u(:,i-1);
                dun = norm(du,2);
                tz = zeta(:,i-1);
                f = [1; 1];
                while (abs(f(1))>tol || abs(f(2))>tol)
                        zn = norm(tz,2);
                        if dun == 0
                                ts = [1 0; 0 1];
                                cg = 1;
                                sg = 0;
                        else
                                ts = [du(1) du(2); -du(2) du(1)]/dun;
                                cg = du'*tz/dun/zn;
                                sg = (du(2)*tz(1)-du(1)*tz(2))/dun/zn;
                        end
                        fz = tanh(a*zn)/tanh(a);
                        fzd = a/tanh(a)*(1-tanh(a*zn)^2);
                        kn = 1-fz*(b+g*cg);
                        ks = c*fz*sg;
                        Km = [kn ks; ks kn];
                        kn1 = -1*(fzd*tz(1)/zn*(b+g*cg)-fz*g*sg*tz(2)/zn^2);
                        kn2 = -1*(fzd*tz(2)/zn*(b+g*cg)+fz*g*sg*tz(1)/zn^2);
                        ks1 = c*(fzd*tz(1)/zn*sg+fz*cg*tz(2)/zn^2);
                        ks2 = c*(fzd*tz(2)/zn*sg-fz*cg*tz(1)/zn^2);
                        Km1 = [kn1 ks1; ks1 kn1];
                        Km2 = [kn2 ks2; ks2 kn2];
                        f = tz - zeta(:,i-1) - ts'*Km*ts*(du/uy);
                        J = eye(2) - [(ts'*Km1*ts*(du/uy)) (ts'*Km2*ts*(du/uy))];
                        tz = tz - J^-1*f;
                end
                zeta(:,i) = tz;
        end
        p= py*zeta;
```

REFERENCES

[1] Bureau of Transportation Statistics, National Trasportation Statistics 2004, in, 2004.

[2] W.D.L. Finn, N. Fujita, Piles in liquefiable soils: seismic analysis and design issues, Soil Dyn Earthq Eng, 22 (2002) 731-742.

[3] Google Earth, Port-au-Prince, Haiti, in, 2010.

[4] PHRI (Port and Harbour Research Institute), Handbook on liquefaction remediation of reclaimed land, in, 1997, pp. 312.

[5] Nuclear Regulatory Commission, Procedures and criteria for assessing seismic soil liquefaction at nuclear power plant sites, in, 2003.

[6] E.M. Rathje, D. Chang, B.R. Cox, K.H. Stokoe, Effect of prefabricated vertical drains on pore pressure generation in liquefiable sand, in: 11th International conference on soil dynamics and earthquake engineering, Berkeley, CA, 2004, pp. 529-536.

[7] W.J. Chang, E.M. Rathje, K.H. Stokoe, B.R. Cox, Direct evaluation of effectiveness of prefabricated vertical drains in liquefiable sand, Soil Dyn Earthq Eng, 24 (2004) 723-731.

[8] P.M. Gallagher, J.K. Mitchell, Influence of colloidal silica grout on liquefaction potential and cyclic undrained behavior of loose sand, Soil Dyn Earthq Eng, 22 (2002) 1017-1026.

[9] P.M. Gallagher, A. Pamuk, T. Abdoun, Stabilization of liquefiable soils using colloidal silica grout, J Mater Civil Eng, 19 (2007) 33-40.

[10] A. Pamuk, P.M. Gallagher, T.F. Zimmie, Remediation of piled foundations against lateral spreading by passive site stabilization technique, Soil Dyn Earthq Eng, 27 (2007) 864-874.

[11] J.P. Stewart, R.B. Seed, G.L. Fenves, Empirical evaluation of inertial soil structure interaction effects, in: PEER-98/07, UCB, 1998.

[12] E. Kausel, J.M. Roesset, Dynamic Stiffness of Circular Foundations, J Eng Mech Div-Asce, 101 (1975) 771-785.

[13] K. Tokimatsu, H. Mizuno, M. Kakurai, Building damage associated with geotechnical problems, Soils Found, 1 (1996) 219-234.

[14] D.J. Dowrick, Earthquake Resistant Design, Wiley, 1977.

[15] H. Matlock, Correlations for design of laterally loaded piles in soft clay, in: 2nd Annual Offshore Technology Conference, 1970, pp. 577-594.

[16] L.C. Reese, W.R. Cox, F.D. Koop, Analysis of laterally loaded piles in sand, in: Offshore Technology Conference, 1974, pp. 473-484.

[17] American Petroleum Institute, Recommended Practice for Planning, Designing and Constructing Fixed Offshore Platforms, in: API Recommended Practice 2A, Washington, D.C., 1993.

[18] S.J. Brandenberg, R.W. Boulanger, B.L. Kutter, D. Chang, Static pushover analyses of pile groups in liquefied and laterally spreading ground in centrifuge tests, J Geotech Geoenviron, 133 (2007) 1055-1066.

[19] M. Novak, Dynamic stiffness and damping of piles, Can Geotech J, 11 (1974) 574-598.

[20] R. Dobry, E. Vicente, M.J. Orourke, J.M. Roesset, Horizontal Stiffness and Damping of Single Piles, Journal of the Geotechnical Engineering Division-Asce, 108 (1982) 439-459.

[21] A.M. Kaynia, E. Kausel, Dynamic behavior of pile groups, Second International conference on numerical methods in offshore piling, (1982) 509-532.

[22] M. Kavvadas, G. Gazetas, Kinematic Seismic Response and Bending of Free-Head Piles in Layered Soil, Geotechnique, 43 (1993) 207-222.

[23] J. Penizen, Soil pile foundation interaction in earthquake engineering, Prentice Hall, NJ, 1970.

[24] T. Kagawa, Soil-pile-structure interaction of offshore structures during an earthquake, in: Annual Offshore Technology Conference, Houston, 1980, pp. 235-245.

[25] T. Kagawa, L.M. Kraft, Lateral pile response during earthquakes, J Geotech Eng-Asce, 107 (1981) 1713-1731.

[26] G.M. Norris, Seismic bridge pile foundation behavior, in: International Conference on Design and Construction of Deep Foundations, 1994, pp. 27-136.

[27] T. Nogami, K. Konagai, Time Domain Flexural Response of Dynamically Loaded Single Piles, J Eng Mech-Asce, 114 (1988) 1512-1525.

[28] A. Tabesh, H.G. Poulos, Pseudostatic approach for seismic analysis of single piles, J Geotech Geoenviron, 127 (2001) 757-765.

[29] M.H. ElNaggar, M. Novak, Nonlinear analysis for dynamic lateral pile response, Soil Dyn Earthq Eng, 15 (1996) 233-244.

[30] T. Kagawa, Lateral pile response in liquefying sand, in: 10th World Conference on Earthquake Engineering, Madrid, Spain, 1992.

[31] S. Fuji, M. Cubrinovski, K. Tokimatsu, T. Hayashi, Analyses of damaged and undamaged pile foundations in liquefied soils during the 1995 Kobe Earthquake, in: Geotechnical Earthquake Engineering and Soil Dynamics III, Seattle, WA, 1998, pp. 1187-1198.

[32] D.S. Liyanapathirana, H.G. Poulos, Seismic lateral response of piles in liquefying soil, J Geotech Geoenviron, 131 (2005) 1466-1479.

[33] R.I. Borja, W.H. Wu, A.P. Amies, H.A. Smith, Nonlinear Lateral, Rocking, and Torsional Vibration of Rigid Foundations, J Geotech Eng-Asce, 120 (1994) 491-513.

[34] N.E. Funston, W.J. Hall, Footing vibration with nonlinear subgrade support, Journal of Geotechnical Engineering Division, ASCE, 93 (1967) 191-211.

[35] K.H. Stokoe, F.E. Richard, Dynamic response of embedded machine foundation, Journal of Geotechnical Engineering Division, ASCE, 100 (1974) 427-447.

[36] G. Gazetas, K.H. Stokoe, Free-Vibration of Embedded Foundations - Theory Versus Experiment, J Geotech Eng-Asce, 117 (1991) 1382-1401.

[37] Y.S. Kim, K. Miura, S. Miura, M. Nishimura, Vibration characteristics of rigid body placed on sand ground, Soil Dyn Earthq Eng, 21 (2001) 19-37.

[38] W.D.L. Finn, M. Yogendrakumar, TARA-3FL: a program for analysis of flow deformations in soil structures with liquefied zones, in, University of British Columbia, 1989.

[39] J.P. Wolf, Soil-structure interaction with separation of base mat from soil (lifting-off), Nuclear Engineering and Design, 38 (1976) 357-384.

[40] J.P. Wolf, P.E. Skriherud, Seismic excitation with large overturning moments: tensile capacity, projecting base mat or lifting-off, Nuclear Engineering and Design, 50 (1978) 305-321.

[41] T. Kobori, Nonlinear uplift response of soil structure interaction system considering ground compliance, in: 7th European Conference on Earthquake Engineering, Athens, 1982.

[42] R. Nova, L. Montrasio, Settlements of Shallow Foundations on Sand, Geotechnique, 41 (1991) 243-256.

[43] R. Paolucci, Simplified evaluation of earthquake-induced permanent displacements of shallow foundations, J Earthquake Eng, 1 (1997) 563-579.

[44] C. Cremer, A. Pecker, L. Davenne, Cyclic macro-element for soil-structure interaction: material and geometrical non-linearities, Int J Numer Anal Met, 25 (2001) 1257-1284.

[45] E. Taciroglu, C. Rha, J.W. Wallace, A robust macroelement model for soil-pile interaction under cyclic loads, J Geotech Geoenviron, 132 (2006) 1304-1314.

[46] C. Rha, E. Taciroglu, Coupled macroelement model of soil-structure interaction in deep foundations, J Eng Mech-Asce, 133 (2007) 1326-1340.

[47] R.W. Boulanger, C.J. Curras, B.L. Kutter, D.W. Wilson, A. Abghari, Seismic soil-pile-structure interaction experiments and analyses, J Geotech Geoenviron, 125 (1999) 750-759.

[48] C.J. Curras, R.W. Boulanger, B.L. Kutter, D.W. Wilson, Dynamic experiments and analyses of a pile-group-supported structure, J Geotech Geoenviron, 127 (2001) 585-596.

[49] N. Gerolymos, G. Gazetas, Development of Winkler model for static and dynamic response of caisson foundations with soil and interface nonlinearities, Soil Dyn Earthq Eng, 26 (2006) 363-376.

[50] N. Gerolymos, G. Gazetas, Static and dynamic response of massive caisson foundations with soil and interface nonlinearities - validation and results, Soil Dyn Earthq Eng, 26 (2006) 377-394.

[51] Japan Road Association, Specifications for highway bridges, in: Part V, Seismic Design, Japan, 1996.

[52] T. Abdoun, R. Dobry, T.D. O'Rourke, S.H. Goh, Pile response to lateral spreads: Centrifuge modeling, J Geotech Geoenviron, 129 (2003) 869-878.

[53] Architectural Institute of Japan, Recommendations for design of building foundations, in, Tokyo, 2001.

[54] L. Liu, R. Dobry, Effect of liquefaction on lateral response of piles by centrifuge model tests, National Center for Earthquake Engineering Research (NCEER) Bulletin, 9 (1995) 7-11.

[55] D.W. Wilson, R.W. Boulanger, B.L. Kutter, Observed seismic lateral resistance of liquefying sand, J Geotech Geoenviron, 126 (2000) 898-906.

[56] S.J. Brandenberg, R.W. Boulanger, B.L. Kutter, D.D. Chang, Behavior of pile foundations in laterally spreading ground during centrifuge tests, J Geotech Geoenviron, 131 (2005) 1378-1391.

[57] R. Dobry, V. Taboada, L. Liu, Centrifuge modeling of liquefaction effects during earthquakes, in: 1st International Conference on Earthquake Geotechnical Engineering, Tokyo, 1995, pp. 1291-1324.

[58] D.W. Wilson, Soil pile superstructure interaction in liquefying sand and soft clay, in, University of California Davis, 1998.

[59] S.A. Ashford, T.J. Weaver, K.M. Rollins, Pore pressure response of liquefied sand in full-scale lateral pile load tests, Transport Res Rec, (2002) 21-29.

[60] S.A. Ashford, K.M. Rollins, J.D. Lane, Blast-induced liquefaction for full-scale foundation testing, J Geotech Geoenviron, 130 (2004) 798-806.

[61] K.M. Rollins, T.M. Gerber, J.D. Lane, S.A. Ashford, Lateral resistance of a full-scale pile group in liquefied sand, J Geotech Geoenviron, 131 (2005) 115-125.

[62] K.M. Rollins, J.D. Lane, E. Dibb, S.A. Ashford, A.G. Mullins, Pore pressure measurement in blast-induced liquefaction experiments, Transport Res Rec, (2005) 210-220.

[63] T.J. Weaver, S.A. Ashford, K.M. Rollins, Response of 0.6 m cast-in-steel-shell pile in liquefied soil under lateral loading, J Geotech Geoenviron, 131 (2005) 94-102.

[64] K. Tokimatsu, H. Suzuki, Y. Suzuki, Back-calculated p-y relation of liquefied soils from large shaking table tests, in: S. Prakash (Ed.) Fourth International Conference on Recent Advances in Geotechnical Earthquake Engineering and Soil Dynamics, 2001, pp. 6-24.

[65] K. Tokimatsu, H. Suzuki, Pore water pressure response around pile and its effects on P-Y behavior during soil liquefaction, Soils Found, 44 (2004) 101-110.

[66] L. Gonzalez, T. Abdoun, R. Dobry, Effect of Soil Permeability on Centrifuge Modeling of Pile Response to Lateral Spreading, J Geotech Geoenviron, 135 (2009) 62-73.

[67] B.L. Kutter, T. Voss, Analysis of data on plough resistance in dense, saturated, cohesionless soil. Contract report CR95.004, in, Naval facilities engineering service center, California, 1995.

[68] A.C. Palmer, Speed effects in cutting and ploughing, Geotechnique, 49 (1999) 285-294.

[69] M. Yoshimine, Liquefied soil-pile interaction and its rate effects, in: First Japan-US workshop on Testing,Modeling and Simulation in Geomechanics, Boston, 2003.

[70] J.H. Prevost, DYNAFLOW: A nonlinear transient finite element analysis program, in, Dept. of Civil Engineering and Operations Research, Princeton University, Princeton, NJ, 1995.

[71] J.H. Prevost, A Simple Plasticity Theory for Cohesionless Frictional Soils, International Journal of Soil Dynamics and Earthquake Engineering, 4 (1985) 9-17.

[72] J.H. Prevost, Wave Propagation in Fluid-Saturated Porous Media: An Efficient Finite Element Procedure, International Journal of Soil Dynamics and Earthquake Engineering, 4 (1985) 183-202.

[73] W.D. Iwan, On a class of mdel for the yielding behavior of continuous and composite systems, Journal of Applied Mechanics, ASME, 34 (1967) 612-617.

[74] Z. Mroz, On the description of anisotropic work hardening, Journal of Mechanics of Physical solids, 15 (1967) 163-175.

[75] J. Prevost, Mathematical modeling of monotonic and cyclic undrained clay behavior, International Journal for Numerical Methods in Geomechanics, 1 (1977) 195-216.

[76] J. Prevost, C.M. Keane, Stress strain curve generation from simple material parameters, Journal of geotechnical Engineering, 116 (1989) 1255-1263.

[77] D.V. Griffiths, J.H. Prevost, Stress-Strain Curve Generation from Simple Triaxial Parameters, Int J Numer Anal Met, 14 (1990) 587-594.

[78] R. Popescu, J.H. Prevost, Comparison between Velacs Numerical Class-a Predictions and Centrifuge Experimental Soil Test-Results, Soil Dyn Earthq Eng, 14 (1995) 79-92.

[79] R. Popescu, J. Prevost, Centrifuge validation of a numerical model for dynamic soil liquefaction, Soil Dyn Earthq Eng, 12 (1993) 73-90.

[80] K. Been, M.G. Jefferies, A State Parameter for Sands, Geotechnique, 35 (1985) 99-112.

[81] R. Dobry, T. Abdoun, T.D. O'Rourke, S.H. Goh, Single piles in lateral spreads: Field bending moment evaluation, J Geotech Geoenviron, 129 (2003) 879-889.

[82] R. Popescu, Stochastic variability of soil properties: data analysis, digital simulation, effects on system behavior, in: Civil engineering and operations research, Princeton University, 1995.

[83] R. Bouc, Mathematical Model for Hysteresis, Acustica, 24 (1971) 16-&.

[84] Y.K. Wen, Method for Random Vibration of Hysteretic Systems, J Eng Mech Div-Asce, 102 (1976) 249-263.

[85] D. Badoni, N. Makris, Nonlinear response of single piles under lateral inertial and seismic loads, Soil Dyn Earthq Eng, 15 (1996) 29-43.

[86] S. Wang, B.L. Kutter, J.M. Chacko, D.W. Wilson, R.W. Boulanger, A. Abghari, Non-linear seismic soil-pile-structure interaction, Earthquake Spectra, 14 (1998) 377-396.

[87] N. Makris, G. Gazetas, Dynamic Pile Soil Pile Interaction .2. Lateral and Seismic Response, Earthquake Eng Struc, 21 (1992) 145-162.

[88] S. Iai, Y. Matsunaga, T. Kameoka, Strain space plasticity model for cyclic mobility, Soils Found, 32 (1992) 1-15.

[89] I. Towhata, K. Ishihara, Modeling soil behavior under principal axes rotation, in: Fifth International Conference on Numerical Methods in Geomechanics, 1985, pp. 523-530.

[90] J.M. Roesset, Stiffness and damping coefficients of foundations, in: ASCE Geotechnical Engineering Division National Convention, 1980, pp. 1-30.

[91] B.B. Broms, Lateral Resistance of piles in cohensionless soils, Journal of Soil Mechanics and Foundation Division, ASCE, 90 (1964) 123-156.

[92] W. Fleming, G.K. Weltman, A.J. Randolph, W.K. Elson, Piling engineering, Surrey University Press, London, 1992.

[93] J.M. Murchison, M.W. O'Neill, Evaluation of P-y relationships in cohesionless soils, in: J.R. Meyer (Ed.) Analysis and design of pile foundations, Geotechnical Engineering Division, ASCE, San Francisco, 1984, pp. 174-191.

[94] L. Yan, P.M. Byrne, Lateral Pile Response to Monotonic Pile Head Loading, Can Geotech J, 29 (1992) 955-970.

[95] J.R. Faris, P. de Alba, National geotechnical experimentation site at Treasure Island, California, in: National geotechnical experimentation sites, Geotechnical Special Publication No. 93, ASCE, NY, 2000.

[96] F.H. Kulhawy, P.W. Mayne, Manual on estimating soil properties for foundation design, in, Electric Power Research Institute, Palo Alto, California, 1990.

[97] R.B. Peck, W.E. Hanson, T.H. Thornburn, Foundation Engineering, Wiley, NY, 1974.

[98] F. McKenna, OPENSEES: Open system for earhtquake engineering simulation, in, PEER, Berkeley, 1999.

[99] K. Arulanandan, R.F. Scott, Verification of numerical procedures for the analysis of soil liquefaction problems, in: International Conference on the Verification of Numerical Procedures for the Analysis of Soil Liquefaction Problems, A. A. Balkema, 1994.

[100] G. Mylonakis, G. Gazetas, Seismic soil-structure interaction: Beneficial or detrimental?, J Earthquake Eng, 4 (2000) 277-301.

[101] S. Karthigeyan, V.V.G.S.T. Ramakrishna, K. RajagopaL, Numerical investigation of the effect of vertical load on the lateral response of piles, J Geotech Geoenviron, 133 (2007) 512-521.

[102] Varun, D. Assimaki, A Nonlinear dynamic macroelement for soil-structure interaction analyses of pile-supported waterfront structures, Int J Numer Anal Met, Submitted (2010).

[103] Y.J. Park, Y.K. Wen, A.H. Ang, Random vibration of hysteretic systems under bi-directional ground motions, Earthquake Eng Struc, 14 (1986) 543-557.

[104] C.H. Wang, Y.K. Wen, Evaluation of pre-Northridge low-rise steel buildings. I: Modeling, J Struct Eng-Asce, 126 (2000) 1160-1168.

VITA

VARUN

VARUN was born in Haryana, India. He attended public schools in Karnal, Haryana and received his B.Tech. in Civil Engineering from Indian Institute of Technology Delhi (IITD), India in 2005 before coming to Georgia Institute of Technology for graduate studies. He obtained an MS in Civil Engineering (Geosystems) from Georgia Tech in 2006 and continued for his doctoral degree. When he is not working on his research, Varun enjoys tweaking his gadgets, coding for fun and gazing at stars with his amateur telescope.